The Design and Testing of Integrated Circuits for Submillimeter-wave Spectroscopy

by

Noah Zamdmer

Submitted to the Department of Electrical Engineering and Computer Science

in partial fulfillment of the requirements for the degree of

Doctor of Philosophy

at the

MASSACHUSETTS INSTITUTE OF TECHNOLOGY

June 1999

Author .....
Department of Electrical Engineering and Computer Science
June 21, 1999

Certified by .....
Qing Hu
Associate Professor of Electrical Engineering and Computer Science
Thesis Supervisor

Accepted by .....
Arthur C. Smith
Chairman, Departmental Committee on Graduate Students

The Design and Testing of Integrated Circuits for Submillimeter-wave Spectroscopy

by

Noah Zamdmer

Submitted to the Department of Electrical Engineering and Computer Science
on June 21, 1999, in partial fulfillment of the
requirements for the degree of
Doctor of Philosophy

Abstract

Optoelectronic techniques have extended the bandwidth of electronic spectroscopic systems to the submillimeter wavelengths. In a significant class of these systems the submillimeter-wave source, detector and device of interest are monolithically integrated. Such systems are attractive because of their reliability and small size and cost, because an integrated circuit is the highest-bandwidth environment for testing microelectronic devices, and because of their potential application to on-chip chemical and biological sensing. This thesis focuses on three separate topics in the field of submillimeter-wave spectroscopy with integrated circuits.

The first topic is the decrease in bandwidth of photoconductive submillimeter-wave emitters with increasing voltage bias, which limits the output power of these devices at frequencies near 1 THz. We performed measurements of a photoconductor made of low-temperature grown GaAs embedded in a coplanar waveguide with both static and dynamic illumination. We investigated the bandwidth decrease and an increase in dc photocurrent that occurs at the same bias voltages. We attribute both phenomena to a reduction of the electron capture cross section of donor states due to electron heating and Coulomb-barrier lowering.

The second topic is a novel circuit for ultrafast measurements with coplanar waveguide transmission lines. The circuit contains photoconductive switches that allow tunable generation and reception of a coplanar waveguide's two propagating modes. The circuit has fewer discontinuities than other circuits with similar capabilities and does not require airbridges. We show how the photoconductive switch can be biased to compensate for pump laser beam misalignment.

The third topic is the first demonstration of an integrated circuit's use for submillimeter-wave frequency-domain spectroscopy. Such an application is attractive because of its inherently good frequency resolution, which is necessary for chemical and biological detection. The amplitude and phase of the measured spectrum of a circuit without a device under test agree with a model that takes into account circuit resonance, photoconductive-switch dynamics, and resistive loss. We discuss why photoconductive frequency-domain spectroscopy has an inherently lower output signal

than similar time-domain spectroscopy, and how this drawback can be compensated for.

Thesis Supervisor: Qing Hu
Title: Associate Professor of Electrical Engineering and Computer Science

Acknowledgments

I very much enjoyed my five years in this experimentalist's heaven. I enjoyed working with my hands in the clean room and in the machine shop, and in experimenting with lasers, mirrors, chips and fibers. I enjoyed the challenge of trying to understand what I was making, to comprehend the motions of electrons and photons micron by micron, picosecond by picosecond. I would like to thank my fellow students with whom I have shared the same pleasures, passions and ambitions day by day, and who taught me to play this wonderful game: Rolf Wyss, Gert de Lange, Farhan Rana, Bin Xu, Ilya Lyubomirsky, Erik Duerr, Arif Rahman, Ben Williams, Brian Reily and Konstantinos Konistis

I would like to give special thanks to those whose great insight, skill and experience were instrumental in my progress: my advisor, Professor Qing Hu, and Simon Verghese and Alex McIntosh of Lincoln Lab. There were many obstacles and forks in the path of this thesis, and their advice and encouragement brought me through to the end.

I would also like to thank others for their support: Professor Mike Melloch of Perdue and Dr. Arno Förster of Forschungszentrum Jülich for low-temperature-grown GaAs wafers, Dr. Mike Rooks of the National Nanofabrication Facility at Cornell for help with e-beam lithography, Karen Molvar and Bob Murphy of Lincoln Laboratory for processing help, Professor Clifton Fonstad for serving as a reader of this thesis, Kevin Thomas of Silicon Graphics for free use of the LC electromagnetic simulator, the NSF for funding through its MRSEC program, and the National Aeronautics and Space Administration, Office of Space Access and Technology for funding, through the Center for Space Microelectronics Technology, Jet Propulsion Laboratory, California Institute of Technology.

Finally, I thank my dear friend and intellectual cohort, Jan-Hein Cremers, for being the most brilliant spectator.

To my grandparents, this fruit of their endurance

Contents

List of Figures

List of Tables

Chapter 1

Introduction

Spectroscopy in the submillimeter-wave frequency range has always been difficult, because of the lack of a cheap, compact, high-power and broadly tunable single-frequency emitter in that range. In the last 15 years, spectrometers with photoconductive emitters and detectors have been developed, and are especially popular for coherent, time-domain spectroscopy [1]. Today's ultrafast photoconductors have subpicosecond response time, and thus can sustain transient currents that radiate submillimeter waves, and can sample incident electromagnetic waves with subpicosecond temporal resolution.

The aim of this thesis is to improve the technology of submillimeter-wave photoconductive spectroscopy. Our focus is on-chip rather than free-space spectroscopy, because this is the less developed field, yet has some very attractive applications. These applications are: measurement of the S-parameters of today's fastest electronic devices, which have cutoff frequencies above 500 GHz [2]; on-chip biological and chemical spectroscopy with microfluidic circuits, since the absorption spectra of molecules have features in the submillimeter-wave band [3]; development of terahertz-bandwidth optoelectronic circuits for communications, since simple spectroscopic integrated circuits with embedded photoconductors are the forerunners of communications circuits; and experimental observation of intersubband transitions in quantum-effect electronic devices, since these transitions fall in the submillimeter-wave band [4]. On-chip spectroscopy is also attractive because on-chip systems tend to be cheaper, more compact

and more reliable than their free-space-coupled counterparts.

This thesis contains three major chapters in which we discuss three separate topics relating to on-chip submillimeter-wave spectroscopy. We begin with a device-level topic, and broaden our scope with each successive chapter towards the system-level. In Chapter 2 we discuss ultrafast photoconductive emitters made of low-temperature grown (LTG) GaAs. The goal of the chapter is to specify and model the physical mechanism that causes the photoconductor's response time to increase with increasing voltage bias. Such modeling is important because the increase in response time can diminish a photoconductive emitter's power output at submillimeter-wave frequencies, and the entire field of submillimeter-wave spectroscopy is in need of bright sources.

In Chapter 3 we discuss a coplanar waveguide (CPW) circuit with two embedded LTG GaAs photoconductors for on-chip submillimeter-wave spectroscopy. Coplanar waveguides are often used in ultrafast electronic experiments because they have the best transmission properties of any coplanar transmission line. However, CPWs have two propagating modes which are subject to mixing, and therefore CPW circuits require selective mode excitation and detection. We introduce a novel embedded photoconductor with two active regions that allows mode control.

In Chapter 4 we show how the circuit introduced in Chapter 3 can be used for coherent, frequency-domain spectroscopy. While LTG GaAs photoconductors have been used for time-domain spectroscopy for over ten years, by using one photoconductor as an emitter of subpicosecond electromagnetic pulses and another as a pulse sampler, a frequency-domain application was only recently proposed [5]. On-chip frequency-domain spectroscopy is attractive because it has a frequency resolution of less than 1 MHz, which is about 1000 times less than the typical frequency resolution of photoconductive time-domain spectroscopy systems. Such frequency resolution is necessary for chemical and biological detection.

Chapter 2

Model of a Low-temperature-grown GaAs Photoconductor at High Bias

2.1 Introduction

One of the most useful emitters of submillimeter-wave radiation is a fast photoconductor, or Auston switch, made of low-temperature-grown (LTG) GaAs. When a biased Auston switch is embedded in a transmission line or antenna, it transduces the intensity envelope of an input optical signal to an electrical signal that propagates down the transmission line or radiates into free space. Pulses of 0.9 ps duration have been launched on transmission lines by illuminating an Auston switch with a mode-locked laser [6], and continuous-wave output from DC to 3.8 THz has been realized by exciting an antenna-coupled Auston switch with the beat frequency of two overlapping, tunable laser beams ("photomixing") [7].

Due to the inherently high bandwidth of optical intensity modulation, the bandwidth of an Auston switch's output is limited by the switch's response time. Auston switches are usually planar, metal-semiconductor-metal photoconductors with very low capacitance, thus the output bandwidth is limited by the free-carrier lifetime

of the LTG GaAs photoconductive substrate. This material is well suited for high-bandwidth, high-average-power ($\sim 1\mu$W) emission because of its short carrier lifetime (~ 0.25 ps), its high electrical breakdown field ($> 5 \times 10^5$ V/cm) and the relatively high mobility (> 200 cm^2 V^{-1} s^{-1}) of its photogenerated electrons [8].

Auston switches generate maximum power when biased near their breakdown voltage. While the amplitude of the emitted electric field increases nearly linearly with increasing bias [9], the bandwidth of the emitted signal decreases after the bias crosses a threshold [9, 10]. The bandwidth decrease has been attributed to high-bias-field phenomena such as local heating due to high photocurrent density [9], and impact ionization [10]. The bandwidth decrease is an important technological problem because it limits the output power of photoconductive emitters such as photomixers at submillimeter-wave frequencies, which is precisely the band for which emitters are lacking.

Features in the DC I-V curves of illuminated Auston switches have been attributed to other high-bias phenomena such as injection-limited currents [11, 12] and velocity saturation [13]. While such phenomena influence the behavior of Auston switches under both static and dynamic illumination, a single physical model that predicts both types of behavior and incorporates high-bias effects has never been proposed. Such a consistent model is needed to pinpoint the cause of the decrease in bandwidth at high bias, and to shed light on how LTG GaAs can be grown to optimize submillimeter-wave generation. In this chapter we propose such a model and compare it to experimental data.

We begin the chapter with a discussion of the current understanding of LTG GaAs material and metal contacts to LTG GaAs. Then we discuss high-field effects caused by the contacts and by electron heating. We then describe the experimental LTG GaAs Auston switch, and describe the three types of experiments we performed: dark current measurements, and photocurrent measurements with both continuous and pulsed illumination. We attempt to model our data with various high-field effects, and find that the bandwidth decrease and increase in dc photocurrent at high bias are caused by the electric field and electron heating reducing the electron capture

cross section of recombination centers.

2.2 Low-temperature-grown GaAs

2.2.1 Band diagram of LTG GaAs

LTG GaAs is the photoconductor with the fastest known carrier relaxation time. It is grown by molecular beam epitaxy (MBE) in an As-rich environment with the substrate held at temperature of about 200 °C, as opposed to the usual substrate temperature of about 600 °C. A typical run includes a growth rate of 1 μm/hr on a (001)-oriented GaAs substrate, with an As_4/Ga beam equivalent pressure ratio of 10. First an undoped 5 μm-thick GaAs layer is grown at a normal substrate temperature of 600 °C to smoothen the growth front [14]. Next the substrate temperature is lowered to about 200 °C and from 1 to 2 μm of LTG GaAs are grown. The samples can then be removed from the MBE chamber, or annealed *in situ*, typically under As overpressure for 10 minutes at a substrate temperature of 600 °C.

Due to the low substrate temperature and the As-rich growth conditions, as much as 1% excess As is incorporated into the LTG GaAs lattice. The As atoms form a variety of point defects such as As antisites (As_{Ga}), As interstitials and Ga-related vacancies (V_{Ga}) [15]. The excess As causes unannealed LTG GaAs to have a lattice constant .1% greater than normal GaAs, as revealed by double crystal x-ray rocking curves [16]. When LTG GaAs is annealed, the concentration of point defects reduces, As precipitates form [17] and the lattice constant relaxes to its normal value [16]. Many studies have been made of how the growth and anneal temperatures of LTG GaAs control the concentrations of the various defects, and how those concentrations control key material parameters such as the carrier capture times and the conductivity.

The As antisites in LTG GaAs are believed to form a large density of donor-like states at midgap, .75 eV below the conduction band. This is because LTG GaAs shows a threshold of infrared absorption at 1.7 μm wavelength (.75 eV). The same infrared absorption experiments also indicate that the density of unionized As antisites (As^0_{Ga}) in unannealed LTG GaAs is about 10^{20} cm^{-3}, and in annealed LTG GaAs is an order of magnitude less [16]. Electron paramagnetic resonance (EPR) experiments reveal the presence of ionized As antisites (As^+_{Ga}) in unannealed LTG GaAs, with a density

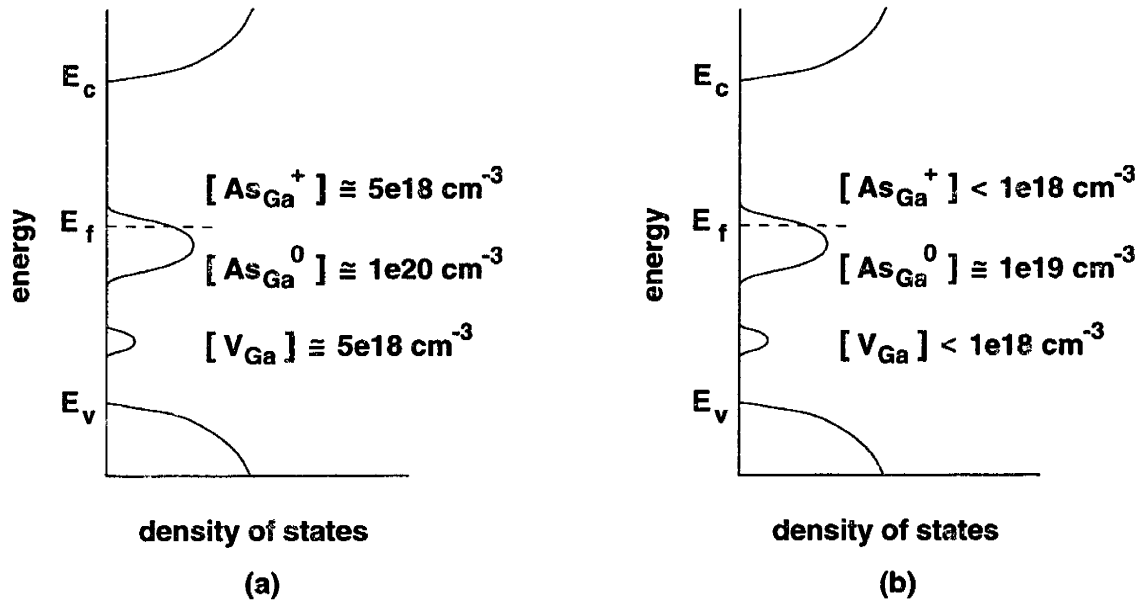

Figure 2-1: Density of states vs. energy models for both (a) as-grown and (b) annealed LTG GaAs

of about $5x10^{18}$ cm^{-3}. The concentration of As_{Ga}^{+} in annealed LTG GaAs is below the detection of threshold of $1x10^{18}$ cm^{-3} [16].

The existence of the As antisite donor states is confirmed by conductivity measurements. Unannealed GaAs grown at intermediate temperatures near 400 °C, as well as annealed LTG GaAs, show thermally activated conductivity with an activation energy of .75 eV [13, 16, 18, 19]. Single-carrier analysis of Hall-effect data imply that the carriers are electrons [16]. This shows that, near room temperature, the fermi level is pinned at the donor energy level, .75 eV below the conduction band. This fermi level pinning, as well as the existence of large densities of positively-charged As_{Ga}^{+}, imply that LTG GaAs is a compensated material, and must contain acceptors as well as donors. This acceptor is attributed by most authors [20] to V_{Ga}. It seems to be associated with a photoluminescence peak at 1.16 eV [16], and is therefore considered to reside about .3 eV above the valence band. The defects described above, As_{Ga} and V_{Ga}, play the major roles in determining the electronic properties of LTG GaAs. Therefore the density of states of both as-grown and annealed LTG GaAs are well described by the diagrams in Fig. 2-1, taken from [16].

Look *et al.* [18] fit data from Hall effect and conductivity measurements by consid-

ering LTG GaAs to be a compensated semiconductor with the fermi level pinned at the donor level. Look *et al.* found that the resistivity of as-grown LTG GaAs at room temperature was too low (20 Ωcm), and the value of the electron mobility extracted from the Hall coefficient was too low (1 cm^2/Vs) to be explained by the electrons in the conduction band. He showed that the high conductivity is due to electrons hopping from donor to donor, since the donor concentration is high enough (Look *et al.* calculated $3x10^{19}$ cm^{-3}) for the wavefunctions of electrons occupying donor atoms to overlap. Smith observed the same hopping conduction [16]. Like Smith, Look *et al.* observed that the donor density decreases by an order of magnitude after a 600 °C anneal. The resistivity increases drastically to $8x10^5$ Ωcm, and is due solely to electrons in the conduction band, because the electrons occupying donor atoms no longer overlap.

The mobility μ_e of electrons in the conduction band of annealed LTG GaAs is close to that of normal GaAs with large densities of dopants. Look *et al.* [21] measured the conductivity and Hall coefficient of 2-μm-thick layers of annealed LTG GaAs removed from their substrates, and calculated $\mu_e = 400$ cm^2/Vs. Other groups measured higher values between 1000 and 2000 cm^2/Vs [16, 18, 22], but these values may be enhanced by conduction in their SI GaAs substrates. The electron mobility appears to be limited by scattering from ionized As^+_{Ga} and V_{Ga} sites [21]. TEM images of annealed LTG GaAs reveal that the GaAs lattice is of good crystalline quality, with no defects such as dislocation lines or loops [14], thus we would expect the mobility to be limited by localized impurities or phonons. All groups measure a negative Hall coefficient for annealed LTG GaAs, and neglect the conduction of holes in the valence band on that basis. Since LTG GaAs is compensated material, this neglect may lead to inaccurately low values of μ_e, if the hole concentration is great enough to overcome the disparities in hole and electron mobilities. The fermi level is known from the activation energy of the conductivity, thus the hole concentration should be included in a self-consistent analysis of conductivity and Hall-effect data.

2.2.2 Photoresponse of LTG GaAs

The model of LTG GaAs shown in Fig. 2-1 explains well the D. C. current in both as-grown and annealed LTG GaAs, but can't adequately explain the complete set of measurements of the photoresponse of these materials. The photoresponse of as-grown and annealed LTG GaAs are quite different. Figure 2-2 shows the time-resolved differential transmission coefficient (at a photon energy 15 to 20 meV above the GaAs band gap) of both as-grown and annealed layers of LTG GaAs removed from their substrates and mounted on glass [23]. The x-axis shows the time delay between the pump and the probe optical pulses. The rise in transmission following an optical pulse is due to the filling of the conduction band by photogenerated carriers. The transmission coefficient is more sensitive to the transient electron concentration than the hole concentration because the density of states of the conduction band is 15 times less than that of the valence band. In as-grown LTG GaAs, photogenerated electrons leave the conduction band rapidly, with a capture time of about 200 fs, but the material doesn't return to its original state for approximately 1 ns. The photogenerated electrons in annealed LTG GaAs leave the conduction band with a slower capture time than in the as-grown material, but annealed LTG GaAs returns to its original state in only 10 to 30 ps. Gupta *et al.* made similar observations [15].

Lochtefeld *et al.* explained the above data as follows. In as-grown LTG GaAs, photogenerated electrons are trapped by As_{Ga}^{+} sites, and holes are trapped by V_{Ga} sites, both with capture times near 200 fs. This is in agreement with the observations of others, who observed that the concentrations of these point defects are very high in as-grown LTG GaAs [16, 20]. The long period of reduced transmission is due to extra absorption by trapped electrons during the time the trapped carriers slowly recombine. This is in agreement with the measurements of Sung *et al.* [24], who observed that trapped electrons in LTG GaAs also cause transient enhanced absorption of below-band-gap light, with a slower time constant than electron and hole capture.

The data in Fig. 2-2 provide no direct evidence that photogenerated holes in as-grown LTG GaAs are trapped rapidly, since the transmission coefficient is insensitive

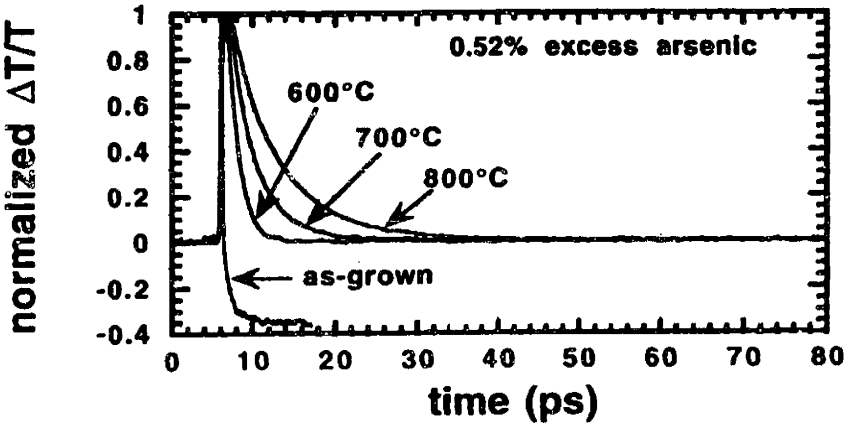

Figure 2-2: Normalized differential transmission from a pump-and-probe measurement of a GaAs epilayer containing 0.52% excess arsenic. Transients are shown for as-grown material and material annealed for 30 s at 600, 700 and 800 °C. Only the first 15 ps of the transient for the as-grown sample is shown. Taken from [23].

to the hole population. Lochtefeld *et al.* present other data to show that rapid hole trapping takes place. Figure 2-3 shows the time-resolved transmission coefficient of an as-grown LTG GaAs layer measured at a few pump pulse energies. The energies are high enough to create a greater density of free carriers than the two point defect densities, as evidenced the greater electron capture time for more intense illumination. This time is actually the hole capture time of As^0_{Ga}, since once all the As_{Ga} sites are filled by electrons and the V_{Ga} sites are filled by holes, only hole capture by As^0_{Ga} will allow further emptying of the conduction band. This hole capture time is about 60 ps, much faster than the 1 ns recombination time of the as-grown sample in Fig. 2-2. This proves that the captured electrons of as-grown sample in fig. 2-2 have no free holes to recombine with during the slow recovery; the holes must already be captured by V_{Ga} sites.

The annealed samples in fig. 2-2 show different capture and recombination dynamics than the as-grown sample. Their transient differential transmission coefficients decay to zero without any sign of a slow recovery. This indicates that the photogenerated electrons and holes in annealed LTG GaAs are captured by the same defect. It is well known that point defects are abundant in as-grown LTG GaAs, and that annealing reduces their densities [16, 20, 21]. During annealing, the As antisites

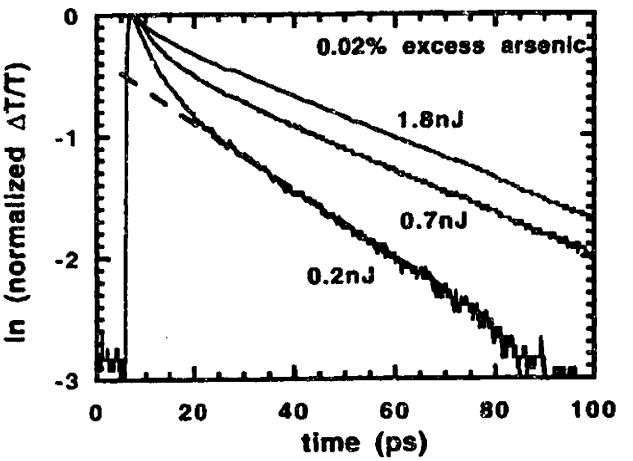

Figure 2-3: Normalized differential transmission at varying pump-pulse energy of an as-grown GaAs epilayer containing 0.02% excess arsenic. Taken from [23].

cluster and form precipitates [17, 25, 26]. The defects responsible for the distinct recombination dynamics of annealed LTG GaAs are therefore most likely to be As precipitates.

Since the electron capture time τ_e is an important figure of merit for high-speed LTG GaAs photoconductors, many authors have tried to find the growth temperature T_g and the anneal temperature T_a of LTG GaAs that minimize τ_e. In general, τ_e decreases with decreasing T_g for $T_g > 190\,^{\circ}\mathrm{C}$, because more excess As is incorporated into the GaAs lattice at low T_g, and both $\mathrm{As_{Ga}}$ and As precipitates capture electrons. Below $T_g = 190\,^{\circ}\mathrm{C}$, at which LTG GaAs tends to grow in polycrystalline form, τ_e increases [27].

Many groups have observed that annealing LTG GaAs only increases τ_e, as is shown in Fig. 2-2, and therefore they have focused their research on lightly annealed ($T_a \leq 600\,^{\circ}\mathrm{C}$) LTG GaAs to achieve both low τ_e and low hopping conductivity at room temperature [27]. Such material contains large densities of both $\mathrm{As_{Ga}}$ and As precipitates, so there is much debate over which defect is the dominant electron capture center. McIntosh *et al.* [27] measured the transient reflection coefficient of many samples of annealed LTG GaAs, and found that τ_e increases from 90 fs to 220 fs as T_a is increased from $480\,^{\circ}\mathrm{C}$ to $620\,^{\circ}\mathrm{C}$ at a fixed T_g of $215\,^{\circ}\mathrm{C}$. These capture times are the fastest ever measured. The one reflection transient McIntosh *et al.* show (for

LTG GaAs with $T_a = 580\,°C$) decays to zero rapidly, like the transients for annealed LTG GaAs in Fig. 2-2. Their lowest T_a is above 400 °C, the lowest T_a for which annealing has been observed to have any effect on LTG GaAs [21]. We assume the one transient McIntosh *et al.* show is typical, that As precipitation occurred during all of their anneals, and that electron capture in their material is dominated by As precipitates.

Harmon *et al.* studied LTG GaAs annealed at relatively high temperatures ($T_a \geq 600\,°C$), and observed a correlation between τ_e and the spacing and diameter of As precipitates. They measured the precipitate spacing and diameter by transmission electron microscopy (TEM) and calculated τ_e from time-resolved transmission measurements. Their data are shown in Table 2.1. The electron capture time is plotted as a function of the As precipitate spacing in Fig. 2-4. Harmon *et al.* note that the data show strong correlation, and fit well to a straight line, but don't explain what the exact dependence should be. The electron capture time is usually expressed as

$$\tau_e = \frac{1}{\sigma N v_t} \tag{2.1}$$

where N is the concentration of electron capture sites, σ is the capture cross section of those sites and v_t is the electron thermal velocity. If As atoms cluster such that the net atomic density remains constant, and each precipitate is modeled as a sphere, then the sphere diameter must increase in proportion to the precipitate spacing. If σ is proportional to the square of that diameter, then τ_e is linearly proportional to the precipitate spacing. However, as Fig. 2-4 shows, a linear fit to the data has a substantial offset from the origin, which the above model does not predict.

One suspect part of the above model is the assumption that σ is proportional to the square of the sphere diameter. We must consider the electrostatic potential near the As precipitates to determine their effective radius. Some authors have considered the As precipitates to be metallic clusters that act as Schottky diodes embedded in the GaAs lattice [25, 26]. Melloch *et al.* report that the Schottky barrier height is about .6 eV [26]. Since the fermi level is pinned .75 eV below the conduction band in the LTG

Table 2.1: Results of 30 s anneals of LTG GaAs grown at 250 °C, as determined by TEM analysis and transient transmission measurements. Taken from [17].

T_a (°C)	As precipitate spacing (nm)	As precipitate diameter (nm)	τ_e (ps)
700	39.6	10.2	2.8
800	50.9	13.2	5.1
900	61.9	16.7	7.1
1000	76.9	18.9	10.3

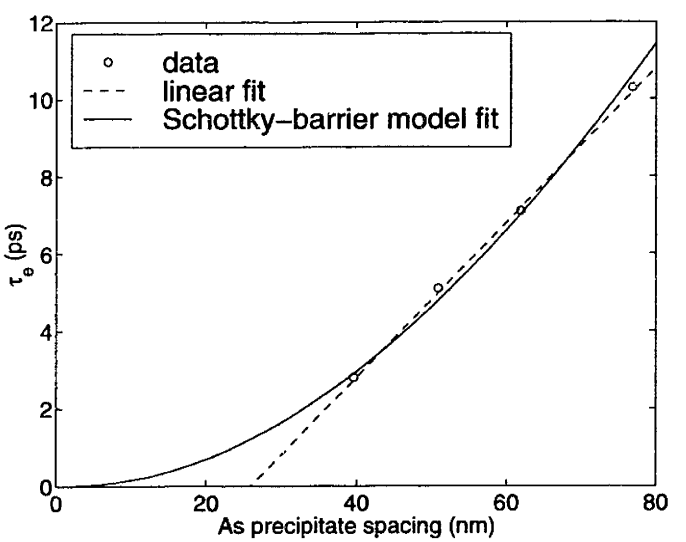

Figure 2-4: The relationship between electron capture time and As precipitate spacing in annealed LTG GaAs. A line and a model based on the attractive Schottky barrier around As precipitates are fit to the data. Data is taken from [17].

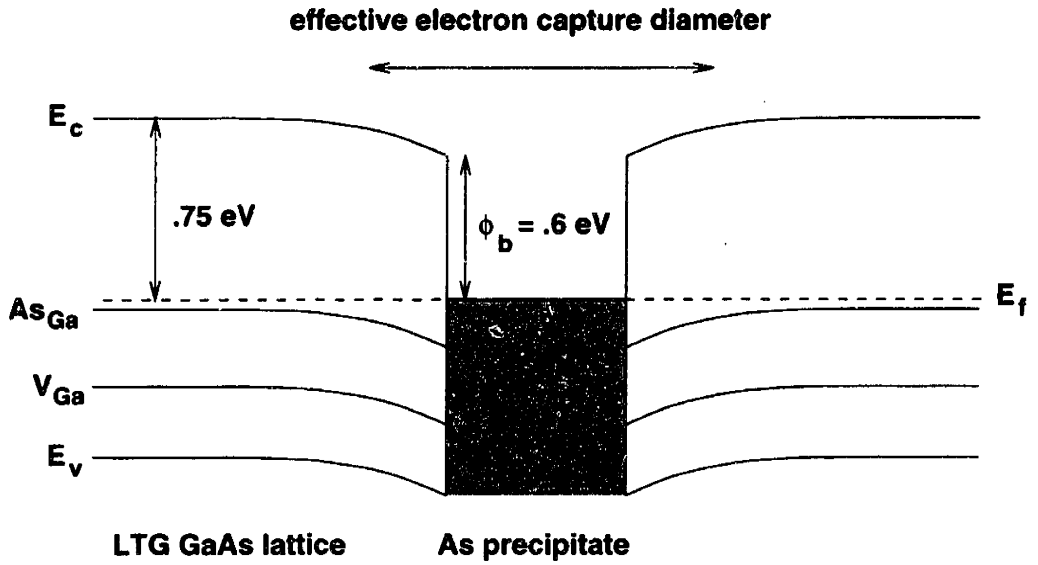

Figure 2-5: Band diagram of LTG GaAs in the vicinity of an As precipitate.

GaAs lattice, free photogenerated electrons are attracted to the As precipitates when they enter the depletion region surrounding each one. Figure 2-5 shows the band diagram of LTG GaAs in the vicinity of an As precipitate. The effective cross section of the precipitate extends to the edge of the depletion region. The full radius of the depletion region, r_d, is found by assuming that the charge density in the depletion region is uniform and solving Poisson's equation. The resulting equation is

$$V_0 = \frac{eN}{3\epsilon}(r_d^3/r_p + r_p^2/2 - 3r_d^2/2) \tag{2.2}$$

where V_0 is .15 V, the amount of band bending in the LTG GaAs; eN is the charge density in the depletion region, which we take to be a fitting parameter that stays constant with annealing; and r_p is the physical radius of the As precipitates, which Table 2.1 shows to be one eighth of the precipitate spacing for all T_a. We find the roots of Eq. 2.2 to get r_d as a function of r_p, N and V_0, then let $\sigma = \pi r_d^2$ to calculate τ_e. We obtain a good fit to the data when $N = 10^{18}$ cm^{-3} and $v_t = 3.2\text{x}10^6$ cm/s, as shown in Fig. 2-4. The value of N agrees with the concentration of V_{Ga} in annealed LTG GaAs. The ionized V_{Ga} sites supply the negative charge that causes band bending. The value of v_t is about an order of magnitude less than $\sqrt{3kT/m^*}$, the known thermal

velocity of electrons. Perhaps the effective capture radius of the As precipitates does not extend all the way to the edge of the depletion region, and we have exaggerated σ, and compensated by lowering v_t. Also, the effective cross section σ is actually less than πr_d^2, because σ includes the probability that an electron emits a phonon to be captured by a trap once it encounters one.

Melloch *et al.* observed positive curvature in plots of measured τ_e vs. As precipitate spacing [26], similar to the positive curvature in the Schottky-barrier model fit in Fig. 2-4. In their view, Eq. 2.1 doesn't apply to As precipitates, because precipitates probably have multiple ionization states, and Eq. 2.1 is for traps with only one ionization state. They propose that precipitates act as sinks for electrons, and that the capture rate is limited by diffusive transport to the precipitates. They state that in the diffusive transport limit, τ_e is proportional to the square of the precipitate spacing, and thereby explain the positive curvature of their plots. They offer no model to fit their data.

Measurements of LTG GaAs under continuous illumination also yield information about capture and recombination dynamics. Stellmacher *et al.* [22] measured the conductance and Hall coefficient of annealed samples of LTG GaAs uniformly illuminated by a laser with a wavelength of 859 nm. They measured a negative Hall coefficient at all levels of illumination and temperature, indicating that electrons are always the dominant conductor. This is further evidence that some defects in annealed LTG GaAs have comparable electron and hole capture rates, since the valence band doesn't fill up with holes waiting to recombine with electrons. The fast hole traps that Lochtefeld *et al.* claim exist in as-grown LTG GaAs, which seem to have no communication with electron traps or the conduction band, play no role in continuous illumination experiments because they don't determine the steady-state hole population. That population is determined by the recombination mechanisms that link the two bands and relax photogenerated electrons. The fast hole traps trap some holes to maintain a separate dynamic equilibrium with the valence band.

More information about hole capture in annealed LTG GaAs was obtained by Sung *et al.* [24]. They performed time-resolved transmission measurements at a wave-

length of 760 nm to probe the valence band. They measured hole capture times as short as 700 fs, only a factor of two higher than τ_e. They considered this to be a hole trapping time because a slow transient related to recombination was observed at optical pulse energies high enough to saturate the traps. Zhou *et al.* [28] were able to measure both the electron and hole capture times by doing a luminescence correlation experiment. They measured equal capture times of 1 ps. They were unable to discriminate between carrier trapping and carrier recombination.

2.2.3 Metal contacts to LTG GaAs

Nearly every type of metalization, including Ti/Au, Ni/Ge/Au and In/Au, forms a low-resistance ohmic contact to both as-grown and annealed LTG GaAs without alloying [16]. Alloying the contact does not influence the characteristics of photoconductors fabricated on LTG GaAs [16]. This is very convenient, because metal-semiconductor-metal photoconductors can be fabricated directly on LTG GaAs without a highly doped layer to facilitate contact and without a high-temperature alloying step that would alter the characteristics of the LTG GaAs.

The low contact resistance is due to the deep donor states in LTG GaAs (see Section 2.2.1). As shown in Fig. 2-6(a), an electron residing in the deep donor band at the fermi level must overcome a small barrier to reach the donor states at the interface and enter the metal. The barrier height $q\phi = q\phi_b - (E_C - E_T)$, where $q\phi_b$ is the Schottky barrier height, assumed to be .8 eV, and E_c and E_T are the energy levels of the conduction band and the deep donors, respectively. As discussed in Section 2.2.1, $E_C - E_T$ is approximately .75 eV, thus $q\phi \approx .05$ eV, much lower than the Schottky barrier height. Electrons in the metal must overcome the same small barrier $q\phi$ to flow into the LTG GaAs. For forward biases greater than ϕ, shown in Fig. 2-6(b),the donor states at the interface are filled and the electrons there face no barrier to enter the metal. The thermionic emission of electrons from the metal into empty donor states, which is the dominant conduction mechanism under reverse bias, is shown in Fig. 2-6(c).

Yamamoto *et al.* [29] modeled the emission of electrons from the donor states into

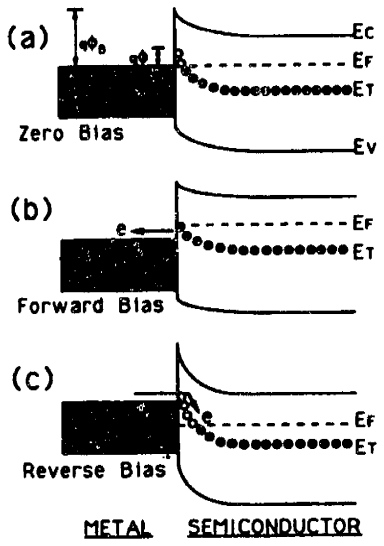

Figure 2-6: Band diagram of the metal-LTG GaAs contact. Taken from [29].

the metal by modifying standard thermionic emission theory. Their theory includes the low barrier $q\phi$, and contains an effective electron velocity due to hopping conduction within the donor band rather than the thermal velocity. They fabricated a standard transmission line model (TLM) pattern of nonalloyed Ni/Ge/Au on a 5-μm-thick layer of as-grown LTG GaAs, and measured the contact resistance and the resistivity of the LTG GaAs layer at different temperatures. They fitted their model to the data and extracted a $q\phi$ of .12 eV. This corresponds to a Schottky barrier height of .87 eV, which is a reasonable value. The resistivity of their LTG GaAs at room temperature was 30 Ω cm, a very high value indicative of enough hopping conduction to supply the forward-bias current in the contact. The measured specific contact resistivity at room temperature was $1.5\text{x}10^{-3}$ Ω cm^2.

The specific contact resistivity of metal on annealed LTG GaAs has never been measured. If Yamamoto's theory is correct, we would expect it to be higher than the value above because the hopping conduction in annealed LTG GaAs is much less than in as-grown LTG GaAs, and hopping electrons in the donor band are the source of trans-interface current. We will report our data in Section 2.4.

Contact effects in MSM photodetectors on LTG GaAs is another unexplored yet important topic. Most authors assume that the voltage drop at the contacts of such

devices is negligible. Most authors also assume that such devices are photoconductors and not photodiodes, because the photocurrent never appears to saturate as the voltage bias increases. That implies that the contacts can inject electrons and holes to replace carriers that drift to the contacts. Other authors invoke effects such as electric field screening [30] that imply charge neutrality is not always maintained and that the contacts are not injecting. It's important to clearly define the behavior of a device's anode and cathode, so one can derive the boundary conditions on current transport in the bulk.

Yamamoto's model describes a low-resistance contact that readily injects electrons at a cathode and does not block the exit of electrons at the anode or holes at the cathode. Not only is the barrier to electron transport between the metal and donor band small, but the depletion layer width is very narrow. The positive charge in the depletion region is that of ionized donors, which have a density N_d of about 10^{19} cm^{-3}. For band bending $\phi = .05$ V, the depletion region width is approximately $\sqrt{2\phi\epsilon/eN_d} = 2.7$ nm, where ϵ is the constant of GaAs and e is the electron charge. The barrier is thin enough for tunneling to be important, assisted by the mid-bandgap donor states. The band bending is small enough for both electrons and holes to drift out of the bulk of a device without being blocked.

From the above description, we can derive the boundary conditions for current flow in an LTG GaAs device with metal contacts. The cathode is an electron injector, therefore the boundary condition at the cathode contact is that the electric field is zero [31]. There is a large excess concentration of injected electrons near the cathode, much like in the p-region of a forward-biased p-n junction, thus the electric must be low to keep the electron drift current near the cathode equal to its value in the bulk. In the limit of a perfectly injecting cathode, the electric field right at the contact is zero.

The anode, however, is not a source of holes. Therefore the boundary condition at the anode contact is that the hole current is zero. When the hole concentration in the bulk of a device is appreciable, for example in an illuminated device, the part of the bulk near the anode must have a non-zero net generation rate of free carriers

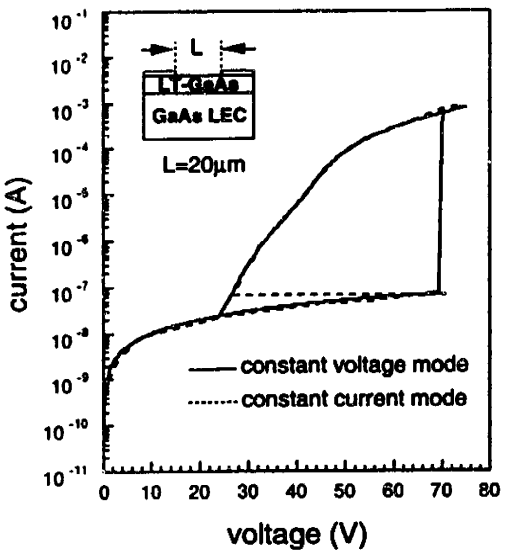

Figure 2-7: I-V curve of a 1-μm-thick planar LTG GaAs device. Taken from [33].

to supply the hole current in the bulk. The electrons and occupied recombination centers in that region adjust their concentrations to reduce the recombination rate, and in doing so the region becomes charged, and the electric field near the anode rises above its value in the bulk. This is the source of the anode field enhancement observed in semi-insulating devices similar to LTG GaAs [32].

There is experimental evidence that a metal contact on LTG GaAs does not inject holes, except in extreme conditions. Shiobara *et al.* [33] measured the I-V curve of a nonilluminated, planar conductor of annealed LTG GaAs with alloyed Au/Ge/Ni contacts. Their data are shown in Fig. 2-7. At low constant-voltage or constant-current biases, their device shows ohmic behavior. Once the device breaks down at high voltage bias, the device gains a new I-V characteristic, with a much greater current at a given bias than before breakdown. This is a sign that a substantial number of holes are injected at the anode after breakdown, which neutralize injected electrons to lower space charge and reduce the voltage at a given current [1]. Hole injection occurs because of impact ionization or barrier lowering due to the high field at the anode, but only after that field is over a threshold. Hole injection due to

[1]See [31] for a description of devices with "double injection"

impact ionization tends to cause an S-shaped I-V curve [34], while hole injection due to barrier lowering tends to cause a steep rise in current without negative differential resistance [32].

2.2.4 Contact effects in LTG GaAs

Now that we have established how metal contacts to LTG GaAs function, we will explore the high-field effects that occur when the carrier and electric field distributions near the contacts dominate the total device behavior. We begin with injection effects at the cathode; namely space-charge-limited (SCL) current and trap filling. These are effects that have been observed in trap-laden insulators [31] and semi-insulating semiconductors [34] that are similar materials to LTG GaAs. Some authors have claimed these effects are evident in LTG GaAs devices [11, 13], however we believe their explanations are incorrect, as we shall explain below. We will at first assume that hole current is negligible, which makes the anode boundary condition unimportant. We will discuss the influence of the anode later.

To elucidate the two phenomena of SCL current and trap filling, we take the model device of Corvini *et al.* as an example, for in this device the two phenomena have distinct influences on the I-V curve. Corvini *et al.* modeled the n-SI-n device made of InP whose doping levels and band diagrams at zero bias are shown in Fig. 2-8 (a). The n regions at the cathode and anode are doped highly enough with shallow donors to serve as electron injectors. The Fe atoms in the SI region form deep acceptors, which compensate a lesser concentration of shallow donors. At equilibrium, the donors in the SI region are fully ionized, and the acceptors are partially ionized such that $N_a^- = N_d$ and the region is charge neutral. This places the fermi level an energy $\frac{kT}{q}\ln(\frac{N_a}{N_d})$ below E_a, far enough below E_c to make this region very resistive (for $N_c = 5.4\text{x}10^{17}$ cm^{-3} and $E_c - E_a = .59$ eV, as given in [34], the electron concentration $n = 9\text{x}10^5$ cm^{-3}). Conduction by holes is negligible in this device because neither of the contacts are hole reservoirs and the concentration of thermally-generated holes in the SI region is very low.

The bottleneck for current transport through this device is obviously the SI region.

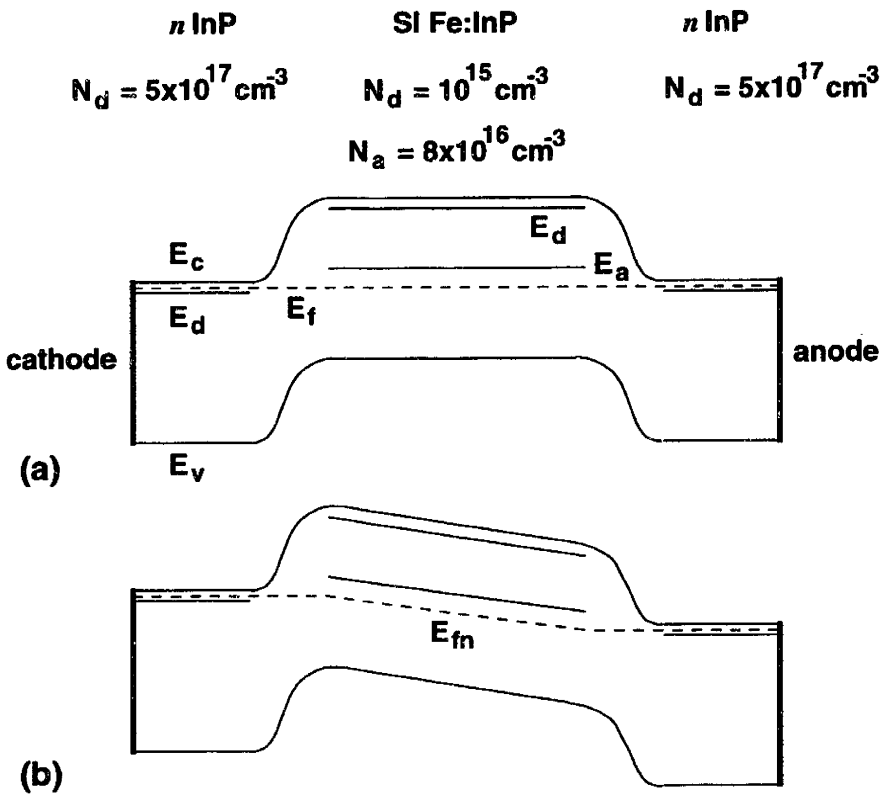

Figure 2-8: Band diagrams of an InP n-SI-n device at (a) zero bias and (b) moderate non-zero bias. The fermi level is drawn in (a), whereas only the electron quasi fermi level is drawn in (b). As described in [34].

We expect an applied voltage bias to drop there. The band diagram at moderate bias is shown in Fig. 2-8 (b). The electron quasi fermi level is flat in the depletion region next to the cathode because over-the-barrier emission of electrons supplies ample current to the SI region. That depletion region maintains its zero-bias shape because no barrier lowering is necessary to supply current. Thus the electric field at the edge of the depletion region is zero, which is the cathode boundary condition discussed in the last section. The anode is simply an electron collector, thus the anode's depletion region is free to change its shape to make the entire device charge neutral.

When there is an applied bias, some negative charge must exist near the cathode to source the electric field in the SI region. We stated above that the depletion region near the cathode is not altered by an applied bias, so the extra negative charge can't reside there; therefore it must reside in the SI region. At a given bias voltage, E_{fn} rises towards E_c to create the charge needed to drop the voltage. In general, this will cause the free electron concentration n to rise and the acceptors to fill. It has negligible effect on the shallow donors. As long as n stays low enough that the SI region is highly resistive, then our original assumption of perfectly injecting contacts is valid.

To simplify analysis of the device under bias, we assume that $E_c - E_{fn}$ is uniform throughout the SI region. In reality, $E_c - E_{fn}$ is such that the current continuity equation and Poisson's equation are obeyed. Solving these equations does not bring to light any unique device behavior, though it is necessary if one considers very short SI regions or impact ionization [34]. We first consider biases such that $E_a - E_{fn} > 2kT$. In this case

$$n = N_c \exp(\frac{q(E_{fn} - E_c)}{kT}), \tag{2.3}$$

$$N_a^+ = N_a \exp(\frac{q(E_{fn} - E_a)}{kT}) \text{ and} \tag{2.4}$$

$$\frac{n}{N_a^-} = \theta = \frac{N_c}{N_a} \exp(\frac{q(E_a - E_c)}{kT}). \tag{2.5}$$

In the device of Fig. 2-8, with a high concentration of deep acceptors, $\theta \ll 1$ (With

the densities and energies given, $\theta = 10^{-9}$). The charge density ρ in the SI region is

$$\rho = e(p + N_d^+ - n - N_a^-) \approx e(N_d - N_a^-). \tag{2.6}$$

The charge density is related to the voltage bias V and the length L of the SI region as

$$V = \frac{-L^2\rho}{2\epsilon}, \tag{2.7}$$

thus the relationships between N_a^- and V and n and V are

$$N_a^- = N_d + \frac{2\epsilon}{eL^2}V \quad \text{and} \quad n = \theta N_a^- = \theta N_d + \frac{2\theta\epsilon}{eL^2}V. \tag{2.8}$$

Eq. 2.8 shows that for $V < \frac{L^2 eN_d}{2\epsilon}$, n is virtually independent of V. The current density $J = en\mu_e\frac{V}{L}$, so for low bias, J is proportional to V. This current is carried by the thermally generated electrons that exist at zero bias. For $V > \frac{L^2 eN_d}{2\epsilon}$, n is approximately proportional to V, and J is proportional to V^2. This type of current arises because the charge distribution within the SI region is altered significantly by the applied bias, and hence is termed space-charge-limited current.

The above equations hold true and n, N_a^- and ρ increase linearly with V until E_{fn} rises above E_a. At this point $N_a^- \approx N_a$, (and $n \approx \theta N_a$) and the acceptors can not supply more negative charge. Poisson's equation dictates that ρ remain proportional to V, and only n can supply more negative charge, so n rises from θN_a to N_a within a voltage bias change of only a few $\frac{kT}{q}$. This leads to a rapid rise in current since θ is very small and n changes by many orders of magnitude. This occurs at the voltage bias that corresponds to $\rho = N_a$, which is $V = \frac{L^2 eN_a}{2\epsilon}$. The current increase is so dramatic that the device appears to break down. The voltage bias at which the I-V curve is nearly vertical is termed the trap-filled-limit voltage because the rapid increase in current is due to the filling of the deep acceptors. The prototypical I-V curve of a device that displays both SCL current and trap filling is shown in Fig. 2-9.

Let us now discuss what kinds of charge-related effects we expect to observe in LTG GaAs photoconductors. LTG GaAs is a compensated material like Fe:InP, except that

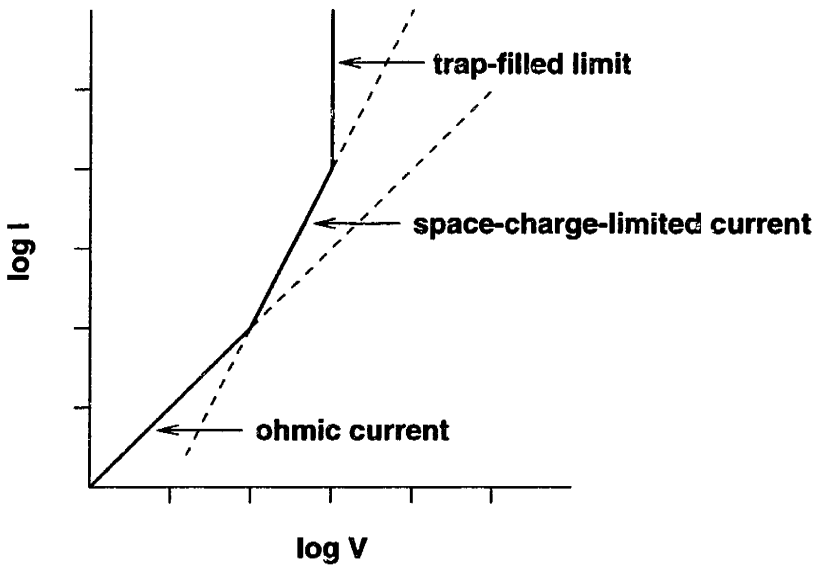

Figure 2-9: Prototypical I-V curve of a n-SI-n device, showing three distinct regimes.

it contains deep donors which compensate shallow acceptors, as shown in Fig. 2-1. Metal contacts to LTG GaAs are similar to the n-type contacts to Corvini's device in that they function as low-resistance injectors and sinks of electrons, as discussed in Section 2.2.3. We first consider the case with no illumination and negligible hopping conduction, such that $J = en\mu_e\frac{V}{L}$ (hole current is again negligible). At zero bias E_f is about 60 meV above E_d, such that the deep donors are partially ionized, the acceptors are fully ionized and $N_d^+ = N_a^- = N_a$. At non-zero bias, Eq. 2.3 holds true for LTG GaAs, but the counterpart of Eq. 2.4 is now

$$N_d^+ = N_d \exp(\frac{q(E_d - E_{fn})}{kT}) \tag{2.9}$$

and the counterpart of Eq. 2.5 has a different form:

$$nN_d^+ = \Theta = N_c N_d \exp(\frac{q(E_d - E_c)}{kT}). \tag{2.10}$$

The charge density ρ is slightly different from Eq. 2.6 to account for the different type of compensation in LTG GaAs:

$$\rho = e(p + N_d^+ - n - N_a^-) \approx e(N_d^+ - N_a). \tag{2.11}$$

Equation 2.7 still correctly relates V, L and ρ, but the relationships between N_d^+ and V and between n and V are now

$$N_d^+ = N_a - \frac{2\epsilon}{eL^2}V \quad \text{and} \quad n = \frac{\Theta}{N_d^+} = \frac{\Theta}{N_a - \frac{2\epsilon}{eL^2}V} \tag{2.12}$$

The last equation indicates that for $V < \frac{L^2 eN_a}{2\epsilon}$, n is approximately constant, and $J \propto V$. For $V > \frac{L^2 eN_a}{2\epsilon}$, more negative charge density is required than $-eN_a$. This can only be supplied by free electrons, so n rises rapidly and the I-V curve becomes nearly vertical due to the filling of the deep donors. There should be no region of the I-V curve where $J \propto V^2$, unlike the case with SI Fe:InP.

Ibbetson *et al.* [13] measured the I-V curves of an annealed, non-illuminated LTG GaAs device like that discussed above, with a length L of 2 μm. The low conductivity of their LTG GaAs, as well as the .75 eV thermal activation energy of the conductivity indicate that conduction in their material is due to free electrons and not hopping electrons in the deep donor states. They observed current saturation at $V = 1$ V, followed by a steep rise in current at $V = 30$ V. They attributed the current saturation to velocity saturation of the free electrons at an electric field of 5x10^3 V/cm. They fit their data to a model that is exactly the same as the one above, except they used the following velocity-field relationship:

$$v(E) = \begin{cases} \mu_0 E, & 0 \leq E < E_{\text{sat}} \\ v_{\text{sat}}, & E \geq E_{\text{sat}} \end{cases}, \tag{2.13}$$

where μ_0 is the low-field mobility, v_{sat} is the saturation velocity, and $v_{\text{sat}} = \mu_0 E_{\text{sat}}$. Even with velocity saturation, a steep rise in current should occur at $V = \frac{L^2 eN_a}{2\epsilon}$ due to trap filling, as dictated by Poisson's equation [2]. If this is the cause of the sharp rise in current at $V = 30$ V, then $N_a = 10^{16}$ cm^{-3}. Ibbetson *et al.* believed that the acceptor density must be higher than that (similar material grown by other groups

[2]In [13], Ibbetson *et al.* imply that velocity saturation and SCL current are related phenomena. This is not true: velocity saturation is a hot-electron effect that involves only the electron *velocity*, SCL current derives from Poisson's equation and involves only the electron *density*.

has $N_a \approx 10^{17} - 10^{18}$ cm^{-3} [20, 21]), and so they attributed the steep rise in current to field ionization of filled donor states.

We now consider the case where hopping conduction is the dominant form of electron transport. Most authors that treat hopping conduction don't explicitly write the flux as a product of a concentration times a velocity [18], but we will write it as $J \propto N_d^+ N_d^0 V$. The N_d^0 term represents the concentration of electrons that respond to the applied field. Their effective velocity is proportional to V because the hopping probability increases linearly with electric field. The N_d^+ term appears in the expression for J because the electrons must have empty donor states to hop to. Equation 2.12 still gives the correct relationship between N_d^+ and V, but now we ignore both n and p because they don't contribute appreciably to the current. The expression for the current density is then

$$J \propto (N_a - \frac{2\epsilon}{eL^2}V)(N_d - N_a + \frac{2\epsilon}{eL^2}V)V. \tag{2.14}$$

At low bias, J is proportional to V, and we predict the ohmic current that is most often observed. Near $V = \frac{L^2 e N_a}{2\epsilon}$, the current reaches a maximum and then decreases as the donor states fill. Beyond this voltage Eq. 2.14 is not valid. The free electron concentration increases rapidly to supply negative charge and begins to dominate conduction. While our formula for hopping conduction is too simple to predict the I-V curve near the critical voltage of $\frac{L^2 e N_a}{2\epsilon}$, its prediction that the current is ohmic at lower voltages is probably correct: space-charge effects will not be evident until the critical voltage is reached. Kordoš *et al.* [19] claimed to observe a suppression of hopping conduction in annealed LTG GaAs due to electron injection at the cathode. They observed that long devices had high conductance and that short devices more prone to injection effects had lower conductance (the threshold length was about 3 μm). However, in short devices, they did not observe a threshold voltage for the suppression of hopping current, which would have been the signature of injection-related conduction.

Whether free electrons and holes in LTG GaAs are generated thermally or op-

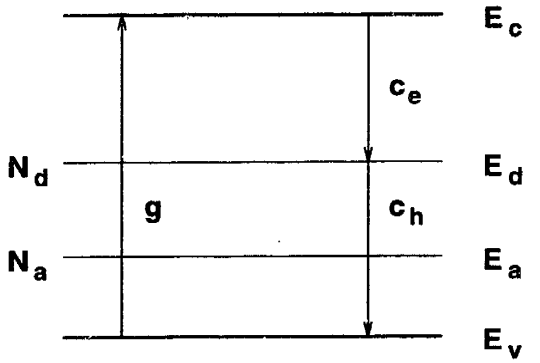

Figure 2-10: Band diagram of LTG GaAs, showing important carrier generation and capture mechanisms. g is generation of carriers by light, c_e is electron capture by empty donor states, and c_h is hole capture by filled donor states.

tically, the space-charge effects should be the same, as long as n and p are small compared to N_a and N_d, so that ρ can be written as in Eq. 2.11. This will be the case when an LTG GaAs device is illuminated by a continuous-wave (cw) laser. As the voltage bias increases, Poisson's equation is satisfied by small changes in N_d^+, n and p stay relatively constant, and the current increases linearly (unless the carrier velocity saturates) until the critical voltage $\frac{L^2 e N_a}{2\epsilon}$. At that point the current rises dramatically due to filling of the donor states.

We now examine our assumption that contact effects at the anode are negligible. As discussed in the last section, the boundary condition at the anode is that the hole current density J_h is zero. This boundary condition should have the most influence on an illuminated device, because under illumination the steady-state hole concentration is greater than or equal to the steady-state electron concentration, since the hole capture time by recombination centers in LTG GaAs is greater than or equal to the electron capture time [22, 23]. We made a one-dimensional model to calculate the electric field and carrier distributions within an illuminated LTG GaAs conductor with metal contacts. The model is based on the LTG GaAs band diagram shown in Fig. 2-1. The important carrier generation and capture mechanisms are shown in Fig. 2-10. We assume that the donors are the dominant recombination sites [22, 23], and that recombination at the acceptors is negligible. While As precipitates are important recombination centers in annealed LTG GaAs, in lightly annealed material

such as ours precipitates are indistinguishable from donor states [35], so we neglect them. The carrier capture rates are given by the following formulas:

$$c_e = nN_d^+\sigma_n v_t \tag{2.15}$$

$$c_h = pN_d^0\sigma_p v_t, \tag{2.16}$$

where n and p are the carrier concentrations, N_d^+ is the concentration of unoccupied donors, N_d^0 is the concentration of occupied donors, σ_n is the electron capture cross section of an unoccupied donor, σ_p is the hole capture cross section of an occupied donor, and v_t is the free carrier thermal velocity. Thermal generation of electrons and holes is negligible at the illumination intensities we will consider. We assume that the acceptors are only in communication with the valence band, and that the concentration of holes is never high enough to empty the acceptors of electrons. Thus we assume the acceptors are always fully ionized, as they are at thermal equilibrium due to compensation by the donors. We neglect diffusion currents, as the electric fields we consider are very high, thus we write the electron and hole currents as

$$J_e = en\mu_e E \tag{2.17}$$

$$J_h = ep\mu_h E, \tag{2.18}$$

where μ_e and μ_h are the electron and hole mobilities and E is the electric field. In steady state, the time derivatives of n, p and N_d^+ must all be zero. This is expressed as follows:

$$\frac{dn}{dt} = 0 = g - c_e - \frac{1}{e}\frac{dJ_e}{dx} = g - nN_d^+\sigma_n v_t - \mu_e(n\frac{dE}{dx} + E\frac{dn}{dx}) \tag{2.19}$$

$$\frac{dp}{dt} = 0 = g - c_h + \frac{1}{e}\frac{dJ_h}{dx} = g - pN_d^0\sigma_p v_t + \mu_h(p\frac{dE}{dx} + E\frac{dp}{dx}) \tag{2.20}$$

$$\frac{dN_d^+}{dt} = 0 = c_h - c_e = pN_d^0\sigma_p v_t - nN_d^+\sigma_n v_t \tag{2.21}$$

Table 2.2: Physical quantities in model.

quantity	value	units	quantity	value	units
N_d	$5\text{x}10^{19}$	cm^{-3}	v_t	$3\text{x}10^{7}$	cm/s
N_a	10^{19}	cm^{-3}	g	10^{26}	$cm^{-3}s^{-1}$
σ_n	$1.7\text{x}10^{-14}$	cm^2	μ_e	200	cm^2/Vs
σ_p	10^{-15}	cm^2	μ_h	10	cm^2/Vs

Poisson's equation must also be obeyed, in the form below:

$$\frac{dE}{dx} = \frac{e}{\epsilon}(p - n + N_d^+ - N_a^-) = \frac{e}{\epsilon}(p - n + N_d^+ - N_a) \tag{2.22}$$

If we know n, p and E at a given point in space, we can calculate N_d^+ with Eq. 2.21, then calculate the spatial derivatives of n, p and E with Eqs. 2.19, 2.20 and 2.22. Given three initial conditions, we can numerically integrate to find n, p and E throughout a device. Those three degrees of freedom correspond to the total current density J, which is constant throughout a device, and the boundary conditions at the anode and cathode.

The values of the physical quantities used in our model are listed in Table 2.2. At thermal equilibrium, charge neutrality makes $N_d^+ = N_a$, so the electron capture time $\tau_e = 1/N_d^+\sigma_n v_t = 200$ fs and the hole capture time $\tau_h = 1/N_d^0\sigma_n v_t = 830$ fs. These are comparable with values in the literature, as are the defect density values and the value of μ_e [21]. The value of σ_n is slightly greater than that reported by Lochtefeld *et al.* ($7\text{x}10^{-15}$ cm^2 [23]). The hole mobility of LTG GaAs has never been measured, but we estimated μ_h by multiplying μ_e by the mobility ratio μ_h/μ_e of normal GaAs, which is 1/20 [36]. This scaling is appropriate since ionized impurity scattering is known to degrade μ_e and μ_h proportionately [36] . The value of g is comparable to that induced by typical cw illumination of LTG GaAs photoconductors.

We calculated the distributions of many quantities of interest in an illuminated $3\text{x}10^{-7}$-cm-long conductor at a current bias $J = 7.72$ A/cm^2. The results are shown in Fig. 2-11. The anode is at $x = 0$, and influences the region for which $x < 1.5\text{x}10^{-7}$. The cathode is at $x = 3\text{x}10^{-7}$, and influences the region for which $x > 2.3\text{x}10^{-7}$. The

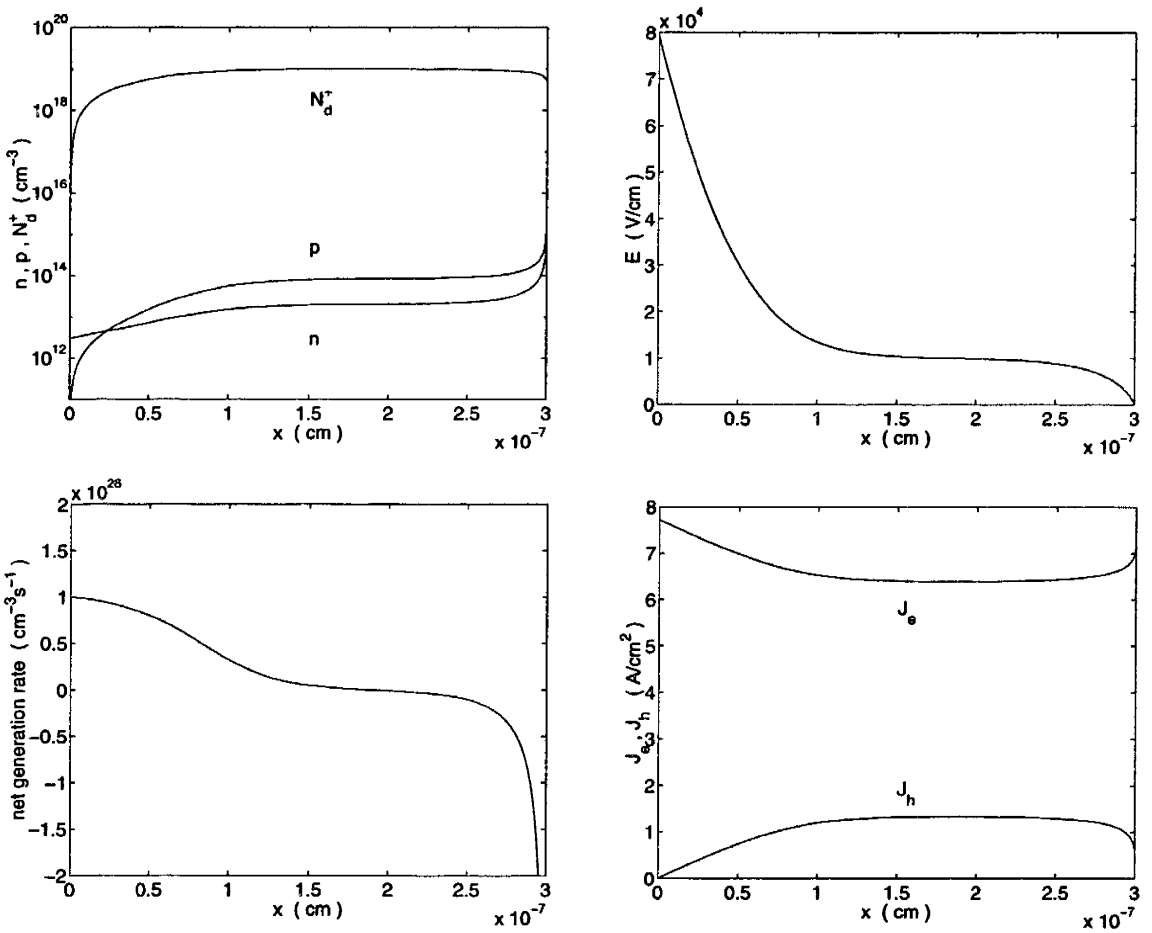

Figure 2-11: Calculated distributions of n, p, N_d^+, E, J_e, J_h and the net generation rate ($g - nN_d^+\sigma_n v_t$) in an illuminated 3x10^{-7}-cm-long device at a current bias $J = 7.72$ A/cm^2. The anode is at $x = 0$, where J_h must be zero. The cathode is at $x = 3\text{x}10^{-7}$, where E must be zero.

region in between, for which $1.5\text{x}10^{-7} < x < 2.3\text{x}10^{-7}$, is the charge-neutral bulk of the device, where $n = g\tau_e$, $p = g\tau_h$ and $N_d^+ = N_a$. The current bias was chosen such that the electric field in the bulk is 10^4 V/cm. The simulated device is so short to make contact effects prominent at applied electric fields used in practice. Any longer device at the same current bias would have the same distributions at the contacts and a longer charge-neutral region.

The cathode region is in agreement with our earlier discussion. In this region $N_d^+ < N_a$, so there is a net negative charge. This charge exists so that the electric field can rise up from zero at the cathode to its bulk value, therefore the space charge region has a length of $eE_{\text{bulk}}/\epsilon N_a$, to satisfy Poisson's equation. Injection at the cathode will dominate the device when the space charge region extends across it's entire length, when the device has a uniform negative charge density eN_a. This corresponds to a voltage of $V = \frac{L^2 eN_a}{2\epsilon}$, where L is the device length. This is the same threshold voltage for trap filling that we derived earlier in this section.

Near the anode, $\frac{1}{e}\frac{dJ_h}{dx}$ is constant at g, its maximum possible value, so that $J_h = 0$ at $x = 0$. We then can estimate the length of the charged region near the bulk as $J_{h,\text{bulk}}/eg = eg\tau_h\mu_h E_{\text{bulk}}/eg = \tau_h\mu_h E_{\text{bulk}}$. Like the cathode region, the anode region is negatively charged, since $N_d^+ < N_a$, because the donor states fill with electrons that lack holes to capture. The negative charge density near the anode is again approximately eN_a. The electric field near the anode is greater than E_{bulk}, therefore the effect of the anode boundary condition is to increase the voltage at a given current bias, making the I-V curve roll off. This saturation-type behavior is similar to the behavior of MSM photodiodes, which have non-injecting contacts similar to the anode of our model device.

We now estimate the bias voltage at which the voltage drop at the anode becomes appreciable, while neglecting electron injection at the cathode. The voltage drop across the device due to the bulk field is $E_{\text{bulk}}L$. The extra voltage drop at the anode is $\frac{1}{2}(\tau_h\mu_h E_{\text{bulk}})^2\frac{eN_a}{\epsilon}$. At the critical bias voltage, the two contributions are equal. We

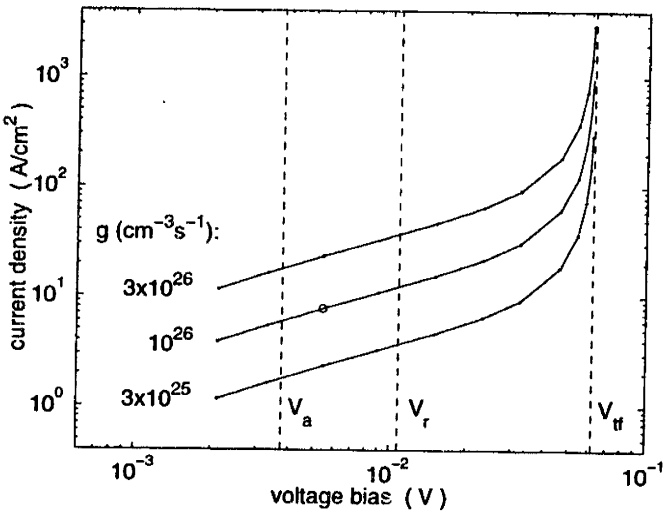

Figure 2-12: I-V curves of the simulated device at three different optical generation rates (g). V_a is the threshold voltage for appreciable voltage drop at the anode, V_{tf} is the trap filling voltage, and V_r would be the threshold voltage for recombination-limited current, which doesn't take place in this device. The bias point and g of Fig. 2-11 is indicated with a circle.

find the critical voltage by solving the following equations for V:

$$E_{\text{bulk}}L = V/2 = \frac{1}{2}(\tau_h \mu_h E_{\text{bulk}})^2 \frac{eN_a}{\epsilon} \tag{2.23}$$

The solution is $V = 4\epsilon L^2/eN_a\tau_h^2\mu_h^2$.

We can now explain the model device's calculated I-V curves, shown in Fig. 2-12. We calculated I-V curves at three different optical generation rates g, and found that the current is proportional to g at all voltages, as seen in the Figure. The current is ohmic for $V < V_a$, where V_a is the threshold voltage for appreciable voltage drop at the anode due to space charge. For $V > V_a$, the current increases as $V^{\frac{1}{2}}$, until the dramatic increase at V_{tf}, the trap filling voltage. If N_a were smaller, such that V_{tf} would be less than V_a, then there would be no part of the I-V curve where $J \propto V^{\frac{1}{2}}$.

The current is proportional to g in all three regimes because in each regime the free carrier concentrations are controlled by capture kinetics, and don't contribute to space charge. If we have one solution to Eqs. 2.17 through 2.22 for $n(x)$, $p(x)$ and $E(x)$ at a total current density J_1 and generation rate g_1, then the solution at

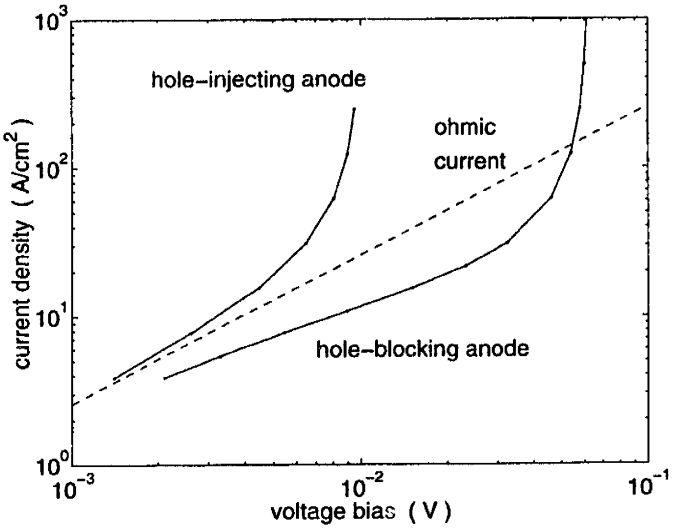

Figure 2-13: I-V curves of the simulated device at $g = 10^{26}$ cm^{-3}s^{-1}, calculated with hole-injecting and hole-blocking boundary conditions at the anode. The ohmic current they both converge to at low bias is shown for comparison. The I-V curve with a hole-blocking anode is the same as the middle curve of Fig. 2-12.

generation rate g_2 and current density $\frac{g_2}{g_1}J_1$ is $\frac{g_2}{g_1}n(x)$, $\frac{g_2}{g_1}p(x)$ and $E(x)$, provided n and p are smaller than N_a and N_d^+ so they don't affect Poisson's equation. The current rises abruptly at V_{tf} because Poisson's equation requires that N_d^+ goes to zero, and n depends on N_d^+ as $n = g/(N_d^+\sigma_n v_t)$ (see Eq. 2.15). At bias voltages greater than V_{tf} (not shown in Fig. 2-12), $n > N_a$, electrons injected from the cathode dominate the space charge, and the current is independent of g. This current is space-charge limited and is proportional to V^2.

Note that the boundary conditions we assume preclude the existence of what is called recombination-limited current [31]. Such current occurs in n-type conductors with a hole-injecting anode and an electron-injecting cathode, and involves the decrease in bias voltage at a given current due to neutralization of space charge by injected holes. At the threshold voltage $V_r = L^2/\mu_h\tau_h$, the I-V curve changes from ohmic to $J \propto V^2$. Recombination-limited current does not occur in our model device, and there is no kink in the I-V curves at $V = V_r$, as shown in Fig. 2-12.

Brown *et al.* [11] measured the I-V curves of an cw-illuminated LTG GaAs photoconductor with a 0.6 μm gap length, and observed a transition from ohmic photocurrent to photocurrent proportional to V^2 at a bias voltage of 5 V. They attributed the

nonlinearity to recombination-limited transport at high bias. We believe their explanation can not be true, mainly because the anode of an LTG GaAs photoconductor doesn't inject holes. However, our assumption about the anode may not be correct, so we calculated the I-V curve of an illuminated LTG device with injecting contacts and with the same parameters listed in Table 2.2, to compare it to the I-V curves in Fig. 2-12 and to Brown's data. The comparison is in Fig. 2-13. The two I-V curves both blow up at finite voltages, though the curve of the injecting-anode device blows up at a lower voltage, because the injected holes neutralize space charge to lower the bias at a given current. Space charge neutralization is similar to dielectric relaxation, thus the threshold voltage of the injecting-anode device depends on the device's bulk conductivity, and generally increases as the parameters τ_e, τ_h, μ_e and μ_h decrease. These parameters do not effect V_{tf}, the threshold voltage of the device with a hole-blocking anode. Note that in neither I-V curve is there a region for which $J \propto V^2$. Such a region only occurs when free carriers make a substantial contribution to the space charge, as discussed above, and in such a region the current is independent of g. Brown's formula for the current, which is quadratic in V and proportional to g, is probably wrong.

The data in [11] show that the current is approximately proportional to illumination intensity, even in the $J \propto V^2$ regime. It's likely that Brown observed a soft breakdown similar to that in either I-V curve of Fig. 2-13, though soft enough for I to be nearly quadratic in V for a small range of voltages. The contact effects discussed in this section may be the cause of breakdown, or there may be a different cause. We will give our explanation of Brown's data when we explain our own data, because we used LTG GaAs from the same source (M. I. T. Lincoln Lab), and our data are very similar to his.

2.2.5 Hot-electron effects in LTG GaAs

Hot-electron effects in LTG GaAs consist of three observed phenomena: velocity saturation, Γ-valley to L-valley transfer and breakdown. Of these three, only velocity saturation and breakdown manifest themselves in the I-V curves of LTG GaAs

conductors. The current in such a device is the sum of the contributions from free electrons with normal mobility and electrons hopping in the donor band with very low mobility (see Sec. 2.2.1). Only the free electrons can gain appreciable energy from the electric field, therefore only they are subject to velocity saturation and they are responsible for breakdown. When hopping conduction dominates the total current of a device, as is the case with a nonilluminated, as-grown LTG GaAs sample at room temperature, its I-V curve is linear right up to an abrupt breakdown due to the free carriers [33, 35, 37]. When the dominance is not as strong, as is the case with a nonilluminated annealed LTG GaAs sample at room temperature, the I-V curve shows a soft breakdown [13, 35, 37, 38]. This is because the high electric field assists the thermal emission of electrons from donor states to the conduction band, which allows the free electron current to overwhelm the hopping current before abrupt, hard breakdown. The hard breakdown is due to a separate mechanism, probably impact ionization, as indicated by the decrease in breakdown voltage with decreasing measurement temperature [35, 38]. When the free electron current is dominant at room temperature and low bias, as is the case with strongly annealed LTG GaAs, then the I-V curve tends to saturate at moderate bias due to velocity saturation. Ibbetson *et al.* reported a saturation velocity of $5\text{x}10^6$ cm/s at a threshold electric field of 3.6 kV/cm [13]. At higher bias the current increases due to soft breakdown and impact ionization.

In any LTG GaAs sample, the free electron concentration increases with increasing temperature, and the above hot-electron effects should become evident. This is demonstrated in Fig. 2-14, which shows the I-V curves of a nonilluminated, planar LTG GaAs conductor over a range of measurement temperatures. At 320 K and below, hopping conduction is dominant. At higher temperature, free electron conduction is dominant and is indeed non-ohmic. We would expect to see a similar set of curves if we varied illumination intensity instead of temperature, because optical and thermal generation of free carriers are similar. Indeed, we will later present data that are similar.

The above qualitative discussion leads us to two important questions about hot

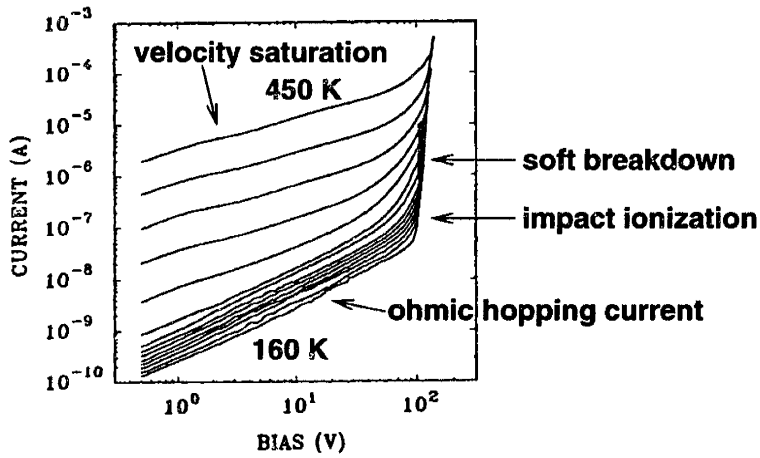

Figure 2-14: I-V curves of a planar LTG GaAs conductor measured at temperatures ranging from 160 K to 450 K. Indicated are the regimes where various conduction mechanisms are dominant. The LTG GaAs was grown at 250 °C, and annealed for 10 minutes at 600 °C. Taken from [35]

electron effects in LTG GaAs: why does the I-V curve show signs of velocity saturation without an unstable regime of Gunn oscillation [3], and why is the breakdown field of LTG GaAs ten times higher than that of GaAs grown at normal temperatures? The first question has not been raised before and the second has been raised but not been answered well.

The answers to both questions probably have to do with the extra scattering in defect-rich LTG GaAs. Arifin *et al.* [39] made a Monte Carlo simulation of electron transport in LTG GaAs, in which they modeled the As precipitates as hard-sphere reflectors that scatter electrons elastically, and the ionized donor and acceptor states as Coulombic scatterers. Their simulation included other scattering mechanisms such as acoustic and optical phonon scattering and intervalley scattering between the Γ, X and L conduction band valleys. The drift velocity that they calculated is plotted as a function of electric field in Fig. 2-15. In (a) the ionized impurity concentration $N_d^+ + N_a^-$ is constant at 10^{17} cm^{-3}, and the As precipitate concentration N_p varies from 0 to 10^{17} cm^{-3}. In (b) N_p is constant at 10^{15} cm^{-3}, and $N_d^+ + N_a^-$ is varied from 10^{17} to 10^{18} cm^{-3}. Both types of scattering centers cause the low-field electron

[3]See Fig. 2 of [32] for an I-V curve of a normal GaAs device with signs of Gunn oscillation

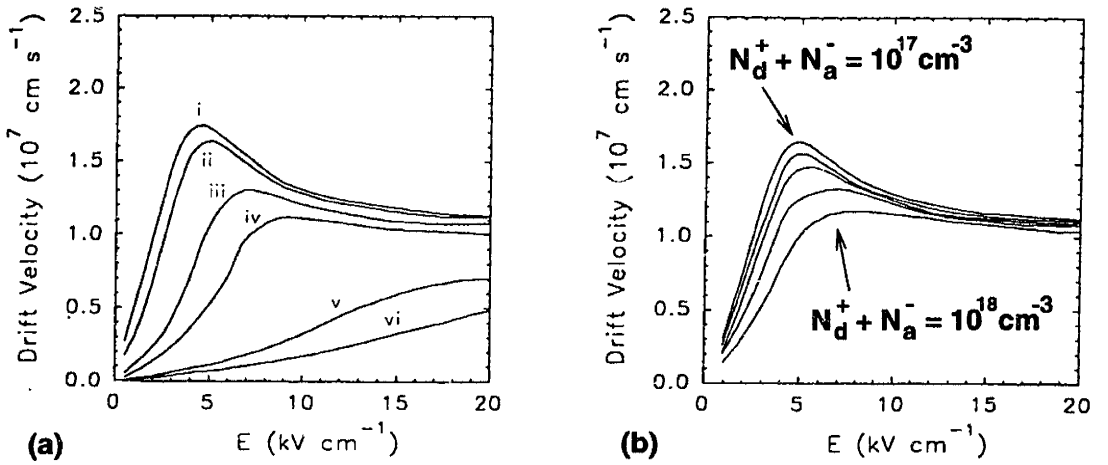

Figure 2-15: Drift velocity in LTG GaAs as a function of electric field for (a) varying As precipitate concentration (N_p) and (b) varying ionized impurity concentration ($N_d^+ + N_a^-$). The values of N_p in (a) are (i) 0, (ii) 10^{15} cm^{-3}, (iii) 5x10^{15} cm^{-3}, (iv) 10^{16} cm^{-3}, (v) 5x10^{16} cm^{-3}, and (vi) 10^{17} cm^{-3}. Taken from [39].

mobility to decrease, though the As precipitates are more effective at doing so. The same change in velocity-field characteristics induced by high concentrations of ionized impurities was observed by Masselink *et al.* [40]. Figure 2-15 shows that if either N_p or $N_d^+ + N_a^-$ is high enough, the region of negative differential mobility is much less pronounced, which suppresses Gunn oscillation. This is in spite of the fact that the same amount of electron transfer to the L-valley takes place in defect-rich LTG GaAs at high fields as takes place in purer LTG GaAs at lower fields (according to Arifin's calculations). The peaking of velocity is suppressed by increased scattering because the low-field electron mobility in the Γ-valley (μ_Γ) is degraded much more by extra scattering than the electron mobility in the L-valley (μ_L). According to Arifin's calculations, the mobility ratio $\frac{\mu_\Gamma}{\mu_L}$ at $N_p = 0$ and $N_d^+ + N_a^- = 10^{17}$ cm^{-3} is 12, while at $N_p = 10^{17}$ cm^{-3} and the same $N_d^+ + N_a^-$, the ratio is only 3. Also, while the peaking of curve (i) in Fig. 2-15(a) is mainly due to intervalley transfer, the saturation of curve (iv) is due more to saturation of the drift velocity of Γ-valley electrons. The acoustic and optical phonon scattering rates in the L-valley must be higher than in the Γ-valley, thus the total scattering rate in the Γ-valley is impacted much more by the presence of extra scatterers.

Arifin *et al.* neglected to consider the effect of LTG GaAs's very short electron capture time on the heating of electrons. The capture time is usually less than 0.5 ps, faster than the energy relaxation time of the Γ-valley, which is about 1 ps [41]. Electron capture may be the dominant inelastic scattering mechanism in LTG GaAs.

While the As precipitate and ionized impurity concentrations considered by Arifin *et al.* are similar to those measured in LTG GaAs, the highest electric field they considered is at least ten times less than the breakdown field of LTG GaAs. Perhaps LTG GaAs has negative differential mobility at very high field, but it's not evident in the I-V curve. Nonuniform field distributions within a device can make the I-V curve increase monotonically, even if the material has negative differential mobility [42]. Such is the case with lightly doped material, in which the depletion region that makes up the Gunn domain is too large to fit within the device. It is also the case with the Fe:InP device of Corvini *et al.* discussed in the last section, for which they calculated a monotonically increasing I-V curve in spite of negative differential mobility [34] (Fig. 2-8 shows their depletion region charge density is $N_d = 10^{15}$ cm^{-3}). But LTG GaAs has a very large density of donors ($N_d \approx 10^{19}$ cm^{-3}), thus the width of Gunn domains would be at the largest $E_{bd}\epsilon/eN_d = 0.02$ μm, where $E_{bd} \approx 3\text{x}10^5$ V/cm is the breakdown field of LTG GaAs. Gunn domains would fit in any of the LTG GaAs devices tested to date, thus the fact that their I-V curves show no instabilities means that LTG GaAs has no negative differential mobility.

Ludwig *et al.* [43] did claim to observe reduced electron velocity in LTG GaAs due to field-induced transfer into the *L*-valley. They made a time-resolved measurement of the transient electric field emitted by a biased, antenna-coupled LTG GaAs photoconductor excited by an optical pulse. The emitted field is proportional to the time derivative of the photogenerated current, thus they could extract information about the time-dependent acceleration and density of photogenerated electrons in the emitter. Their time resolution was limited by the electron capture time τ_e of the LTG GaAs photoconductive receiver (about 1 ps) which sampled the emitted field [44]. The transients they measured at different emitter voltage biases are plotted in Fig. 2-16 (a). Oddly the transients are mostly unipolar, even though a pulse of

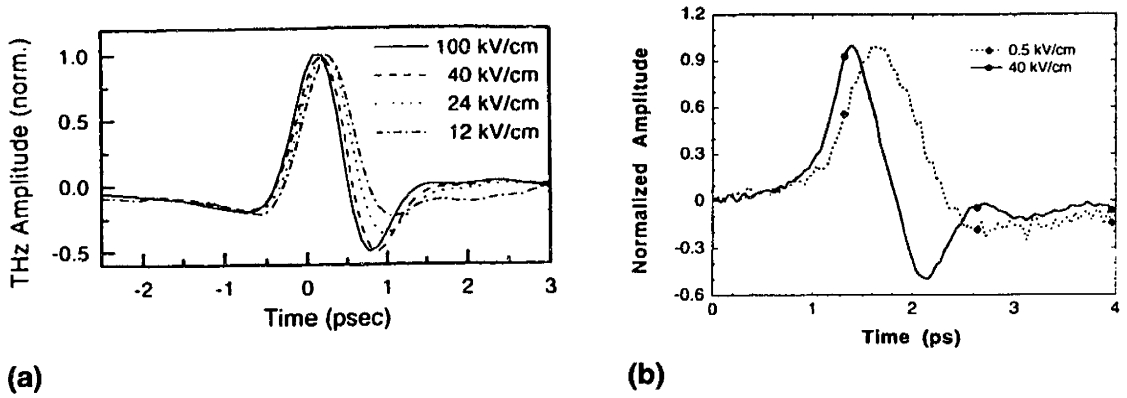

Figure 2-16: Electric field transients as a function of emitter bias field for (a) an LTG GaAs emitter and (b) a normal GaAs emitter. (a) is taken from [43], and (b) is from [45]

photocurrent in LTG GaAs has substantial positive and negative time derivatives. Transients measured by other groups are more bipolar [44]. Ludwig *et al.* ignored carrier recombination and assumed that the transient field is proportional to the electron acceleration at all times. They claimed that the narrowing of the pulse peak and the appearance of a negative peak at high bias is due to velocity overshoot, followed by intervalley transfer and deceleration of carriers in the L-valley, as observed by Son *et al.* in normal GaAs with the same technique [45] (see Fig. 2-16 (b)). The trend Ludwig *et al.* observed does agree with their theory, yet if we consider the effect of carrier recombination on the emitted field, then we predict an antisymmetric bipolar transient at low bias, and a bipolar transient with a more pronounced negative peak at high bias due to velocity overshoot. Since a model including carrier recombination doesn't fit the data, it seems that the emitter's τ_e is substantially greater than the receiver's, which may be due to the strong bias on the emitter (the bias dependence of τ_e will be discussed in Sec. 2.6).

The similarity between the transients in Fig. 2-16 (a) and (b), for LTG GaAs and normal GaAs at the same bias field of 40 kV/cm, is striking. Why doesn't the extra scattering in LTG GaAs curtail velocity overshoot? It may be that velocity overshoot takes place in LTG GaAs, but at lower velocities than in normal GaAs, because of some other scattering mechanism with an energy threshold besides intervalley scattering, for example optical phonon scattering. To check this, one would

have to compare the total output power of a LTG GaAs emitter and a normal GaAs emitter of the same size, at the same bias and optical excitation. If the output of the LTG GaAs emitter were lower, it would mean velocity overshoot was taking place at a lower velocity. The data in [43] and [45] don't allow this comparison.

Ludwig *et al.* state that 40 kV/cm is a high enough electric field for electrons in LTG GaAs to transfer ballistically to the L-valley. With an electric field of 40 kV/cm, it takes 125 fs for an electron to acquire 200 meV (assuming the effective mass is that of the GaAs Γ-valley), which is the energy an electron generated by a 816-nm-wavelength photon needs to reach the L-valley [43]. The momentum relaxation time τ_m in LTG GaAs is about 19 fs, assuming $\tau_m = \mu_e m^*/e$ and $\mu_e = 500$ cm^2/Vs, which is almost an order of magnitude less than 125 fs, making ballistic transfer to the L-valley very unlikely.

Luo *et al.* observed that the breakdown electric field E_{bd} of LTG GaAs has a strong dependence on the growth temperature [35]. LTG GaAs grown at 200 °C has an E_{bd} of 300 kV/cm, while GaAs grown at 375 °C has an E_{bd} of 20 kV/cm. Annealing does not change E_{bd} appreciably [37]. It's tempting to say that the extra scattering and low τ_e of LTG GaAs postpones impact ionization to higher electric fields than in normal GaAs, but the low-field mobility [21] and τ_e [17, 27] of LTG GaAs are both known to increase with annealing, without a corresponding decrease in E_{bd}. However, as discussed in Section 2.2.2, holes are captured more efficiently after anneal than before, perhaps because of capture by As precipitates. E_{bd} would stay relatively constant with annealing if band-to-band impact ionization by holes is significant, as it is in normal GaAs [36]. The holes in LTG GaAs have been relatively ignored, but impact ionization may be one phenomenon in which they play a crucial role.

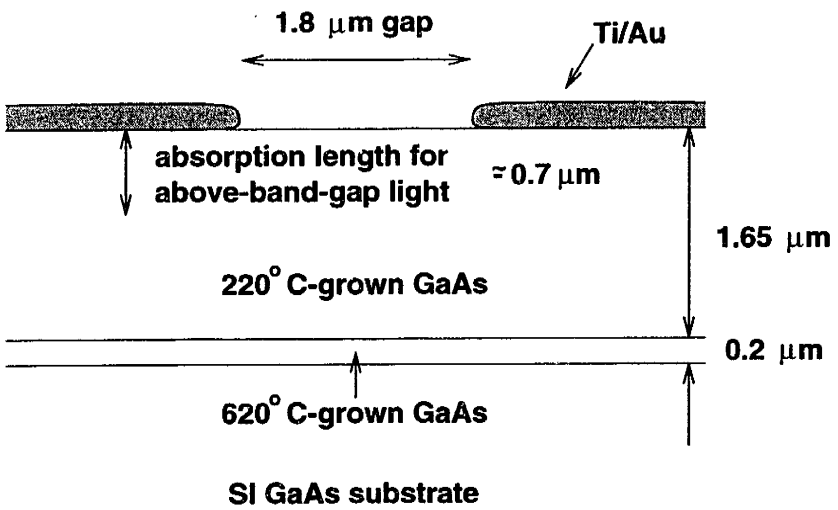

Figure 2-17: Cross section of the experimental device, drawn to scale, showing the two epitaxial layers of GaAs and the metalization.

2.3 The experimental device

The experimental device was grown and fabricated at M. I. T. Lincoln Laboratory. The LTG GaAs was grown in an Intevac modular Gen II MBE system on an LEC-grown SI GaAs substrate. The substrate was not bonded to the holder; measurements suggest this causes the substrate to be $15-20\,^{\circ}\mathrm{C}$ cooler than the thermocouple on the holder [27]. GaAs was grown at a rate of 1 μm/h, using Ga and As_4 fluxes, at a beam equivalent pressure ratio of 11. First, 0.2 μm of GaAs was grown at a normal growth temperature of $620\,^{\circ}\mathrm{C}$. Then 1.65 μm of LTG GaAs was grown at $220\,^{\circ}\mathrm{C}$. Finally, the sample was annealed *in situ* for 10 minutes at $580\,^{\circ}\mathrm{C}$ under As overpressure. The device's cross section, showing the two epitaxial layers, is shown in Fig. 2-17.

We did not fabricate an anti-reflection coating above the LTG GaAs, so a portion of the light incident on the LTG GaAs surface is reflected due to the dielectric mismatch between GaAs and air. The refractive index n of GaAs is 3.6 [36], so $4n/(1+n)^2 = 68\%$ of the incident power is transmitted [46]. The absorption coefficient of LTG GaAs at the above-band-gap laser wavelengths we use (770 – 790 nm) is approximately $1.5\text{x}10^4$ cm^{-1} [47, 48], therefore 92% of the transmitted light is absorbed in the LTG GaAs layer. The absorption length is shown in comparison to the thickness of the epitaxial layers in Fig. 2-17.

The experimental devices are photoconductors embedded in coplanar waveguide-type transmission lines. The device layout is shown in Fig. 2-18. The single-level metalization was defined on the LTG GaAs surface layer by electron-beam lithography, and fabricated by liftoff of 20 nm of titanium and 200 nm of gold. A coplanar waveguide (CPW) consists of a planar strip centered between two semi-infinite ground planes. Our center strip is 4.1 μm wide, and is separated from the ground planes by 2.95 μm. The photoconductor is simply a 1.8-μm-wide gap in the center strip. The ground planes are only 50 μm wide, but are separated by only 10 μm, so they are effectively semi-infinite.

The photoconductor is embedded in a CPW so that time-dependent photocurrents with a bandwidth near 1 THz couple to one of the CPW's quasi-transverse-electromagnetic (TEM) propagating modes, and are collected at the terminations of the CPW without radiating away. CPWs contain three separate pieces of metal and therefore allow two quasi-transverse-electromagnetic (TEM) propagating modes. The modes are called even and odd according to the symmetry of each mode's electric field with respect to the CPW's center conductor.

Figure 2-19 shows how transient current in the photoconductor generates only the odd propagating mode, since only that mode has a net current in its center conductor. The even mode is shown for comparison (See Chapter 3 for more discussion of this topic). The largest dimension of our CPW is the 10 μm between the ground planes. The group velocity v_g of the quasi-TEM modes of coplanar transmission lines on a semi-infinite GaAs substrate is $1.1\text{x}10^8$ m/s [49], therefore the cutoff frequencies of higher-order and radiating modes are at least $v_g/10$ μm = 11 THz, and transient photocurrents with a bandwidth less than that should couple purely to the odd mode. With the dimensions stated above, the odd mode of our CPW has a characteristic impedance $Z_0 = 50\ \Omega$ [49]. The CPW's full length of .73 mm corresponds to a round-trip travel time from the photoconductor to the end of the CPW and back of .73 mm/v_g = 6.6 ps. The influence of these values on pulsed-illumination experiments will be discussed later.

The 3" wafer holding many devices was diced and individual chips with four

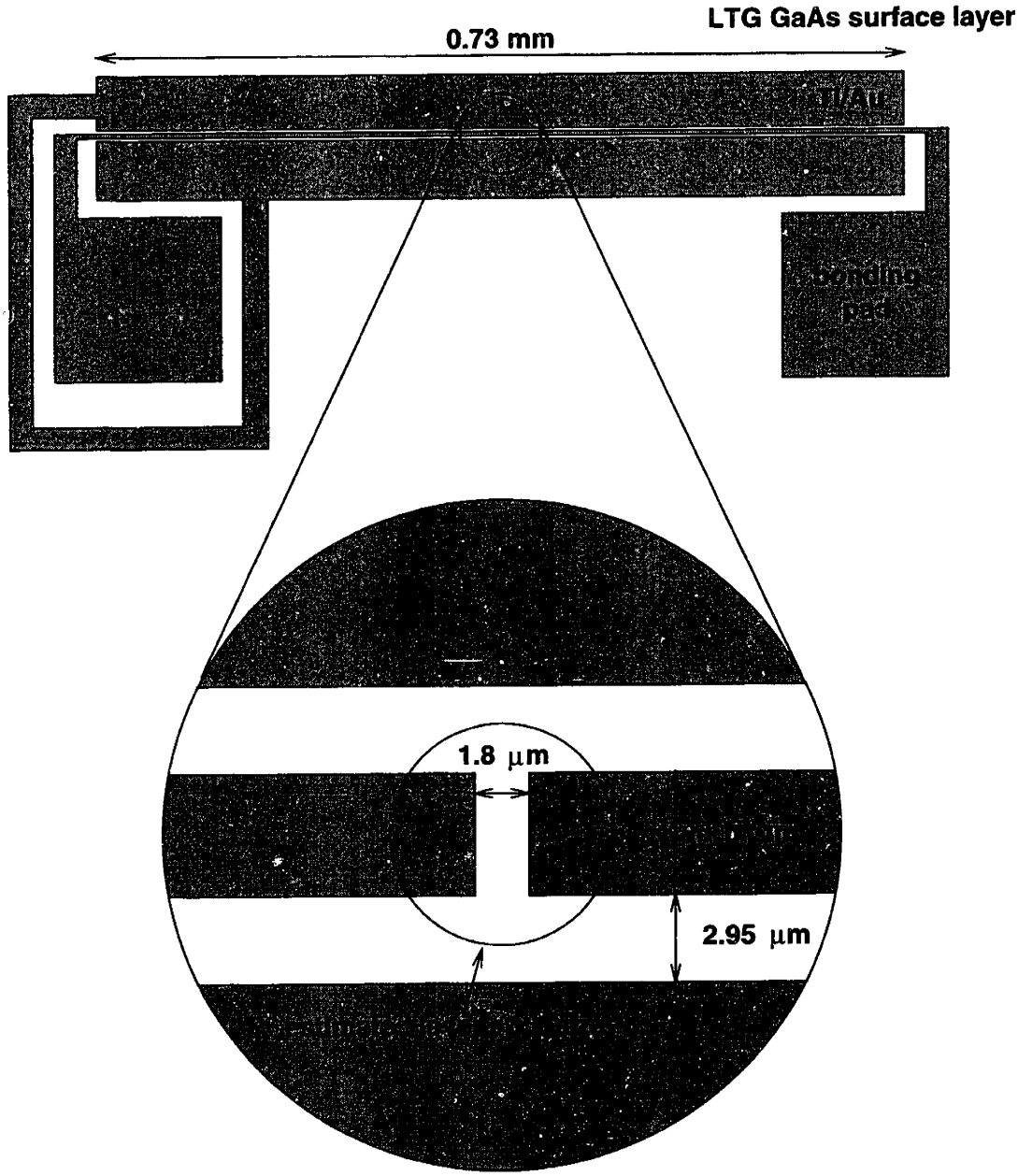

Figure 2-18: Plan view of device, drawn to scale, showing a photoconductor embedded in a coplanar waveguide. The inset shows the photoconductor's active region.

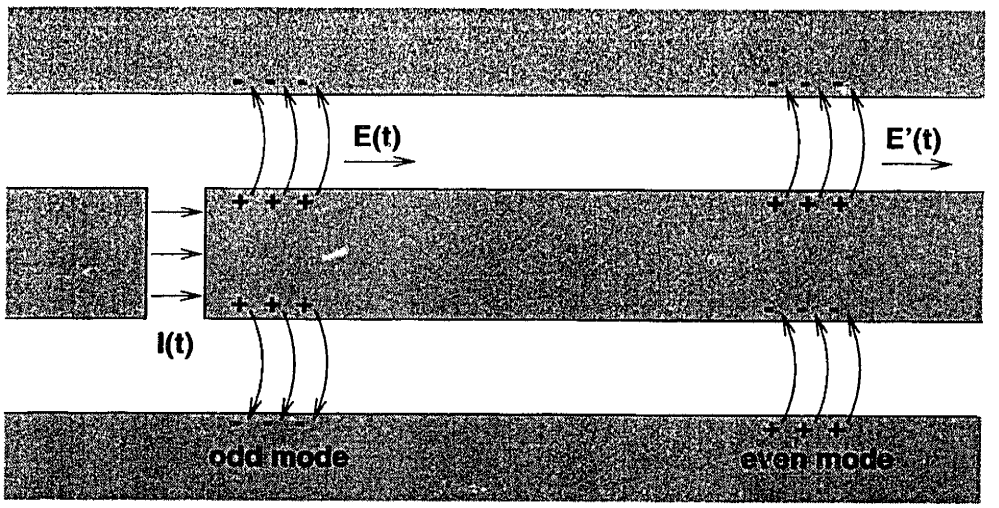

Figure 2-19: Left: transient photocurrent $I(t)$ generating the odd propagating mode $E(t)$ of a coplanar waveguide. Right: the even propagating mode $E'(t)$ shown for comparison.

devices each were mounted in chip carriers. Two wire bonds were made to each device, to the two bonding pads shown in Fig. 2-18. These pads contact the anode and cathode of the photoconductor via the center conductor of the CPW. The ground planes don't require a bias and were left floating.

2.3.1 Two-dimensional device models

Our planar LTG GaAs photoconductor is two-dimensional in nature, which makes analysis of current transport within the device difficult. We would like to be able to treat it as a resistor: at a given voltage bias and intensity of uniform illumination, we would like single values for all carrier concentrations, filled defect concentrations and the electric field. To consider the device uniform, the electron injection region near the cathode and the hole depletion region near the anode must not extend over a significant portion of the device. In Section 2.2.4, we derived threshold bias voltages for the intrusion of contact effects. With the physical parameters listed in Table 2.2 and a device length $L = 1.8$ μm, the threshold voltage for significant hole depletion at the anode is $V_a = 1.4$ kV and the trap filling voltage is $V_{tf} = 22$ kV. The lowest threshold voltage, V_a, is almost 30 times greater than the highest bias we applied

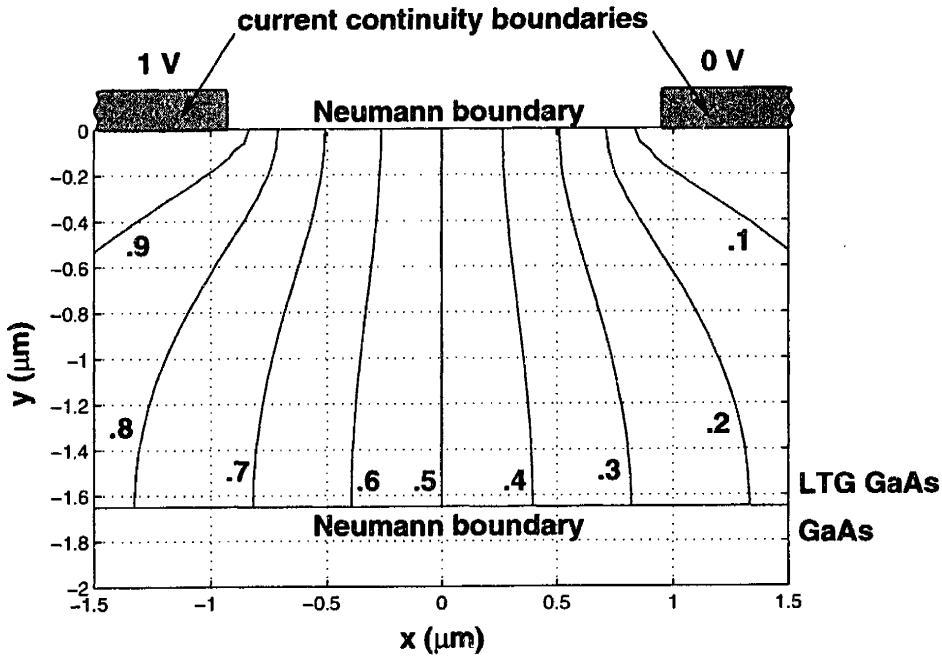

Figure 2-20: Contour plot of the electric potential in the nonilluminated experimental photoconductor under a 1 V bias, as solved with Matlab assuming charge neutrality. The types of boundary conditions are shown at their respective boundaries. The actual simulation region extended to $x = \pm 15$ μm.

(50 V), therefore we can consider our device's bulk uniform and charge neutral.

To see how geometric effects such as current spreading cause nonuniformity in our device, we simulate our device and solve the current continuity equation and Poisson's equation in two dimensions. This is different from the approach of Brown [50], who neglected current continuity and assumed charge neutrality throughout the substrate. First we consider a nonilluminated device shown in Fig. 2-20. In this case, the entire LTG GaAs layer can be considered a region of uniform, ohmic conductivity, because both hopping conduction and drift of thermally generated free electrons is ohmic. Later we will show that hopping conduction dominates the dark current in the experimental device. The current density J is then proportional to the electric field E, so we will satisfy current continuity within the bulk by solving Poisson's equation to find E. The equation to solve is then $\nabla^2 V = 0$, where V is the electric potential,

$E = -\nabla V$ and $J = \sigma E$, where σ is the conductivity.

The boundary conditions all derive from current continuity, not electrostatics. The air-LTG GaAs interface between the contacts must reflect current, therefore the condition at that boundary is $E_\perp = 0$, which is a Neumann boundary condition. Hopping conduction does not occur in the normal GaAs beneath the LTG GaAs layer, thus the conductivity of the normal GaAs is much lower than that of the LTG GaAs, and the LTG GaAs-GaAs interface is also a reflecting Neumann boundary. It's tempting to describe the metal contact-LTG GaAs boundaries as equipotentials, but that would ignore the finite contact resistance. We must set current in the bulk flowing away from the contact, $\sigma E_\perp$, equal to the current flowing through the interface, $(V_{\text{bias}} - V)/\rho_c$, where ρ_c is the specific contact resistivity. V is the potential on the bulk side of the contact, which may be different from V_{bias}, the potential in the metal. The product $\sigma\rho_c$ has the units of length, and represents the characteristic length over which V varies near the contacts. The data we will present later indicate that the contact resistance in the experimental device is negligible, therefore we have taken $\sigma\rho_c = .01$ μm, which is much smaller than the characteristic lengths of the device. In this limit the contact is essentially an equipotential. The contacts of the experimental device extend very far away from the device's active region, so we extended the limits of the simulation to $x = \pm 15$ μm, far enough away for the lateral boundaries to be irrelevant.

The electrical potential calculated by Matlab and based on the above equations is shown in Fig. 2-20. Note that the electric field at $x = 0$ is nearly constant with depth and that current is collected at the contacts over a length much greater than $\sigma\rho_c$. The electric field at $x = 0$ and $y = 0$ is $\frac{2V_{\text{bias}}}{3l}$, where l is the device length. We integrate J along the line $x = 0$ to find the total current per unit width $I = .63\frac{\sigma V_{\text{bias}} t}{l}$, where t is the LTG GaAs layer thickness. This is not much less than the current that would obtain if the contacts were not planar but instead extended down to the bottom of the LTG GaAs layer, making the electric field uniform and the current $I = \frac{\sigma V_{\text{bias}} t}{l}$. We can treat our device as a uniform resistor with uniform field $E = \frac{V_{\text{bias}}}{l}$, as long we decrease the expected current by 63%.

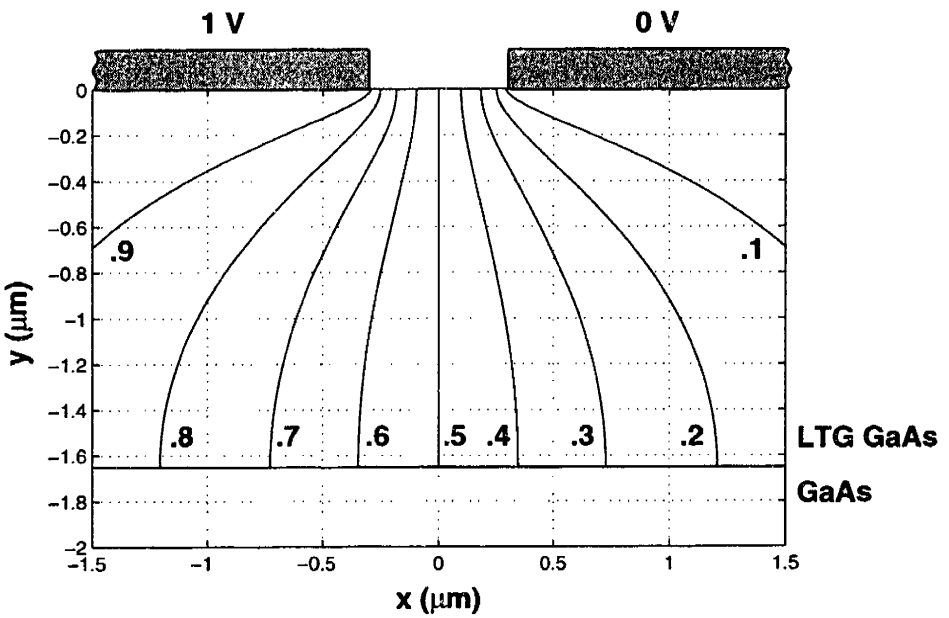

Figure 2-21: Contour plot of the electric potential in a .6-μm long photoconductor under a 1 V bias, as simulated equivalently to the device shown in Fig. 2-20

Two-dimensional simulation becomes important when the photoconductor gap length is much less than the width of the LTG GaAs layer. The potential contours for such a case are shown in Fig. 2-21, in which the gap length is .6 μm. The electric field is now much greater near the device's surface than at the bottom of the LTG GaAs layer. As the gap length approaches zero, the device resistance will not approach zero, but will instead approach a constant value dependent on the thickness of the LTG GaAs layer. We have measured the resistance of nonilluminated devices with different gap lengths, and we discuss the data the next section.

The two-dimensional calculation of E and J are more complicated for an illuminated device because the nonuniform free carrier concentration excited by light leads to a nonuniform σ. The boundary conditions remain the same, but the equations to be solved in the bulk become $E = -\nabla V$ and $\nabla \cdot (\sigma(x,y)E) = 0$. The space-dependent conductivity $\sigma(x,y)$ is approximately $\sigma_p \exp(-\alpha y) + \sigma_0$ in the illuminated

region between the contacts and $\sigma(x, y) = \sigma_0$ elsewhere, where σ_p is the light-induced conductivity at $y = 0$, α is the optical attenuation coefficient and σ_0 is the conductivity of dark LTG GaAs. It may be very important to model the diffraction of light and the diffusion of free carriers towards the dark regions under the contacts, because these regions are effectively in series with the illuminated bulk, and may reduce the total current due to their low conductance. We expect little diffusion or diffraction in the experimental device, because the electron diffusion length in LTG GaAs is very small (for $\mu_e = 200$ cm^2/Vs and $\tau_e = .2$ ps, $L_d = \sqrt{\mu_e kT\tau_e/q} = .01$ μm), and the gap length is much larger than the wavelength of light in GaAs (1.8 μm and .22 μm, respectively).

The above mentioned nonuniformities make it too difficult for us to simulate the current in a two-dimensional illuminated device. The calculation could be done with device simulation software such as Atlas [51], from Silvaco, which incorporates the non-uniform generation of free carriers by light incident on a device surface. It would be interesting to compare such simulation with measurements of an illuminated TLM-type structure on LTG GaAs, with which one could distinguish near-contact and bulk effects. For the remainder of this thesis we will consider an illuminated device to be a uniform resistor with a thickness equal to the optical absorption length.

2.4 Dark measurements

We measured the I-V curves of the experimental device in the dark at different temperatures to characterize the LTG GaAs. The curves are shown in Fig. 2-22. The noise in the current at high temperature and low bias is due the thermocouple on the wafer holder. The curves are very linear, with slight positive curvature, up to applied electric fields as high as $E = 50$ V/1.8 μm = 2.8x10^5 V/cm, just under the breakdown field of normal GaAs, which is 4x10^5 V/cm [36]. We fit the low-bias portion of the I-V curves to a line to find the device resistance at each temperature. We made a similar fit to find the resistance of a device with a shorter gap at 24 °C. The plot of normalized resistance (resistance times device width) as a function of gap length at

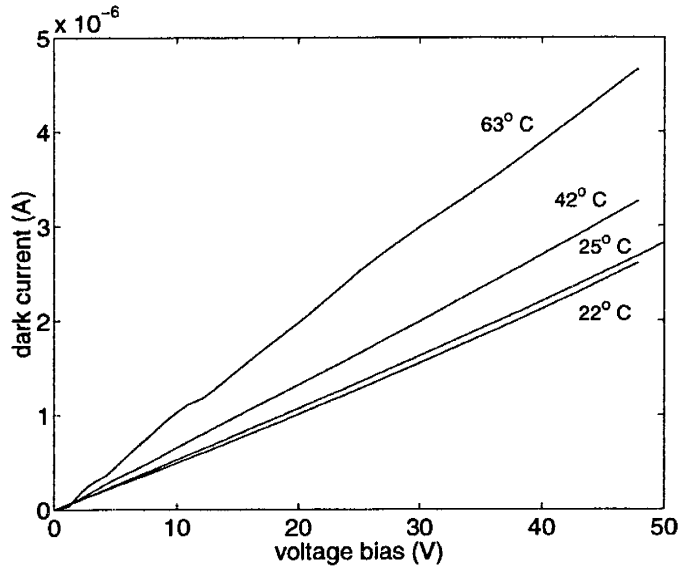

Figure 2-22: Dark current vs. voltage bias at different temperatures

24 °C is shown in Fig. 2-23. Surprisingly, the resistance approaches zero as the gap length decreases, even though the shortest gap length, 0.56 μm, is much less than the thickness of the conductive LTG GaAs layer. As discussed in the previous section, the resistance should approach a constant value because of the finite thickness of the LTG GaAs, aside from any contact resistance at the metal-LTG GaAs interface. This indicates that most of the current flows in the top 0.5 μm of the LTG GaAs. A previous study [52] found defect clustering to occur at the bottom of an LTG GaAs layer, therefore our high current near the surface of LTG GaAs is probably a surface effect. We fit a line to the data of Fig. 2-23 to extract the normalized contact resistance r_c and specific contact resistivity ρ_c [53] of the metal-LTG GaAs contact, which are 23 Ω cm and 6x10^{-6} Ω cm^2, respectively. This fit gives the characteristics of the metal-LTG GaAs contact and not the spreading resistance due to the finite LTG GaAs thickness because only the contact resistance causes the voltage between the tips of the contacts to be less than the applied voltage: contact resistance is in series with the bulk, spreading resistance is in parallel.

We did not collect enough data to measure r_c and ρ_c with great accuracy. Their values can be anything from 0 to upper bounds of about 300 Ω cm and 10^{-3} Ω cm^2, respectively. The value of ρ_c is comparable to but lower than 1.5x10^{-3} Ω cm^2, the

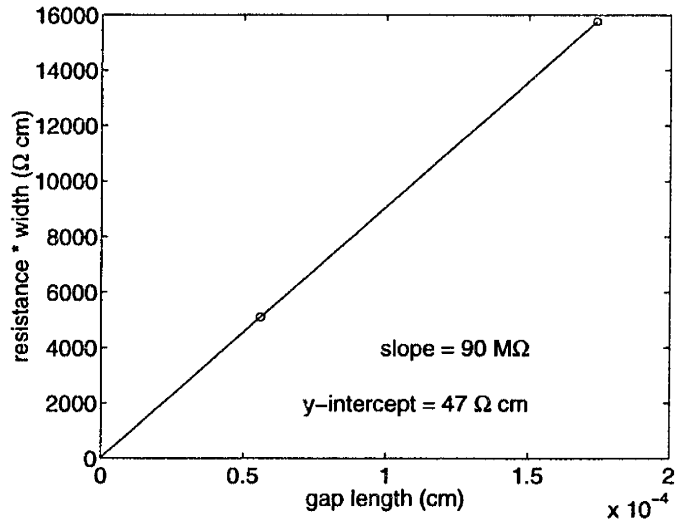

Figure 2-23: Dark resistance normalized by device width vs. device length at 24 °C. A line is drawn through the two data points and extended to the y-axis.

value measured by Yamamoto *et al.* [29]. In Section 2.2.3 we discussed Yamamoto's measurement of metal-to-as-grown LTG GaAs contacts, and wrote that we would expect higher ρ_c for contacts to annealed LTG GaAs because of the lower hopping conductivity. It may be that tunneling is more of a factor in our devices, or that the interface barrier height may be lower than in Yamamoto's devices. Experiments with TLM structures on annealed LTG GaAs would yield more accurate data than ours, and help to resolve this issue. Fig. 2-23 clearly shows that we may neglect the contact resistance of the devices with 1.8-μm-long gaps.

We derived the conductivity σ of the LTG GaAs layer as a function of temperature from the resistances extracted from the data of Fig. 2-22. We used the following formula: $\sigma = \frac{l}{Rwt}$, where R is the resistance, l is the photoconductor's gap length, w is the gap width and $t = 0.5$ μm is the approximate thickness of the conductive region at the surface of the LTG GaAs layer. The derived conductivities are all near 10^{-4} $\Omega^{-1}\text{cm}^{-1}$, which is three orders of magnitude higher than the conductivity of SI GaAs [54]. Thus our assumption that the primary conduction path is through the LTG GaAs layer is correct.

An Arrhenius plot of the conductivity as a function of temperature is shown in Fig. 2-24. The data are fit much better with an activation energy E_a of .14 eV than

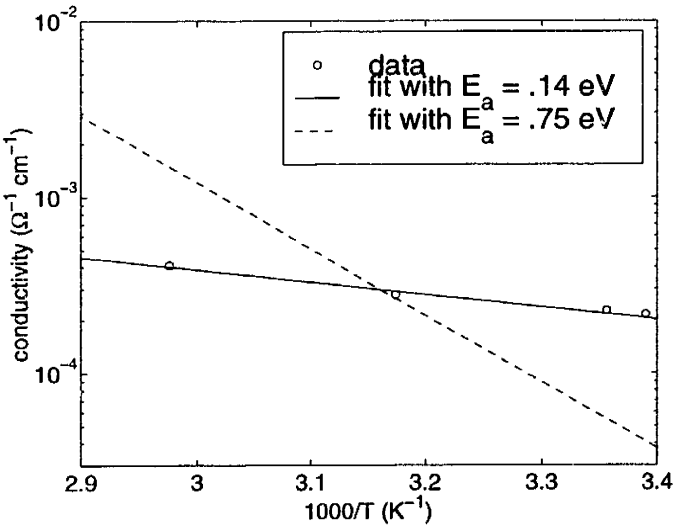

Figure 2-24: Dark conductivity vs. temperature

.75 eV. This low E_a is indicative of hopping conduction; conduction by free electrons in LTG GaAs has an E_a of .75 eV, as discussed in Section 2.2.1. Luo *et al.* [35] measured an E_a of about .08 eV for hopping conduction in annealed LTG GaAs. Our value of E_a is closer to the value Smith measured for as-grown material, .17 eV, than to the value he measured for annealed material, .04 eV, even though the conductivity of his as-grown material is ten times the conductivity of our annealed LTG GaAs. The activation energy of hopping conduction is related to the width of the donor band, which tends to decrease with annealing as the donor concentration reduces. Our measured conductivity at the highest temperature may be boosted by thermally-generated free electrons, which would exaggerate our extracted E_a.

The conductivity data are very similar to what Smith measured for LTG GaAs grown at 200 °C and annealed at 400 °C, and to what Look *et al.* measured for T_g = 200 °C and T_a = 500 °C [16, 21]. The similarity of our conductivity to that of Look's (as well as similar measurements of free electron mobility, as discussed below), allows us to tentatively assume that the point defect concentrations in our LTG GaAs are the same as in his. Those concentrations are $N_D = 2\text{x}10^{19}$ cm^{-3} and $N_A = 10^{19}$ cm^{-3}, as shown in Fig. 5 of [21]. This value of N_a is the same that we assumed in Sec. 2.2.4 (see Table 2.2), where we used it to calculate the threshold voltages for contact effects. Only the trap-filling voltage is applicable is applicable to a device

dominated by hopping conduction, since conduction by free holes is negligible. With a device length $L = 1.8$ μm, the trap-filling voltage is $V_{tf} = 22$ kV, which is far above the bias voltages we applied. This is consistent with the fact that we observe only ohmic dark current.

2.5 Continuous-illumination measurements

We further characterized the experimental device by studying its response to uniform, continuous illumination. A continuous-wave (cw) beam from a Ti:sapphire laser was shined through a 10x microscope objective with a 14.8 mm focal length on to the sample at normal incidence. The laser wavelength λ was tuned to 789 nm, which corresponds to a photon energy of 1.57 eV, 150 meV above the bandgap of GaAs at room temperature [36]. The beam diameter d_0 was 2 mm, as estimated by eye by shining the beam on a ruler. From Gaussian beam theory, the minimum diameter of a focused beam is $4\lambda f/\pi d_0$ [55], where f is the focal length of the focusing lens. The minimum diameter of our focused beam was therefore approximately 7.4 μm. As shown in Fig. 2-18, the focused beam was slightly larger than the active region of the photoconductor. Though the focused beam had a gaussian spatial profile, we will assume that the optical power was uniform distributed throughout the 7.4-μm-diameter focal spot. The sample was mounted on an x-y-z translation stage, and we aligned the sample to the laser beam by finding the x, y and z position of greatest photocurrent. Fine alignment of the laser spot to the photoconductor was accomplished by steering the laser beam. The photocurrent was very sensitive to all three positioning axes, thus we are confident the sample was illuminated as shown in Fig. 2-18. To vary the optical power incident on the sample, we rotated a circular variable attenuator through which the laser beam passed.

To study the illuminated device, we measured its I-V curve at three different optical powers. We measured the dark current as well and subtracted it from the pumped current to obtain the photocurrent I-V curves. Those curves are shown in Fig. 2-25, along with the dark current I-V curve for comparison. The photocurrent

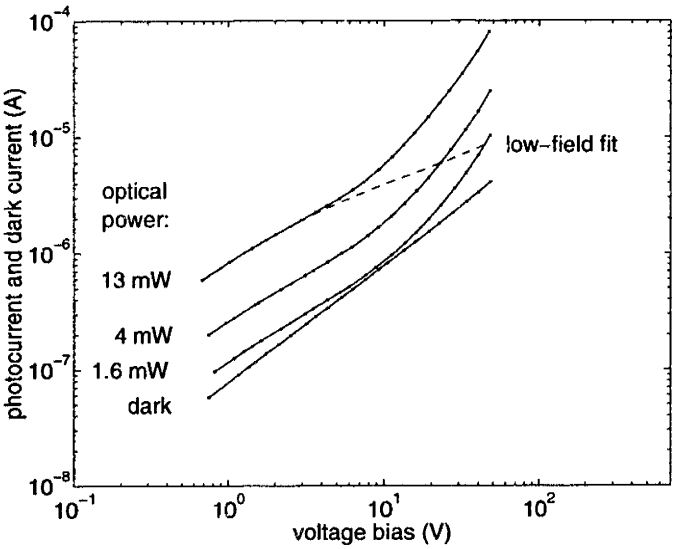

Figure 2-25: Photocurrent and dark current vs. voltage bias

I-V curves are all similar in shape and are very different in shape from the dark I-V. The difference is even more pronounced in Fig. 2-26, in which we plot the normalized differential conductance ($\frac{d\log(I)}{d\log(V)}$) of both the photocurrent and dark current vs. voltage bias. The dark current is nearly ohmic ($\frac{d\log(I)}{d\log(V)} = 1$) over the entire bias range, yet the photocurrent shows signs of saturation ($\frac{d\log(I)}{d\log(V)} < 1$ and decreasing) at low bias and superlinearity ($\frac{d\log(I)}{d\log(V)} > 1$) at high bias.

The dark current and the photocurrent have such different characteristics for two reasons. First, photocurrent is carried by free carriers, while hopping current is carried by electrons in the donor band. Second, the photogenerated electron concentration is determined by capture and recombination dynamics, while the concentration of filled donors is determined by charge balance with ionized acceptors. Conduction band electrons have a much higher mobility than electrons in the donor band, and are therefore subject to hot electron effects such as velocity saturation and impact ionization. Holes may make a significant contribution to the photocurrent, therefore the anode boundary condition, $J_h = 0$, may cause the photocurrent I-V curve to roll off. Velocity saturation and hole depletion at the anode may explain the sublinear region of the pumped I-V, and impact ionization can perhaps explain its superlinear region.

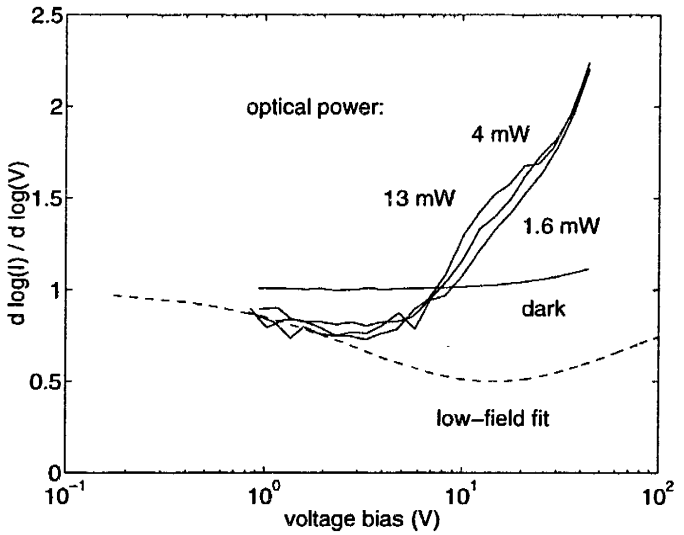

Figure 2-26: Normalized differential conductance of photocurrent and dark current vs. voltage bias

Of the two mechanisms that can cause sublinearity, only electron velocity saturation produces a model that fits the data well. A model based on hole depletion requires a threshold voltage $V_a = 5.7$ V to match the roll-off in the data. If we assume $N_a = 10^{19}$ cm^{-3}, then the product $\tau_h \mu_h$ must be 1.28x10^{-10} cm^2/V to match V_a. Not only is this product about 15 times the value of the product of the expected parameters in Table 2.2, it leads to a predicted value of the low-bias hole current that is 3.3 times greater than the measured total current. It is unlikely that there is an optical coupling loss large enough to account for this difference. The product is also large enough to make the hole current larger than electron current. However, Stellmacher *et al.* observed the Hall effect in illuminated LTG GaAs and concluded electrons are the dominant photogenerated carrier [22].

We show a fit to the I-V curve at the highest illumination intensity with a model based on electron velocity saturation in Figs. 2-25 and 2-26. We assume the following velocity-field relationship for photogenerated electrons:

$$v_e(E) = \frac{v_{\text{sat}}}{1 + \frac{v_{\text{sat}}}{\mu_e E}}, \tag{2.24}$$

where v_e is the electron drift velocity, μ_e is the low-field electron mobility, v_{sat} is the

Table 2.3: Parameters used to fit the data of Fig. 2-25.

quantity	measured value	units
τ_e	200	fs

quantity	assumed value	units
τ_h	830	fs

quantity	value extracted from fit to data	units
μ_e	164	cm^2/Vs
μ_h	5	cm^2/Vs
v_{sat}	$4.4x10^6$	cm/s

high-field saturation velocity, and E is the average electric filed in the device, assumed to be V/L. As discussed in Sec. 2.2.5, negative differential mobility has never been observed in LTG GaAs. We assume the hole velocity doesn't saturate for the electric fields of interest, so the hole velocity v_h is simply $\mu_h E$. We assume the electron and hole concentrations n and p are $g\tau_e$ and $g\tau_h$, respectively, where τ_e and τ_h are the respective capture times. We obtain g from the illumination power P by assuming the focal spot size is as described earlier, and assuming that carriers are generated uniformly within one extinction length of the LTG GaAs surface. In addition to a loss due to reflection at the air-LTG GaAs interface, we assume a 10% loss due to the microscope objective used for focusing. The formula for the photocurrent is then:

$$I = g(P)(\frac{\tau_e v_{sat}}{1+\frac{v_{sat}}{\mu_e E}} + \tau_h \mu_h E) w \delta, \tag{2.25}$$

where w is the device width and δ is the optical extinction length. Eq. 2.25 has only three degrees of freedom, so we must measure or assume values for two parameters independently. The electron capture time was found to be 200 fs by measuring the transient reflectance of the LTG GaAs layer before metalization. We assume that τ_h is 830 fs, as assumed in Sec. 2.2.4. The parameters extracted from a fit to the data of Fig. 2-25 are in the third part of Table 2.5. The values of μ_e, μ_h and v_{sat} are very low compared with the values of these quantities for normal GaAs, but that that is to be expected for material with defect concentrations near 10^{19} cm^{-3}, as discussed

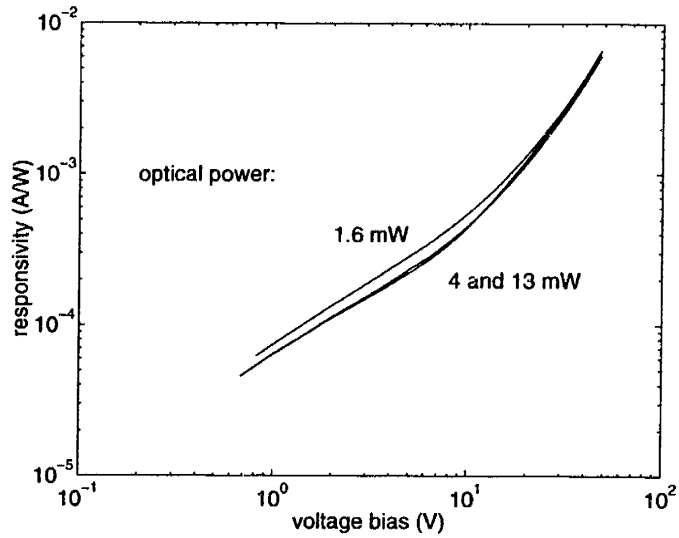

Figure 2-27: Responsivity vs. voltage bias

in Sec. 2.2.5. The value of μ_h can not be extracted with great accuracy, because electrons dominate the photocurrent in the bias voltage range of the fit.

The functional dependence of the photocurrent on the illumination intensity tells us something about the recombination dynamics in our device. The responsivity, which is the photocurrent divided by the optical input power, is plotted as a function of voltage bias in Fig. 2-27. Note that all three curves nearly overlap, especially at high bias. The low-illumination I-V curve would perfectly overlap the other two curves if we subtracted a small ohmic current from it, a current similar to the dark current. It may be that the generation of free carriers causes a rearrangement of charge in the various defects that alters the hopping conductivity. This change is less noticeable when photoconductivity is more dominant. Since the electron capture time at a given voltage bias is nearly intensity-independent, and we observe no saturation of the responsivity, we can conclude that the defect densities are much greater than the densities of the photogenerated carriers. This is to be expected, because with the parameters of Table 2.5, we calculate steady-state values for n and p of $2.2\text{x}10^{14}$ cm^{-3} and $8.9\text{x}10^{14}$ cm^{-3}, respectively, at the highest illumination intensity, which are orders of magnitude less than the values of donor and acceptor concentrations measured by others. Even at a bias of 45 V, where the free carrier concentrations

must be about ten times higher than their low-field values to account for the high current, the free carrier concentrations are still smaller than the defect densities.

Now we consider explanations for the superlinear I-V curve at high bias. Trap filling would cause the observed increase in current if V_{tf} were about 50 V. For a device length of 1.8 μm, N_a would have to be 2.2x10^{16} cm^{-3}. As discussed earlier, we are expecting a value closer to 10^{19} cm^{-3}. Liu *et al.* [20] measured a value of 4x10^{17} cm^{-3} for LTG GaAs grown at 200 °C and annealed at 580 °C, but even this low value is 18 times greater than the value we require. Also, if the superlinearity were due to trap filling, then V_{tf} would be proportional to the square of the device length. We have measured the I-V curves of illuminated devices of different lengths and found that the voltages where superlinearity occurs scale approximately sublinearly with length. Thus we rule out trap filling as the cause of superlinearity.

As shown in Fig. 2-13, superlinear I-V curves occur at lower voltages in devices with hole-injecting anodes than in devices with hole-blocking anodes. Though we stated that a metal-on-LTG GaAs contact is not hole-injecting, we must see if superlinearity due to hole injection can explain our data anyway. To fit the high-bias data while maintaining the fit of the low-bias data, we can change the values of N_a and N_d while keeping the products $N_a\sigma_n$ and $(N_d - N_a)\sigma_p$ constant to keep τ_e and τ_h constant (see Eqs. 2.15 and 2.16). Changing μ_e and μ_h would change the bias voltages at which superlinearity occurs, but it would also change the low-bias current, so we can't alter them. Once again, we can only match the high-bias data by bringing the value of N_a down to an unacceptably low level (about 5x10^{16} cm^{-3}). Like trap filling, hole injection causes superlinearity at bias voltages that scale with the square of device length. This is not what we observe, thus we rule out hole injection as the cause of superlinearity.

There are a number of electric-field activated phenomena that may explain the superlinear part of the I-V curve. Impact ionization, intervalley transfer and field-induced reduction of the capture cross sections are some examples. Impact ionization appears as an extra field-dependent generation term in the carrier continuity equations (see Eqs. 2.19 through 2.21), and the last two mechanisms make the capture cross

sections σ_n and σ_p, and thereby τ_e and τ_h, field-dependent. We can see which type of mechanism is the likely cause of the observed superlinearity by investigating the field-activated terms that, when added to our low-field model, match the predicted current to the observed current.

With a term for band-to-band impact ionization by hot electrons, the carrier continuity equations are

$$\frac{dn}{dt} = g - \frac{n}{\tau_e} + \alpha_{bb,e}(E) n v_e(E) - \frac{1}{e}\frac{dJ_e}{dx} \tag{2.26}$$

$$\frac{dp}{dt} = g - \frac{p}{\tau_h} + \alpha_{bb,e}(E) n v_e(E) + \frac{1}{e}\frac{dJ_h}{dx}, \tag{2.27}$$

where $\alpha_{bb,e}(E)$ is the ionization rate and v_e is the electron velocity as defined in Eq. 2.24. In the charge-neutral bulk of the device and in steady-state, these equations lead to $n = g\tau_e/(1 - \alpha_{bb,e}(E)v_e(E)\tau_e)$ and $p = g\tau_h/(1 - \alpha_{bb,e}(E)v_e(E)\tau_e)$, instead of the usual $n = g\tau_e$ and $p = g\tau_h$. The predicted current is then a modified version of Eq. 2.25:

$$I = g(P)\left(\frac{\tau_e v_e(E)}{1 - \alpha_{bb,e}(E)v_e(E)\tau_e} + \frac{\tau_h \mu_h E}{1 - \alpha_{bb,e}(E)v_e(E)\tau_e}\right) w\delta. \tag{2.28}$$

By matching Eq. 2.28 to the data of Fig. 2-25 at the highest illumination intensity, we extracted $\alpha_{bb,e}$ at every data point, effectively extending the low-bias model to high-bias by adding the one parameter $\alpha_{bb,e}(E)$. The results are plotted in Fig. 2-28, with the ionization rate of normal GaAs shown for comparison. Though $\alpha_{bb,e}$ depends on E as $\alpha_{bb,e} = A\exp(-E_0/E)$, as is expected for impact ionization (see [36]), the value of E_0 ($\sim$ 6x10^4 V/cm) is about 100 times less than its value in normal GaAs ($\sim$ 6x10^6 V/cm). This is physically impossible, because μ_e is much less in LTG GaAs than in normal GaAs. We therefore rule out band-to-band impact ionization by hot electrons as the cause of superlinearity.

In a similar fashion, we rule out band-to-band impact ionization by hot holes. We replace the generation term $\alpha_{bb,e}(E)nv_e(E)$ in Eqs. 2.26 and 2.27 with $\alpha_{bb,h}(E)p\mu_h E$, and fit an altered version of Eq. 2.28 to our data. The extracted $\alpha_{bb,h}(E)$ is plotted in Fig. 2-28. The values of $\alpha_{bb,h}$ are again much higher than expected, especially at

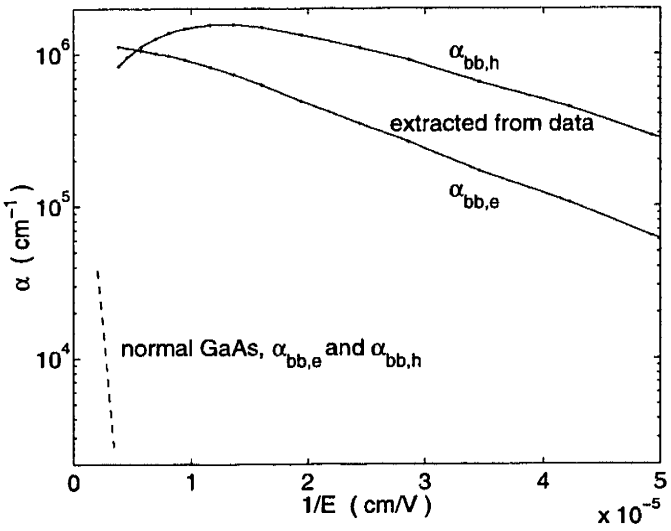

Figure 2-28: Band-to-band impact ionization rates of electrons and holes vs. reciprocal electric field, extracted from separate fits of our model to our data at high bias (see Fig. 2-25 for the low-bias fit). Ionization rate of electrons and holes in normal GaAs is shown for comparison [36].

low E. It is also unacceptable that $\alpha_{bb,h}$ does not increase monotonically with E.

The impact ionization of occupied donor states by hot electrons or holes is another possible cause of the superlinear I-V curve. In either case the free hole population is not augmented, because the ionized electron leaves behind a nonconductive hole in the donor band, not a hole in the valence band. The generation terms are the same as mentioned above, but now the enhanced current is

$$I = g(P)(\frac{\tau_e v_e(E)}{1 - \alpha_{d,e}(E) v_e(E) \tau_e} + \tau_h \mu_h E) w \delta \tag{2.29}$$

in the case of donor ionization by hot electrons, and

$$I = g(P)(\tau_e v_e(E)(1 + \alpha_{d,h}(E) \mu_h E \tau_h) + \tau_h \mu_h E) w \delta. \tag{2.30}$$

in the case of donor ionization by hot holes. We again extracted $\alpha_{d,e}$ and $\alpha_{d,h}$ from our measured data by separately fitting Eqs. 2.29 and 2.30 to the measured I-V curve at highest illumination of Fig. 2-25. The results are plotted in Fig. 2-29.

We expect $\alpha_{d,e}$ and $\alpha_{d,h}$ to be of the form $\exp(-E_0/E) N_d^0 \sigma$, where N_d^0 is the

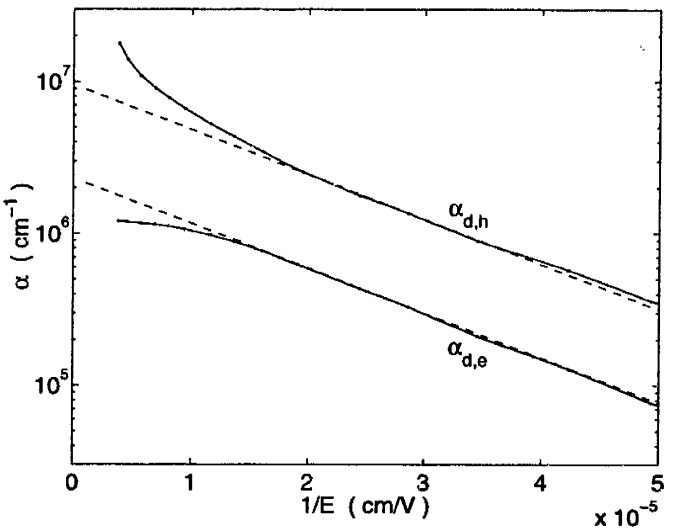

Figure 2-29: Donor impact ionization rates of electrons and holes vs. reciprocal electric field, extracted from separate fits of our model to our data at high bias (see Fig. 2-25 for the low-bias fit). Fits to $\alpha_{d,e}$ and $\alpha_{d,h}$ of the form $A\exp(-E_0/E)$ are also shown.

concentration of impact ionization sites, σ is their cross section and $\exp(-E_0/E)$ is the fraction of the carrier concentration with enough kinetic energy to ionize an occupied donor. We fit lines of the form $A\exp(-E_0/E)$ to the values of $\alpha_{d,e}$ and $\alpha_{d,h}$ at low fields (see Fig. 2-29), and extracted a value of A of 2.3x10^6 cm^{-1} and a value of E_0 of 68 kV/cm for ionization by electrons, and a value of A of 9.5x10^6 cm^{-1} and a value of E_0 of 68 kV/cm for ionization by holes. Both values of A are comparable to the product of the donor concentration and the cross sections found in Table 2.2. The values of E_0 are again 100 times lower than the value of E_0 for band-to-band impact ionization in normal GaAs. While the energy required to ionize a donor ($\sim$ 0.7 eV, see Sec. 2.2.1) is less than the GaAs band gap (1.42 eV [36]), it is not low enough to account for the difference in E_0.

The behaviors of $\alpha_{d,e}$ and $\alpha_{d,h}$ at high fields are physically unreasonable. $\alpha_{d,e}$ saturates at an electric field of about 140 kV/cm, which means at that field 100% of the electrons have enough kinetic energy to ionize occupied donors. A field-induced non-thermal kinetic energy distribution with a negligible fraction of low-energy electrons is impossible. The marked increase of $\alpha_{d,h}$ at high fields is also nonphysical. Plots of the band-to-band impact ionization rates α of different materials, when plotted as

in Fig. 2-29, show a slight roll off at high field [36]. Impact ionization of filled states in the valence band and in the donor band should share the same field-activation characteristics, because both are due to field-induced carrier heating, thus we rule out impact ionization of donor states by hot carriers of both types.

Our efforts to attribute the cause of our superlinear I-V curve to impact ionization fail because we do not observe the exponential increase in current with voltage that impact ionization implies. Fig. 2-25 shows that in the bias voltage range where high-field effects are important, between approximately 6 V and 47 V, the current increases by only a factor of 23 while the voltage increases by a factor of 7.5. We seek a high-field effect that has a power-law dependence on electric field to explain our superlinear I-V curve.

Ning [56] and others studying electron capture in SiO_2 observed a decrease in the capture cross section of a Coulomb-attractive (positively-charged) electron trap with increasing electric field. For electric fields less than 10^6 V/cm, the capture cross section is proportional to $E^{-\frac{3}{2}}$, and the decrease is caused by barrier-lowering of the trap's Coulombic potential by the applied field. At electric fields higher than 10^6 V/cm, the capture cross section is proportional to E^{-3}, and the extra factor of $E^{-\frac{3}{2}}$ is due to electron heating. It is attractive to attribute the superlinear I-V curve we observe to one of the above mechanisms.

To represent a field-dependent capture cross section in our model, we simply make the electron and hole capture times field dependent. The capture times are inversely proportional to the capture cross sections (see Eq. 2.1). The expressions for the current are then

$$I = g(P)(\tau_e(E)v_e(E) + \tau_h\mu_h E)w\delta \tag{2.31}$$

in the case of a field-enhanced electron capture time, and

$$I = g(P)(\tau_e v_e(E) + \tau_h(E)\mu_h E)w\delta \tag{2.32}$$

in the case of a field-enhanced hole capture time. We extracted $\tau_e(E)$ and $\tau_h(E)$ separately from our data just as we extracted the ionization rates above. The results

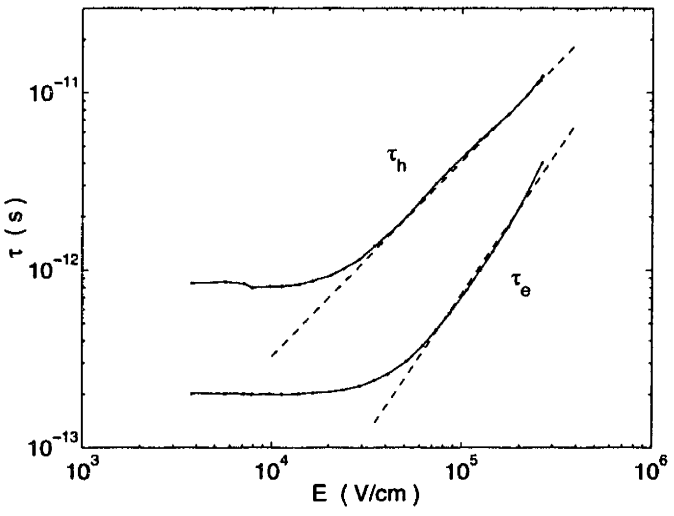

Figure 2-30: Electron and hole capture times vs. electric field, extracted from separate fits of our model to our data at high bias (see Fig. 2-25 for the low-bias fit). Power-law fits at to τ_e and τ_h at high field are also shown. τ_e is proportional to $E^{1.6}$, and τ_h is proportional to $E^{1.1}$

are plotted in Fig. 2-30. Note that above threshold fields, both τ_e and τ_h have a power-law dependence on E, in agreement with the above models. In fact, τ_e is proportional to $E^{1.6}$ for $E < 10^6$ V/cm, in agreement with Ning's formula for barrier-lowering-induced changes in the cross section. It is τ_e rather than τ_h that we would expect to be subject to barrier lowering, because the electron capture site is the positively charged, unoccupied donor state, and the hole capture site is the neutral, occupied donor state.

Dussel *et al.* [57] calculated the barrier-lowering-induced dependence of τ_e on E by assuming that a trap's capture cross section is proportional to the effective volume of its Coulomb well. The volume is critical and not the cross sectional area because the probability of phonon emission (and hence capture) during transit of the well is factored in to the capture cross section. The effective volume of the well is the volume for which the potential is $2kT/e$ below the potential maximum of the lowered barrier. In cylindrical coordinates, this is expressed as all r and z such that

$$\frac{-e}{4\pi\epsilon(r^2+z^2)^{1/2}} - Ez < -\sqrt{eE/\pi\epsilon} - 2kT/e, \tag{2.33}$$

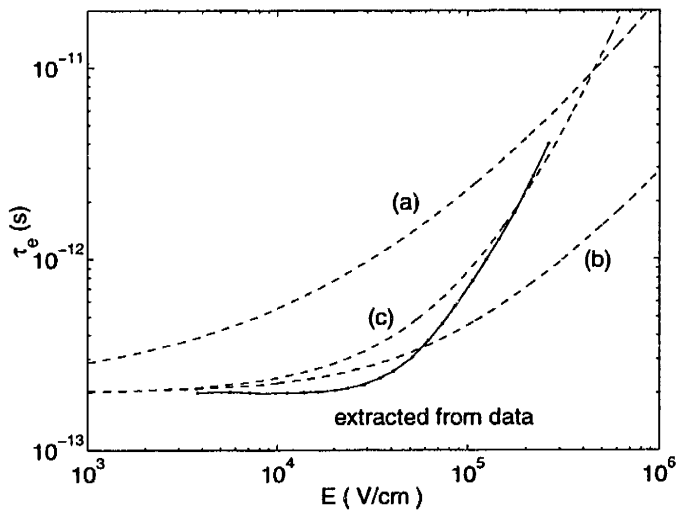

Figure 2-31: τ_e vs. E as extracted from our data compared with three models for $\tau_e(E)$. Model (a) is from [56], model (b) includes the effect of nearest-neighbor traps, and model (c) includes the effects of nearest-neighbor traps and electron heating.

where E is in the positive z direction, and $-\sqrt{eE/\pi\epsilon}$ is the barrier-lowering term. Ning analytically integrated the volume defined in Eq. 2.33 to find the ratio $\frac{\sigma(E)}{\sigma(E=0)}$. We invert this ratio to find the ratio $\frac{\tau_e(E)}{\tau_e(E=0)}$, then assume $\tau_e(E=0)$ is 0.2 ps, as we have before. The resulting $\tau_e(E)$ is plotted in Fig. 2-31, where we show τ_e as extracted earlier from our data. The predicted $\tau_e(E)$ is proportional to $E^{\frac{3}{2}}$ at very high E, and levels off at a constant value as E goes to zero because the barrier-lowering term in Eq. 2.33 becomes negligible compared to $2kT/e$. The transition between these two regimes takes place over a much greater range of electric fields than what we observe.

One thing that may supress the field-dependence of τ_e at low fields, and make $\tau_e(E)$ more similar to what we observe, is the effect of neighboring traps on a trap's local potential. This should be an important effect in our LTG GaAs because the density of unoccupied traps (N_d^+) is about 10^{19} cm^{-3}. We incorporate a nearest-neighbor into Dussel's model by generalizing Eq. 2.33 as follows:

$$\frac{-e}{4\pi\epsilon(r^2+z^2)^{1/2}} - Ez - \frac{e}{4\pi\epsilon|\mathbf{r}-\mathbf{r_0}|} < V_{\max} - 2kT/e, \tag{2.34}$$

where $\mathbf{r_0}$ is the position vector of the nearest neighbor and $V_{\max}$ is the lowest local maximum in the potential (which is the left-hand side of Eq. 2.34). The volume

defined by Eq. 2.34 should be averaged over all $\mathbf{r_0}$ appropriate to the unoccupied donor density. To make this calculation more tractable, we make the following one-dimensional analog of Eq. 2.34:

$$\frac{-e}{4\pi\epsilon|z|} - Ez - \frac{e}{4\pi\epsilon|z-z_0|} < V_{\max} - 2kT/e, \tag{2.35}$$

where z_0 is approximately (though probably slightly greater than) $N_d^{+\,-\frac{1}{3}}$. At a certain $z = z_1$ $(0 < z_1 \leq \frac{z_0}{2})$, the left and right sides of Eq. 2.35 are equal. We assume that the effective volume of the trap potential is proportional to z_1^3. We calculated a modified version of $\tau_e(E)$ by assuming $\tau_e \propto z_1^{-3}$ and setting $\tau_e = 0.2$ ps at $E = 0$. The modified $\tau_e(E)$ is plotted in Fig. 2-31. We choose the value of z_0 which fits our data best. This value is 9 nm, which corresponds to a trap density of approximately 10^{19} cm^{-3}.

Though the second calculation of $\tau_e(E)$ fits our data better than the first, the observed τ_e increases more rapidly with E than we predict. This may be due to electron heating, which, as discussed above, causes τ_e to increase by an extra factor of $E^{\frac{3}{2}}$. We include electron heating in our model as follows. Ning found that the ratio $\frac{\sigma(T_e)}{\sigma(T_e=T)}$ is $(\frac{T}{T_e})^{\frac{3}{2}}$, where T_e is the electron temperature and T is the lattice temperature. We estimate T_e as $T + e\lambda E/k$, where λ is the optical phonon mean free path [56]. We add a factor of $(1 + e\lambda E/kT)^{\frac{3}{2}}$ to our previous expression for $\tau_e(E)$ and treat λ as a fitting parameter. This final version of $\tau_e(E)$ is plotted in Fig. 2-31. The best fit is achieved with a z_0 value of 7 nm and a λ value of 2 nm. This value of λ is comparable to the optical phonon mean free path in normal GaAs, which is 5.8 nm [36]. The z_0 value is almost the same as that found above.

We find further evidence that both barrier lowering and electron heating help determine $\tau_e(E)$ by examining the dependence of the photocurrent on ambient temperature. Equations 2.33, 2.34 and 2.35 all show that at any given electric field, the capture cross section decreases with increasing temperature, due to the increased magnitude of the $2kT$ term. The electron-heating contribution to σ, however, increases with increasing temperature, because λ decreases with temperature. The first

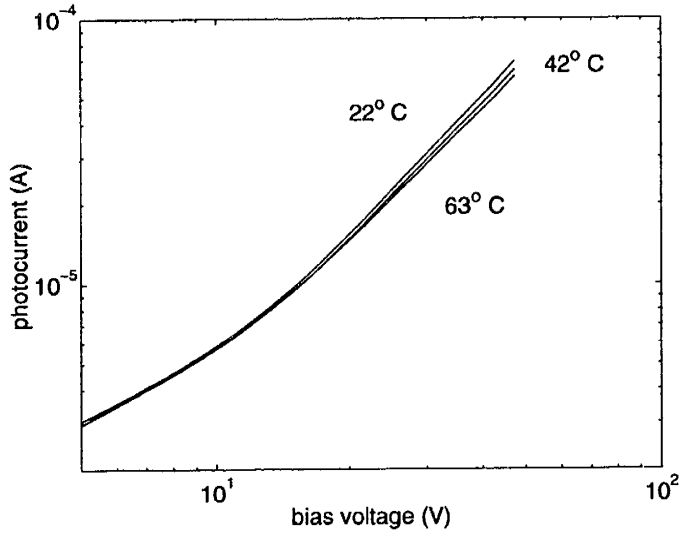

Figure 2-32: Photocurrent vs. bias voltage at different temperatures. Only high-bias data are shown because noise from the thermocouple is prominent at low bias.

different temperature dependence is dominant at low bias, though the two dependencies cancel each other at high bias, where electron heating is significant, as observed by Ning.

I-V curves measured at three temperatures are shown in Fig. 2-32, over the bias voltage range for which τ_e is field-dependent. At low voltages, the photocurrent is nearly independent of temperature, while at high voltages, the photocurrent decreases with increasing temperature. Keeping mind that τ_e and the photocurrent are inversely proportional to σ, the trend in the data agrees with the expected trend, namely, that the signature temperature-dependence of electron heating becomes more dominant as the bias voltage increases. However, there appears to be a factor of the photocurrent with a negative temperature dependence at all biases that we haven't accounted for. That factor is probably the electron velocity.

2.6 Time-resolved measurements

The field-dependent τ_e that is the best explanation for our superlinear I-V curve at high bias should effect our photoconductor's dynamic response to time-varying illumination. τ_e is the decay time with which the electron concentration relaxes back

to equilibrium following a pulse of illumination. We sought to experimentally observe this decay to verify our model derived in the previous section.

The measurement of electrical transients with subpicosecond time resolution is typically performed optoelectronically. Measurement techniques almost always employ a modelocked Ti:sapphire laser, which typically emits optical pulses of 50 to 100 fs duration, because of its inherently superb time resolution. It can be used in a variety of ways to detect a variety of transients, including electron and hole concentration transients [24], and photocurrent transients [58, 59, 60]. Our aim is to observe an electron concentration transient in an applied electric field. One way to do this would be to measure the time-resolved reflectance or transmittance [4] of the active region of a photoconductor with an applied bias. The reflectance and transmittance of above-band-gap light depend on the electron concentration because of conduction band filling [27]. Keil *et al.* [47] performed such an experiment, and observed a longer decay time of the transmittance of 840-nm-wavelength light with an applied bias than without. However, they interpreted the limited amount of data they presented in terms of field screening and the Franz-Keldysh effect without presenting a detailed model. We do not believe field screening takes place during uniform illumination, because of adequate electron injection from the cathode.

We measured the electron concentration transient by measuring the photocurrent transient. At a given electric field, the photocurrent is proportional to the electron concentration because of the low hole mobility of LTG GaAs. Though we did not measure the photocurrent transient this way, the most direct way to measure it is as follows. As discussed in Sec. 2.3, when an optical pulse excites carriers in our biased photoconductor, the transient photocurrent creates a propagating electromagnetic (EM) pulse in the coplanar waveguide (CPW) the photoconductor is embedded in. Over short distances ($\sim 100\mu$m) of propagation, the CPW can be assumed to be lossless and dispersionless, so the EM pulse is an analog of the photocurrent transient. The EM pulse can be sensed electro-optically with ~ 0.3 ps time resolution [61], but

[4] The reflectance or transmittance of a "probe" optical pulse as a function of time after a "pump" pulse generates carriers at the same spot.

this involves equipment we did not have access to.

We took advantage of the nonlinear saturating response of the EM pulse to the incident optical intensity to measure the autocorrelation of the photocurrent transient [60]. We measure the dc current through our photoconductor as a function of the time delay between two optical pulses. Each pulse individually excites a propagating current $i(t) = i_0(\mathcal{E})\exp(-t/\tau_e)$ in the CPW, where $\mathcal{E}$ is the optical pulse energy (the optical pulse duration is negligible compared with τ_e). $i_0(\mathcal{E})$ is proportional to $\mathcal{E}$ at low $\mathcal{E}$, but saturates at $\frac{V_b}{2Z_0}$, where V_b is the bias voltage and Z_0 is the characteristic impedance of the CPW's odd propagating mode (see Sec. 2.3), because $2Z_0$ is effectively the resistance in series with our embedded photoconductor at picosecond time scales (see Fig. 2-18). Assuming each of optical pulses we apply excites identical $i(t)$, the dc current we measure is

$$I_{\rm dc}(\tau) = 2\langle i(t)\rangle - A\langle i^2(t)\rangle - A\langle i(t)i(t-\tau)\rangle + ..., \tag{2.36}$$

where A is a coefficient that expresses the photoconductor's saturability, and τ is the delay time between pulses. We operate at as low $\mathcal{E}$ as possible to make the higher order nonlinear terms in Eq. 2.36 negligible. The τ-dependent part of $I_{\rm dc}$ is the autocorrelation of $i(t)$.

To perform the autocorrelation measurement, we used the same Ti:sapphire laser and focusing optics that we used to do the cw measurements, though this time we made the laser pulse and split the beam into two beams with a beamsplitter. Both beams were recombined with a second beamsplitter and focused on the active region of the photoconductor with the same microscope objective. Each beam was individually aligned by maximizing the dc current it produced. The path length of the first beam was controlled by a retroreflector mounted on a motor-driven translation stage, and the path length of the second beam was dithered at 20 Hz by a retroreflector mounted on an audio speaker. The dc photocurrent was ac coupled with a cutoff frequency of 0.15 Hz to a transimpedance amplifier, whose output was connected to an oscilloscope synchronized to the speaker, so that the oscilloscope displayed the autocorrelation in

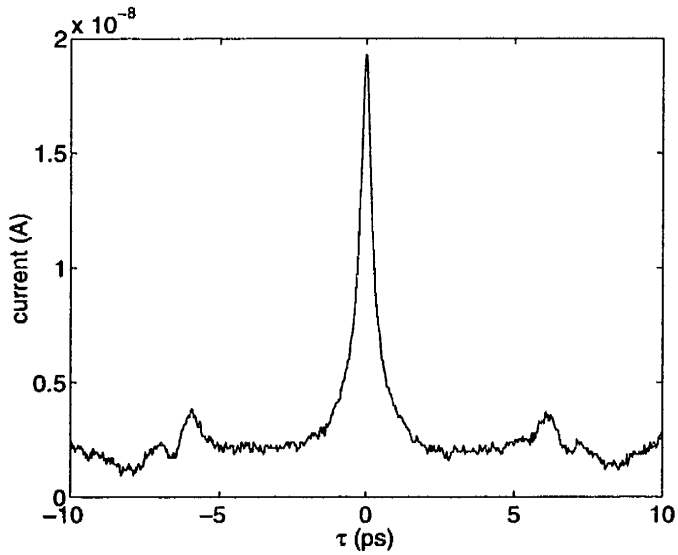

Figure 2-33: Typical autocorrelation data. Measured at a bias voltage of 10 V, with a total incident power of 1.75 mW.

real time. The translation stage was adjusted to make zero-path-difference occur when the speaker-mounted retroreflector was midway through its travel. The full speaker throw was about 4 mm, enabling us to view a range of τ of about 27 ps. The Ti:sapphire laser's repetition rate is 82 MHz, which is much faster than the speaker's oscillation frequency, but much slower than τ_e, so the oscilloscope showed in real time the interaction of the two laser pulses with near-zero path difference, but no other pulses were involved. With the help of a quarter-wave plate, the two incident beams were cross-polarized to avoid coherence effects [60, 62].

Typical autocorrelation data are shown in Fig. 2-33. The amount of power in each of the beams was adjusted to make the autocorrelation symmetric. The power in the beam polarized parallel to the center conductor of the CPW was 0.53 mW, and the power in the cross-polarized beam was 1.22 mW. Since the gap length is comparable to the optical wavelength (779 nm), the unbroken dimension of the center conductor (perpendicular to the center conductor) is more reflective than the broken one, and the center conductor is similar to a wire-grid polarizer. The central feature of the autocorrelation is a double-sided exponential decay, which is the expected autocorrelation of the single-sided exponential decay $i(t)$. The double-peaked features

at about $\tau = \pm 6.5$ ps correspond to the interaction between the reflection of an EM pulse off the end of the coplanar waveguide and the delayed optical pulse. As noted in Sec. 2.3, the expected round trip travel time between the photoconductor and the end of the waveguide 0.365 mm away is 6.6 ps. These features have an odd shape because an EM pulse distorts upon reflection at the somewhat capacitive CPW termination (see Fig. 2-18).

Though the total power used in the autocorrelation measurement described above is low compared to the cw power used in the measurements described earlier, the instantaneous power of each pulse is quite high, and we must investigate whether or not the effects of the high density of photogenerated carriers are negligible. In Sec. 2.5, we discussed the geometrical and physical parameters that control the relationship between the cw laser power and the steady-state carrier densities. To predict the carrier densities immediately following an optical pulse, we apply the same parameters, and assume that no carrier capture takes place during the optical pulse. This is a good assumption, because we infer a pulse width of 55 fs from the pulsing laser's 12.4-nm-wide spectrum (assuming the pulse width is fourier-transform limited). We calculate a carrier density of $1.05\text{x}10^{18}$ cm^{-3} per milliwatt of average laser power. For the 1.75 mW of total average power used to obtain the data of Fig. 2-33, we calculate a maximum carrier density of $1.8\text{x}10^{18}$ cm^{-3}, which is five times less than the lowest defect density (N_a, see Table 2.2), thus the photogenerated carriers have a negligible impact on the balance of charge in the bulk of the photoconductor.

We must also verify our assumption that i_0, the initial current of the photocurrent transient, is less than $\frac{V_b}{2Z_0}$, which as described above is the maximum current the bias voltage V_b can supply to the EM pulse. At a bias voltage of 10 V (the conditions of Fig. 2-33), electrons travel at their saturation velocity, and the total current the above maximum carrier density can generate in our experimental device is 35 mA. This a factor of three less than $\frac{V_b}{2Z_0}$ for $V_b = 10$ V and $Z_0 = 50\ \Omega$, thus we are justified in neglecting the higher order terms of Eq. 2.36.

We measured autocorrelations at seven different bias voltages and extracted τ_e from them with the following formula, which is the appropriate extraction of the

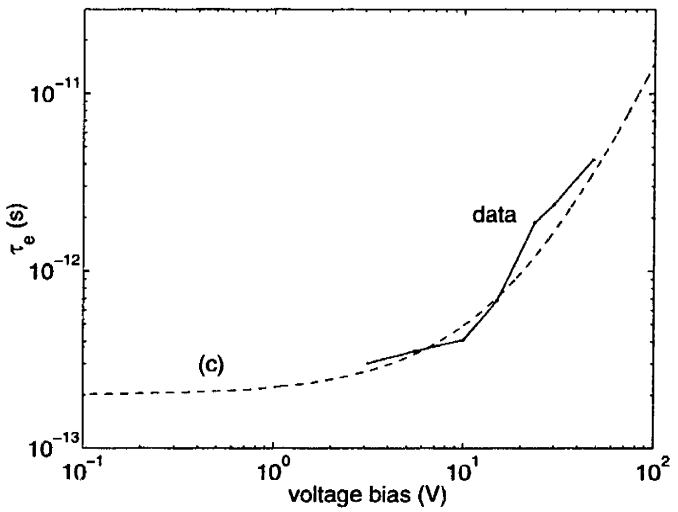

Figure 2-34: τ_e vs. bias voltage as extracted from autocorrelation measurements, compared with model (c) of Fig. 2-31

decay time of a double-sided exponential: $\tau_e = \frac{\tau_{\mathrm{FWHM}}}{2\ln(2)}$, where τ_{FWHM} is the full autocorrelation width at half maximum. The data are plotted in Fig. 2-34, where they are compared with the final model for τ_e discussed in the last section. The agreement is quite good over the full voltage range considered, thus data taken with both static and dynamic illumination can be explained with the same model of electron capture in LTG GaAs at high fields. The apparent noise in the data is not because of noise in each autocorrelation, but because of difficulty in determining the peak and baseline of each one. The peak and baseline of the data in Fig. 2-33 are obvious, but in some cases the baseline is not that flat (especially at high bias, when the central peak is very broad), and a small peak due to coherence sits atop the main peak because the two beams were not perfectly cross-polarized. The dithered-delay technique is very effective at reducing noise in the autocorrelation because the digital oscilloscope can average over many speaker oscillations (we averaged each autocorrelation for about 90 s).

2.7 Discussion

The main conclusion of this chapter is that the high dc photocurrent and slow response of an LTG GaAs photoconductive switch at high voltage bias is caused by an increase in the electron capture time τ_e of Coulombic attractive donor states due to electron heating and Coulomb-barrier lowering. The model we use to predict τ_e as a function of applied electric field has been used to model electron trapping in SiO_2, and includes two fitting parameters (the optical phonon mean free path and the average spacing of ionized donor states) for which we find physically reasonable values. Other authors have measured data similar to ours, and offered explanations based on injection-limited currents [11] and impact ionization [10]. We show that neither of these theories explain our data, because the defect densities in our LTG GaAs are too high to allow injection-limited currents at the bias voltages of interest, and an explanation based on impact ionization would imply an unreasonably low electric field threshold. Other authors have measured thermally-generated currents in dark LTG GaAs that behave similarly to our photocurrents [13, 35], and based their models on electric-field-enhanced *emission* of free carriers, which is different from but has a similar field dependence to electric-field-reduced *capture*.

We are the first group to show that the same electron capture process that determines the steady-state electron concentration induced by cw illumination also determines the transient response to pulsed illumination. Our dc photocurrent data and time-resolved photocurrent data can be explained with the same model, as can our measurement of the time-resolved reflectance. This implies that we are correct in ignoring all electron and hole capture mechanisms, such as hole trapping by acceptors, except for capture by donor states. This is probably because we use lightly annealed LTG GaAs, in which both electrons and holes are known to trap readily and recombine [23] at As antisites that behave as donors but may be slightly precipitated [35]. The fast hole capture time of the donor states keeps a substantial concentration of holes from being trapped by acceptors and then slowly recombining. Fast electron and hole trapping at different sets of defects followed by slow recombination is known

to occur in as-grown LTG GaAs and some annealed LTG GaAs [23, 24, 28], but such processes are not evident in our material. Evidence of these processes would be higher steady-state electron and hole concentrations induced by cw illumination (and hence higher photocurrent) than what would be expected from the decay times of photocurrent and reflectance transients, because these concentrations are determined solely by the capture times of recombination centers, not traps. Other evidence of hole trapping would be a superlinear dependence of the steady-state electron concentration on cw illumination intensity. If trapped holes would substantially empty the acceptors, then the concentration of ionized donors would have to decrease to maintain charge neutrality. The ionized donors are electron capture sites, so the steady-state electron concentration would increase. It would be interesting to try to observe the above effects by studying steady-state photocurrents in as-grown LTG GaAs, for which recombination is a slow process. There has never been such a study, perhaps because the dark currents in as-grown LTG GaAs are high.

In general, additional information about capture and recombination processes in a semiconductor comes from illumination at high enough intensities that the electron and hole concentrations become comparable to or greater than the defect densities. With LTG GaAs, this is only possible with pulsed illumination because the defect concentrations are very high and the electron and hole lifetimes are very low. Such illumination was used by both Lochtefeld *et al.* [23] and Sosnowski *et al.* [63] to estimate defect concentrations in LTG GaAs and to measure both the electron and hole capture times of donor states, all with one type of experiment, a time-resolved transmittance measurement. All the experiments in this chapter, including the pulsed illumination experiments, were performed at low enough intensity to avoid upsetting the charge balance between ionized donors and acceptors. It would be interesting to examine the high-intensity regime to verify our model of electron and hole capture.

In Sec. 2.3.1 we discuss simulations of our device in two dimensions, and note that the dark regions under the contacts of an illuminated planar photoconductor might form a high resistance in series with the illuminated bulk and thereby limit the photocurrent. In this chapter we ignore this dark region and assume that the

full voltage bias falls across the illuminated region, and therefore the electric field is V/l, where l is our photoconductor's gap length. However, we have measured the I-V curves of illuminated photoconductors with different gap lengths and found that the threshold voltage for the increase in electron capture time is a sublinear function of the gap length. A voltage drop near the contacts may explain this sublinearity. As we note in Sec. 2.3.1, measurement of an illuminated TLM-type structure would make the contact resistance distinguishable from the bulk resistance. If the dark region proves to be a problem, alternative means of illumination can be tried, including backside illumination of an LTG GaAs layer removed from its SI GaAs substrate and mounted on glass, illumination via a waveguide [64], and reflection of light from a Bragg reflecting stack under the LTG GaAs layer [50].

In Sec. 2.5 we extract a value of 164 cm^2/Vs for the low-field mobility μ_e of photogenerated electrons from the measured photocurrent, by assuming the electron concentration is $g\tau_e$, where g is the carrier generation rate induced by illumination, and τ_e is the electron capture time measured at low-field by time-domain reflectometry. This value of μ_e is similar to values measured directly with the Hall effect by Look *et al.* [21], who used LTG GaAs annealed at lower temperatures than ours (450 °C - 600 °C for them compared with 580 °C for us) though Stellmacher *et al.* [22] measured values ten times as high for LTG GaAs annealed at 600 °C with sub-picosecond τ_e. High electron mobility is critical for high output of sub-millimeter wave emitters, perhaps more so than short τ_e (since output is independent of τ_e at $f > \frac{1}{2\pi\tau_e}$), and should be optimized, especially since a factor of ten variation is large. Hall measurements of illuminated LTG GaAs should be used to measure μ_e and the steady-state electron concentration, and such measurements should be used to optimize the LTG GaAs growth and annealing temperatures.

Much of the debate in the LTG GaAs field involves attributing various physical properties such as dark current and τ_e to specific types of defects. The role of As precipitates is especially debated. While we note in Sec. 2.2.2 that As precipitation seems to be essential for rapid electron and hole capture by the same defect, the model of our annealed LTG GaAs that we introduce in 2.2.4 does not contain islands of metal-

lic As (as As precipitates are often modeled [65]), instead it contains As antisites that act as donors and serve as electron and hole capture centers. Our justification for this is based on the work of Luo *et al.* [37], who found that As antisites behave similarly to and can be considered the atomic source of As precipitates. Their main evidence is the hopping current, which depends only on the spacing between As atoms or clusters, whether the As has precipitated or not. We assume that the similarity between As antisites and precipitates extends to their behavior as recombination centers. One physical justification for this is that they both have potentials that attract electrons: the donor-like As antisites are Coulomb attractive, and the As precipitates have an attractive depletion region around them, as shown in Fig. 2-5. Thus they would both be subject to the capture cross section reduction by electron heating and barrier-lowering that we observe. One observable difference between LTG GaAs with a large concentration of As antisites and LTG GaAs with a large concentration of As precipitates would be the threshold voltage of injection-limited currents. In LTG GaAs with a high concentration of As antisites, the threshold voltage is high because ionized donors can create a high charge density near the contacts (see Sec. 2.2.4). It is more difficult to calculate the charge density in heterogeneous LTG GaAs with metallic islands of As, but we suppose the precipitates would not ionize, and therefore less charge density would be available to the contacts and the threshold voltage for injection-limited current would be lower.

One topic that requires more theoretical work is the screening of an applied bias field by photogenerated carriers. We believe this should not be evident during uniform illumination of an LTG GaAs photoconductor, because its cathode is electron-injecting (see Sec. 2.2.3), and electrons near the cathode accelerated by the applied field are replaced by electrons from the metal contact. However, many authors have claimed that field screening does occur in LTG GaAs [30, 43, 47]. Screening is an effect that becomes prominent at high illumination intensity and low bias, thus it is definitely not the cause of phenomena we observe at high bias and moderate intensity. Screening does occur in normal GaAs photodetectors with Schottky contacts [66], but one should be careful to assume that it occurs in LTG GaAs photoconductors as well.

The autocorrelation measurements we performed provide important verification of the increase in electron capture time with voltage bias, and are a particularly simple pump-and-probe, time-resolved measurement. The coplanar waveguides with embedded photoconductors that we fabricated are quite simple and small (see Fig. 2-18), and could serve as a standard diagnostic device on any ultrafast photoconductive substrate to evaluate the electron capture time as a function of voltage bias. Though a theoretical description of these devices and how they function as autocorrelators exists [60], that description has never been completely experimentally verified. While the temporal widths of the autocorrelations make sense and agree with other time-resolved data, the dependence of amplitude and shape of the autocorrelation peak on the illumination intensity and bias voltage has never been investigated. Chen *et al.* [59] did verify the saturating dependence of the photocurrent on the pulsed illumination intensity, which is the nonlinearity that makes the autocorrelation measurable. They observed that the transient photocurrent in an LTG GaAs photoconductor embedded in a coplanar transmission line is current limited by the characteristic impedance of the line. However, they observed the transient photocurrent directly with electro-optic sampling, and did not measure its autocorrelation. It would be interesting to find out how both the nonlinearity due to the current limit and any nonlinearity due to high carrier concentrations effect the autocorrelation.

Chapter 3

A Novel Photoconductor and Coplanar Waveguide Circuit for Submillimeter-wave Spectroscopy

3.1 Introduction

One of the main uses of ultrafast photoconductors, such as the LTG GaAs photoconductor discussed in the last chapter, is as the generators and detectors of electrical transients for time-domain spectroscopy of electronic device and circuits. The bandwidth of optoelectronic measurements involving photoconductors is near 1 THz, which is substantially greater than the typical 100-GHz bandwidth of all-electronic means of device testing [67], and allows accurate measurement of the high-frequency dynamics of today's fastest electronic devices, with cutoff frequencies above 500 GHz [2]. Photoconductive generation and detection have been used to characterize active devices such as modulation-doped field-effect transistors[10, 68, 69, 70, 71] and resonant tunelling diodes, and passive coplanar transmission lines [72, 73] and discontinuities in transmission line circuits [67, 74, 75].

These measurements typically involve circuits composed of high-bandwidth transmission lines in which photoconductors and the device of interest are embedded. The

photoconductor that generates the electrical transient (the "pump" photoconductor) is voltage-biased and illuminated by optical pulses from a mode-locked laser, which instantaneously short the conductor such that it launches guided electromagnetic pulses on to the transmission line. The pulses propagate down the transmission line towards the device, where they are both transmitted and reflected. Both the transmitted pulses and reflected pulses contain information about the device's S-parameters. These pulses are detected with a second, unbiased "probe" photoconductor, or with an electrooptic crystal.

The transmission lines and embedded elements of the measurement circuit must be designed to limit the distortion of the propagating electrical pulses. Many different types of distortion are possible, including pulse dispersion and attenuation caused by straight segments of transmission line, and spurious pulses caused by photoconductors, wires needed for biasing, and other discontinuities in the transmission line.

Coplanar waveguide (CPW), which consists of a strip centered between two ground planes, is perhaps the type of transmission line that causes the least pulse distortion. It shares certain advantages over microstrip with other coplanar transmission lines: it can be made with micron precision using photolithography, which pushes the cutoff frequency of undesirable high-order modes far above one terahertz; and it can be integrated with planar active devices without making large discontinuities such as through holes. Experiments have shown CPWs with narrow ground planes to be less attenuative and dispersive than microstrip and coplanar strips at subterahertz frequencies [73, 76]. Signals traveling on CPWs are less susceptible to distortion by freely propagating radiation than signals on coplanar strips, because a CPW's signal-carrying center conductor is shielded on both sides by its ground planes, while coplanar strips are unshielded [10].

The main disadvantage of CPWs is that they allow two quasi-transverse-electromagnetic (TEM) propagating modes, compared to the single quasi-TEM propagating mode of coplanar strips. The modes are called even and odd according to the symmetry of each mode's electric field with respect to the CPW's center conductor (see Fig. 2-19). The even mode has a wider extent than the odd mode in the direction

transverse to the CPW, because its characteristic dimension is the distance between the two ground planes, while the odd mode's characteristic dimension is the distance between each ground plane and the center conductor. The even mode's extra width makes it more dispersive and attenuative than the odd mode in the subterahertz frequency range, because dispersion occurs when a mode's width is comparable to the wavelength, and radiative attenuation increases with the square of the width [72, 76]. Since the two modes have different propagation characteristics, any asymmetry or discontinuity in a circuit that mixes the modes causes distortion. Every useful circuit must contain some discontinuities, usually at active devices or at photoconductive switches, and at breaks in the CPW's ground plane which allow access to its center conductor. Even if these discontinuities have mirror symmetry with respect to the center conductor, the unwanted even mode of the CPW can still be excited if the laser beam that illuminates the pump photoconductor is misaligned.

Modal distortion must be controlled if CPWs are to be useful. Air bridges have been used to connect the two ground planes of a CPW and suppress the even mode [10, 75]. Several authors have optoelectronically sensed the electric field on either side of the center conductor and thereby discriminated between the odd and even modes, allowing the meaningful and spurious parts of signals to be distinguished [10, 77]. In this chapter we discuss the design and testing of a simple single-layer CPW circuit that makes air bridges unnecessary and allows mode discrimination and selective mode generation without requiring optoelectronic sampling. The circuit includes both a pump and a probe photoconductor for fiber-coupled measurements of active devices inside a cryostat [78], which is an environment where optoelectronic sampling is difficult [79].

3.2 The experimental device

Figure 3-1 shows a schematic diagram of our circuit. There are photoconductive switches at the pump and probe spots. These switches are novel in that each switch has two active regions, grounded by and located on either side of the CPW's center

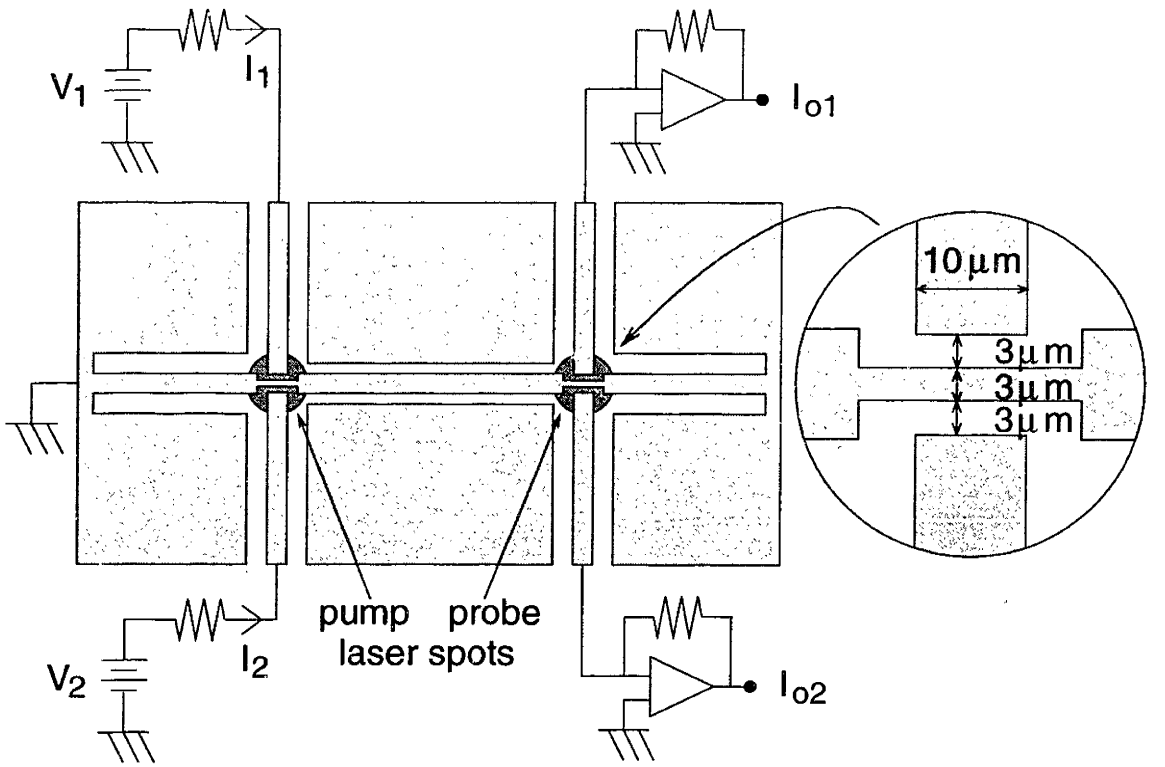

Figure 3-1: Schematic diagram of our coplanar waveguide circuit, with inset showing the two active regions of the probe photoconductor. The pump and probe regions are drawn to scale, though the entire circuit is not. V_1 and V_2 are voltage supplies for the pump photoconductor, and I_1 and I_2 are the supplied DC photocurrents (dark current is negligible). I_{o1} and I_{o2} are the DC outputs of the transimpedance amplifiers collecting the two probe currents. I_{o1} and I_{o2} depend on the time delay between the arrivals of the pump and probe laser pulses.

conductor. The active regions are 10-μm wide with 3-μm gaps, and are separated by the center conductor at a point where it narrows to 3 μm. They are close enough to be illuminated by the same laser spot, yet can be biased independently on the pump side, or collect independent samples on the probe side. Thus the type of mode generated at the pump can be adjusted by tuning V_1 and V_2 [76], and the even and odd modes can be distinguished by comparing the two probe currents.

Our circuit is "device-ready" in that a device could be embedded between the pump and probe spots in common-gate configuration without having to create any other discontinuity than the device itself. To embed a device, the center conductor of the coplanar waveguide must be split halfway between pump and probe and the

device placed in between. The portion of the center conductor connected to the pump then becomes the source contact, the portion connected to the probe becomes the drain contact, and the two ground planes become independent gate contacts. The dual-photoconductor design has two important capabilities: generation of a pure odd mode, and access to the source and drain. Previous designs had either one or the other capability [10, 75].

One disadvantage of dual photoconductors compared with a single photoconductor is the added loss in coupling between the photocurrent and the current excited in the propagating modes. We define the coupling constant $C(\omega)$ as

$$C(\omega) = \frac{I_{\text{prop}}(\omega)}{I_{\text{photo}}(\omega)}, \tag{3.1}$$

where $I_{\text{prop}}(\omega)$ is the Fourier transform of the transient current propagating in a quasi-TEM mode of the CPW, and $I_{\text{photo}}(\omega)$ is the Fourier transform of the transient photocurrent within the photoconductor. Loss is indicated by $|C(\omega)/C(\omega = 0)| < 1$. Figure 3-2 shows the magnitude of a few normalized coupling constants as a function of frequency, calculated with FD-TD electromagnetic simulation software freely available from Silicon Graphics Corp. [80] (See Appendix A). The least loss occurs when a single switch, a gap in the center conductor of a coplanar waveguide (see Fig. 2-19), excites the odd propagating mode. The small loss is due to radiation into the substrate and free space. More loss occurs when dual photoconductors are symmetrically biased to excite the odd mode. The dual photoconductors radiate more than an embedded photoconductor because they are not as well shielded by ground planes. Even greater loss occurs when dual photoconductors are anti-symmetrically biased to excite the even mode. This coupling rolls off at a lower frequency than the coupling from an symmetric excitation to the odd mode because, as explained in Sec. 3.1, the even mode has a greater width than the odd mode.

The circuits used in our experiments were fabricated on a 1-μm-thick layer of low-temperature-grown (LTG) GaAs grown by molecular beam epitaxy on a semi-insulating GaAs wafer at 250°C and annealed at 540°C for 10 minutes inside the

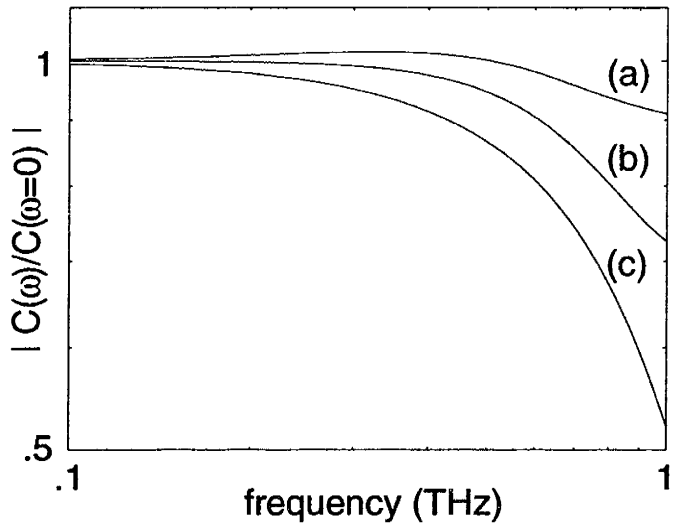

Figure 3-2: Magnitudes of photocurrent-to-propagating-mode-current coupling constants, each normalized to its DC value, calculated with an FD-TD electromagnetic simulator. (a): single photoconductor embedded in coplanar waveguide coupling to the odd mode. (b): dual photoconductors with symmetric excitation coupling to the odd mode. (c): dual photoconductors with asymmetric excitation coupling to the even mode. The rise in curve (a) above a value of 1 is an artifact of the FD-TD simulation.

MBE chamber in As-rich conditions. The wafer was fabricated by Dr. Förster of FZ Jülich. We measured the LTG GaAs to have a carrier lifetime of 1.2 ps with the autocorrelation technique discussed in Sec. 2.6. The circuits were defined by optical lithography and fabricated by liftoff of an evaporated 250-nm-thick Au film with a 50-nm-thick Ti adhesion layer. Each circuit has seven distinct sections of coplanar waveguide: the main one, which is a 2-mm-long straight line between pump and probe, and six parasitic ones, which contact the photoconductive switches. When the pump photoconductor is illuminated by an optical pulse, electrical pulses are generated on the nearby parasitic lines as well as on the main line. These pulses reflect at bonding pads or other terminations and then enter the main line, adding spurious peaks to the signal sampled at the probe. The parasitic lines therefore were made 1 mm long, enough for substantial temporal separation between the main peak and the spurious peaks. In most cases the main coplanar waveguide has a 10-μm-wide center conductor and a 5-μm gap between the center conductor and each ground

plane (characteristic impedance $Z_0 = 44\ \Omega$). A coplanar waveguide with the same Z_0, a 30-μm-wide center conductor and 15-μm gaps was found to have nearly the same transmission properties. The parasitic coplanar waveguides have 10-μm-wide center conductors and 10-μm gaps ($Z_0 = 55\ \Omega$).

3.3 Experimental results

3.3.1 Experimental set-up

We performed pulse-propagation experiments with our circuit as follows, with a technique called photoconductive sampling[1]. We used a mode-locked Ti:sapphire laser operating at a wavelength of 760 nm, emitting pulses of 100 fs width (as inferred from the spectral width) at a rate of 82 MHz. Its beam was split into pump and probe beams, which were focused onto their respective photoconductors. As shown in Fig. 3-1, the active regions of the pump photoconductor are biased, so each pump optical pulse generates an electrical pulse that propagates down the CPW towards the probe photoconductor. The electrical pulse provides a transient voltage bias to both active regions of the normally unbiased probe photoconductor. When this transient bias and the probe optical pulse arrive at the probe photoconductor simultaneously, photocurrents are generated in the two parasitic CPWs that contact the probe photoconductor. These currents propagate to the ends of the CPWs, where they are collected by transimpedance amplifiers (see Fig. 3-1). When the electrical transient and probe pulse are not simultaneous, no current is generated. In effect, the probe photoconductor samples the electrical transient on the main CPW, with a time resolution equal to the free carrier lifetime of the LTG GaAs. The output currents I_{o1} and I_{o2} depend on the time delay τ between the pump and probe optical pulses, and the traces $I_{o1}(\tau)$ and $I_{o2}(\tau)$ are equal to the convolution of the electrical transient at the probe photoconductor and the optical impulse response of the photoconductor. With an active device placed between pump and probe, other groups have used the photo-

[1]The first three subsections of experimental results were published in [81]. The rest are unpublished.

conductive sampling technique to measure the device's S-parameters [44]. We use it with an unbroken CPW between pump and probe to investigate pulse generation by our novel double photoconductor.

We focused both the pump and the probe laser beam onto our circuit at approximately normal incidence with a single 5x microscope objective. The spot diameters were approximately 12 μm. The average power in the pump beam was 8 mW and the power in the probe beam was 11 mW. The path length of the pump beam was controlled by a retroreflector mounted on a motor-driven translation stage, and the path length of the probe beam was dithered at 15 Hz by a retroreflector mounted on an audio speaker. The currents I_{o1} and I_{o2} were measured by low-noise transimpedance amplifiers whose outputs were displayed and averaged on a digital oscilloscope triggered at 15 Hz. The oscilloscope measured a portion of the traces $I_{o1}(\tau)$ and $I_{o2}(\tau)$ at one time. These measurements were averaged for 90 s. Because of the limited travel of the speaker, we moved the motor-driven translation stage to measure different portions of $I_{o1}(\tau)$ and $I_{o2}(\tau)$, then stitched the portions together to derive the full traces.

Alignment was achieved while monitoring the main peak of $I_{o1}(\tau)$ and $I_{o2}(\tau)$ in real time. For coarse alignment, we adjusted the x-y-z translation stage on which the sample was mounted. Fine alignment of the pump beam to the pump spot was accomplished by steering the pump beam to simultaneously equalize and maximize I_1 and I_2. We aligned the probe beam to the probe spot by steering the probe beam to simultaneously balance and maximize $I_{o1}(\tau)$ and $I_{o2}(\tau)$. Some iteration of these steps was performed, with minimal effect. Once lateral alignment was achieved, the translation stage was adjusted to place the circuit right at the microscope objective's focal plane. Biases were applied to the two active regions of the probe photoconductor to verify that the photogenerated currents were indeed approximately equal. We find our double photoconductors easier to align to than photoconductors with a single active region and power supply, such as a gap in the center conductor of a CPW. This is because the relative magnitude of the two currents I_1 and I_2 give information about where the pump beam spot is with respect to the pump photoconductor.

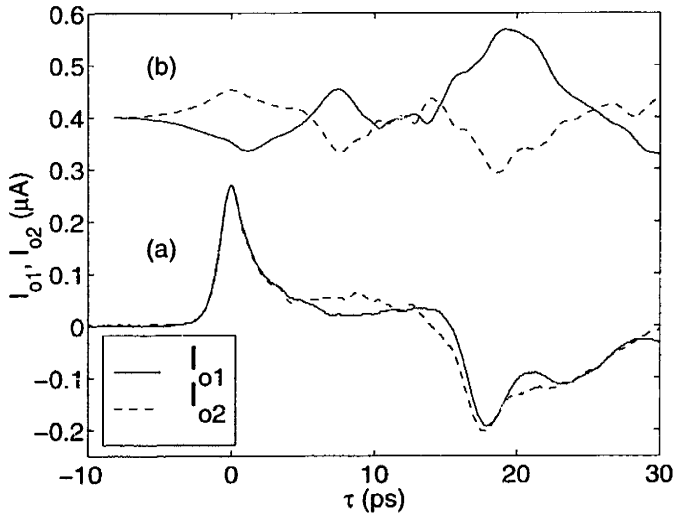

Figure 3-3: Measured electrical transients $I_{o1}(\tau)$ and $I_{o2}(\tau)$ under symmetric bias (a) and antisymmetric bias (b). (a): $V_1 = V_2 = 20$ V, $I_1 = I_2 = 8.0\ \mu$A, pulse width (FWHM) = 2.4 ps. (b): $V_1 = -20$ V, $V_2 = 20$ V, $I_1 = -14.4\ \mu$A, $I_2 = 14.8\ \mu$A (shifted by 0.4 μA).

3.3.2 Excitation of odd and even modes

Figure 3-3 shows the averaged traces for two different pump biases. Both traces were measured with the two active regions of the pump and probe switches equally illuminated. Trace (a) was measured with equal pump biases, and trace (b) was measured with equal pump biases of opposite sign. In trace (a), I_{o1} is nearly equal to I_{o2}, indicating that a pure odd mode was generated and received. In trace (b), I_{o1} and I_{o2} are approximately equal and of opposite sign, indicating that a pure even mode was generated and received. There is a portion of trace (a) for which I_{o1} and I_{o2} are significantly different at a time-delay of 10 ps. This is evidence that the even mode was received at the probe a substantial time after the arrival of the odd mode's main peak. The even mode was probably generated by stray radiation coupling to the main line after a pulse on a parasitic waveguide reflected from a bond wire. This is an example of how the mode-discriminating photoconductors can distinguish the main features of a signal from the spurious ones. The large negative peaks in both traces at 18 ps are due to reflections at the shorts that terminate the parasitic waveguides that contact the main center conductor. The 18 ps travel time for a round trip across 1

mm agrees with the theoretical value for the group velocity of a coplanar transmission line on a GaAs substrate, which is 0.11 mm/ps or $0.37c$ [10].

The main peaks of trace (a) are five times higher than the main peaks of trace (b), even though both I_1 and I_2 are higher with antisymmetric bias. This is because, as explained earlier, the odd mode attenuates and disperses less than the even mode does, and, as shown in figure 3-2, the coupling between a symmetric excitation and the odd mode is more efficient at high frequencies than the the coupling between an an asymmetric excitation and the even mode. There are multiple asymmetric features in trace (b) that do not appear in trace (a), such as as the large peak at 7 ps. This may due to the extra dispersion suffered by the even mode, or the radiation that escapes from an asymmetric excitation into free space or the substrate.

3.3.3 Compensation of pump-beam misalignment

The two contacts to the pump photoconductor can be used to generate a pure odd mode even when the two active regions of the pump are not equally illuminated. This is particularly useful with fiber-optic coupling since unavoidable fiber misalignment can be compensated [78]. Figure 3-4 shows an example of such compensation. Trace (a) was measured with a balanced illumination of the pump and probe switches, and equal pump biases. It shows that the propagating pulse was almost purely in the odd mode. Trace (b) was measured at the same bias, after the pump beam was slightly misaligned, as evidenced by the inequality of I_1 and I_2. This trace contains some asymmetric features that are visible in trace (b) of figure 3-3, such as the asymmetric peak at 7 ps. Obviously, this pulse contained both even and odd modes. Trace (c) was measured after V_1 and V_2 had been adjusted to equalize I_1 and I_2, without further adjustment of the pump beam. The original values of I_1 and I_2 could not be obtained, because that would have required a near-breakdown value of V_1. Trace (c) shows that mode purity was recovered, since trace (c) is approximately a scaled version of trace (a). Interdigitation of the two active regions of each photoconductor using electron beam lithography would have made the switches less sensitive to optical misalignment, and more responsive as well.

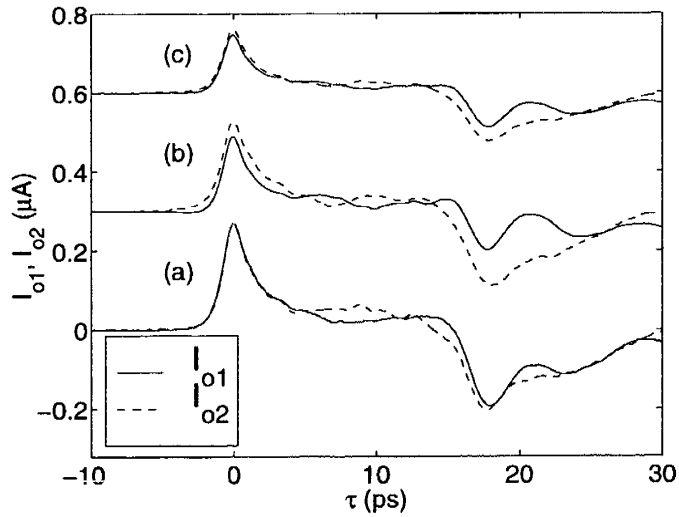

Figure 3-4: Effect of compensation of pump beam misalignment on $I_{o1}(\tau)$ and $I_{o2}(\tau)$. (a): pump and probe beams aligned, $V_1 = V_2 = 20$ V, $I_1 = I_2 = 8.0\ \mu$A (same as trace (a) of Fig. 3-3. (b): pump beam misaligned, $V_1 = V_2 = 20$ V, $I_1 = 1.9\ \mu$A, $I_2 = 11.3\,\mu$A (shifted by 0.3 μA). (c): pump beam still misaligned, $V_1 = 30$ V, $V_2 = 13$ V, $I_1 = I_2 = 5.0\ \mu$A (shifted by 0.6 μA).

3.3.4 Pulse propagation on a hybrid circuit

All the advantages of our novel circuit, as well as its large bandwidth, are maintained even when it is used in a hybrid experiment, in which the device to be tested is on a separate chip from the photoconductive switches. Thus S-parameter measurements with picosecond resolution can be done without monolithically integrating the device of interest with a fast photoconductor such as LTG GaAs. The device need only be embedded in a coplanar waveguide, which is a simple single layer of metal. We tested a hybrid circuit by first scribing then breaking a chip like the one shown in figure 1 in half vertically, creating a pump chip and a probe chip. The two pieces were then placed next to each other in a chip carrier, aligned using a microscope and translation stages, and fixed in place with silver epoxy. The corresponding parts of the main coplanar waveguide were then contacted by applying silver epoxy to the gap between those parts with a needle tip. The circuit used had a large main coplanar waveguide to make alignment and contact easier. The center conductor was 30-μm wide and there was a 15-μm gap between the center conductor and each ground plane. The needle tip left about a 10-μm-diameter spot of silver epoxy on the Ti/Au waveguide,

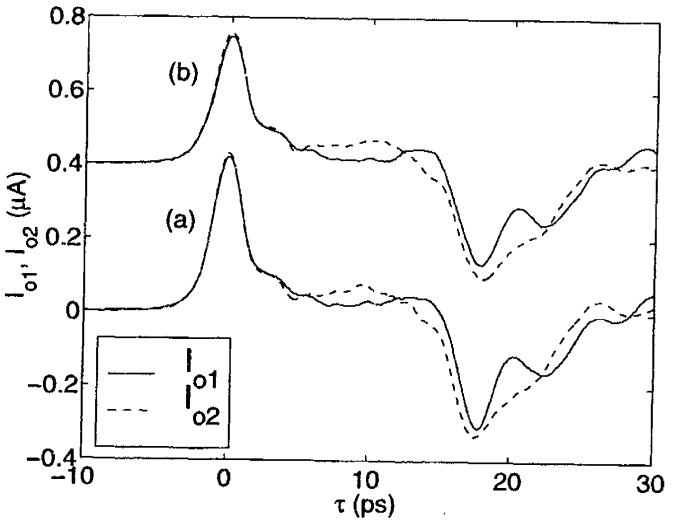

Figure 3-5: Measured electrical transients $I_{o1}(\tau)$ and $I_{o2}(\tau)$ on an integrated circuit (a) and on a hybrid circuit (b). (a): $V_1 = V_2 = 20$ V, $I_1 = I_2 = 9\ \mu$A, pulse width (FWHM) = 2.5 ps. (b): same bias and currents, pulse width (FWHM) = 2.6 ps, shifted by 0.4 μA.

and could be positioned with 1-μm precision, thus the shape of the applied epoxy matched the coplanar waveguide well. Figure 3-5 shows that trace (a), measured on an integrated circuit, is nearly identical to trace (b), measured on a hybrid circuit. The pulse width difference is only 4%.

3.3.5 Pulse generation by a normal photoconductor

We verified that the electrical pulse launched from our novel double photoconductor is almost identical to a pulse launched from a photoconductor with a single active region, a gap in the center conductor of a CPW. To do this, we fabricated the circuit shown in Fig. 3-6 on the same wafer of LTG GaAs as the experimental circuit described above. It has a single-gap photoconductor biased by V_1 in the spot of the pump laser beam, and a double photoconductor in the spot of the probe beam identical to that described earlier. The active region of the pump photoconductor has the same dimensions as the active regions of the double photoconductor: it's 3 μm long and 10 μm wide. The circuit was illuminated as described above, and the pump beam was aligned to the pump photoconductor simply by maximizing I_1.

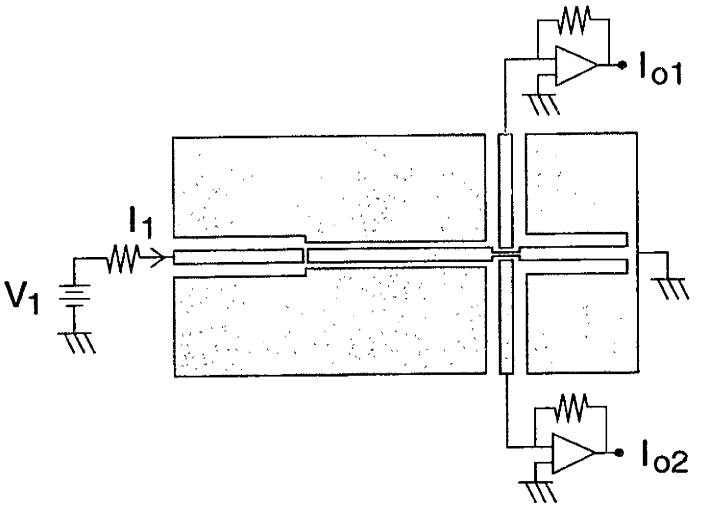

Figure 3-6: Schematic diagram of a coplanar waveguide circuit with a simple pump photoconductor with one active region, and a double probe photoconductor identical to the one of the circuit shown in Fig. 3-1. The pump and probe regions are drawn to scale though the entire circuit is not.

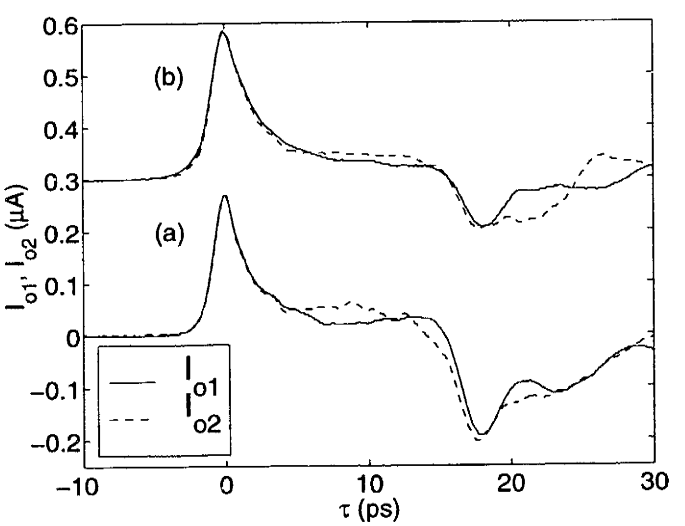

Figure 3-7: Comparison of electrical transients $I_{o1}(\tau)$ and $I_{o2}(\tau)$ measured (a) on the standard experimental circuit (same as trace (a) of Fig. 3-3) and (b) on the circuit shown in Fig. 3-6. $V_1 = 20$ V, $I_1 = 11.0\,\mu$A, pulse width (FWHM) = 2.9 ps (shifted by 0.3 μA).

Figure 3-7 shows the measured electrical transients generated by the single pump photoconductor, compared with the transients generated by a double photoconductor. The transients are on the whole very similar. The peak heights are almost equal, even though 31% less dc photocurrent flows through the single pump photoconductor than through the two active regions of the double photoconductor, because 45% of the transient current in the double photoconductor excites an electrical pulse that travels away from the probe and doesn't contribute to the main peak[2]. The main peak of the transient generated by the single photoconductor has a full temporal width at half maximum of 2.9 ps, compared with a 2.4-ps width for the main peak of the transient generated by the double photoconductor. We believe this difference is erroneous, because simulation indicates that the single photoconductor couples high-frequency transient photocurrents to the odd propagating mode better than the double photoconductor does (see Fig. 3-2). Much less of the spurious even mode is generated by the single photoconductor than by the double photoconductor, as evidenced by the near-equality of I_{o1} and I_{o2} for time delays less than 18 ps, which indicates that the single photoconductor is indeed better coupled to the odd propagating mode. Measurements of the temporal width of electrical transients on the standard experimental circuit on different occasions varied by about 0.5 ps, thus such an error is possible. This error is usually caused by incorrect estimation of the trajectory of the moving retroreflector that determines τ.

While the main peak heights of the two transients are almost the same, the heights of the negative peaks at a time delay of 18 ps are quite different. The negative peak of the transient generated by the single photoconductor is half the height of the other negative peak. In Sec. 3.3.2 we described how the negative peak in the transient generated in the standard experimental circuit corresponds to reflections at the shorts that terminate the two parasitic CPWs that contact the main center conductor. The circuit with a single pump photoconductor only has one short termination, which probably explains why its negative peak is small. The spurious pulse that propagates

[2]a smaller electrical pulse propagates away from the probe than towards it because the main CPW has a lesser characteristic impedance than the parasitic CPW that adjoins it has.

on the parasitic CPW that contacts the single photoconductor probably reflects poorly at the CPW's termination, which is a bonding pad, and does not reach the probe. There are too many spurious pulses that propagate over too many paths and encounter too many different terminations and discontinuities to draw firm conclusions from the negative peak at 18 ps of delay.

3.3.6 Pulse propagation through gate-lead discontinuities

We noted in Sec. 3.2 that our standard experimental circuit is "device-ready" in that a three-terminal device such as an FET could be easily and cleanly embedded in the main CPW between pump and probe to measure its impulse response. A three- or four-terminal device can be embedded without breaking the ground planes of the main CPW, because each ground plane can serve as a gate lead. The ground planes can provide dc bias without disturbing pulse generation and detection at the photoconductors because, as Fig. 3-1 shows, the LTG GaAs near the ground planes is not illuminated.

There are devices with more than two gates that we would like to measure the impulse response of, such as quantum dots and lateral resonant tunneling devices with as many as six gates. A two-level metal scheme could be used to bring the extra gate leads over the ground planes without breaking them, but that would entail extra processing that may damage the two-dimensional electron gas that is the key element of the devices mentioned above. The same holds true for air bridges. We performed pulse propagation experiments on circuits with the ground planes broken to form multiple gate leads to see if a single-level metallization can be used to measure four- and six-gate devices.

Figure 3-8 shows how the standard experimental circuit was altered to make circuits with double photoconductors at pump and probe and multiple gate leads. These circuits were also fabricated on the same LTG GaAs wafer described earlier. To make the four-gate circuit (circuit (a) of Fig. 3-8), the ground planes are broken by a 5-μm-wide gap. To make the six-gate circuit (circuit (b) of Fig. 3-8), the ground planes are broken by tapered CPWs. These have 3-μm-wide center conductors and

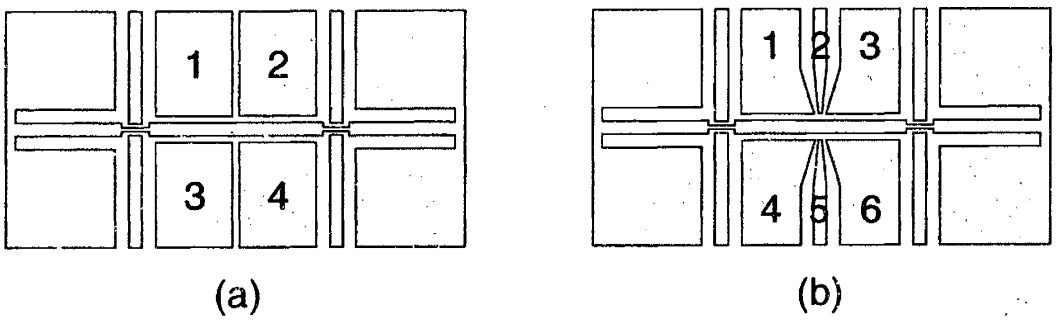

Figure 3-8: Schematic diagram of coplanar waveguide circuits identical to the one shown in Fig. 3-1, except that the ground planes of the main CPWs are broken to form multiple gate leads. Circuit (a) has four gate leads, which are numbered, and circuit (b) has six. The pump and probe regions and the regions where the gate leads approach the center conductors are drawn to scale, though the entire circuits are not

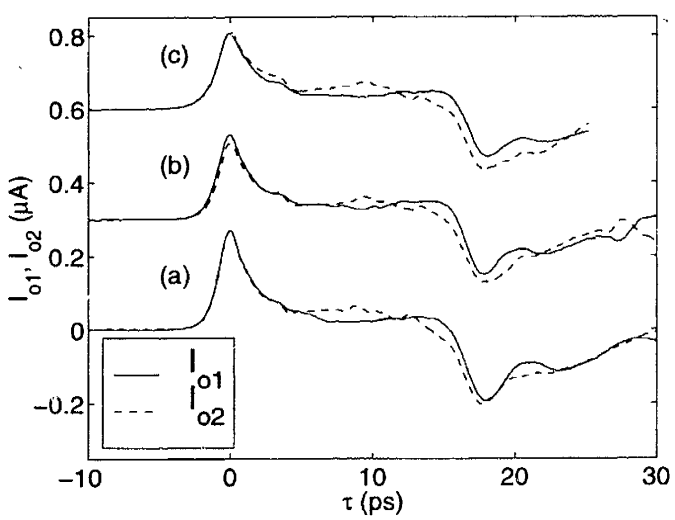

Figure 3-9: Comparison of electrical transients $I_{o1}(\tau)$ and $I_{o2}(\tau)$ measured (a) on the standard experimental circuit (same as trace (a) of Fig. 3-3); (b) on the four-gate circuit shown in Fig. 3-8 (a). $V_1 = V_2 = 20$ V, $I_1 = I_2 = 9.3\,\mu$A, pulse width (FWHM) = 2.5 ps (shifted by 0.3 μA); and (c) on the six-gate circuit shown in Fig. 3-8 (b). $V_1 = V_2 = 20$ V, $I_1 = 8.7\,\mu$A, $I_2 = 9.0\,\mu$A, pulse width (FWHM) = 3.0 ps (shifted by 0.6 μA).

3-μm-wide gaps where they meet the main CPW. These dimensions flare out to 10 μm over a 100 μm distance to reduce the chance of accidental shorts between gate leads. The center conductors of the main CPWs are unbroken, as on the standard experimental circuit, so that we observe the effect of the broken ground planes alone.

We performed pulse propagation experiments on these circuits exactly as described in Sec. 3.3.1. The measured electrical transients are shown in Fig. 3-8, where they are compared with the transient measured on the standard experimental circuit. Note that all the transients are mostly very similar, which means that four- and six-gate devices can be measured with a single level of metallization. The extra gates lower the amplitude of the main peak and broaden it, without introducing any extra features to the transient or mixing the even and odd propagating modes. The pulse-width broadening from 2.4 ps for the two-gate circuit to 3.0 ps for the six-gate circuit is not very severe, but would probably be more severe if the pulse generated by the pump photoconductor were shorter. Even though the coupling between the different parts of the broken ground planes is capacitive, the dc component of the propagating pulse is transmitted by the broken-ground-plane discontinuity. This is because the current propagating in the main CPW's unbroken center conductor induces charge in whatever ground plane is nearby, whether that ground plane is broken or not. This propagation behavior was verified with the FD-TD electromagnetic simulator discussed earlier.

There seems to be a secondary peak in the transients at a delay of 3 ps that is unaffected by the extra gates. It maintains its height as gates are added, even as the main peak height decreases. The origin of this peak is unknown.

3.4 Discussion

In this chapter a novel photoconductor and a coplanar waveguide circuit are introduced that make possible clean and accurate photoconductive sampling measurements and only require a single level of metallization. The photoconductor and circuit have the following capabilities which we prove experimentally: the novel photoconduc-

tor with two active regions can both selectively generate and detect the even and odd propagating modes of a CPW; the circuit has fewer discontinuities than other photoconductive-sampling circuits, and therefore few spurious features are observed in measured electrical transients; two circuits on separate samples can be connected with silver epoxy to make a hybrid circuit, without consequent loss of bandwidth; the double photoconductor generates the same electrical pulse that a simple photoconductor with a single active region does; and the circuit can contain as many as six gate leads without intolerable degradation of its transmission probabilities. The photoconductor and circuit should be useful for impulse-response measurements of active devices, especially at temperatures below 1 K, where the low heat load of fiber-coupled photoconductive sampling is a necessity [78]. The results discussed in this chapter should be of general interest to anyone designing ultrafast optoelectronic and electronic circuits, especially the results concerning coupling between circuit elements and the transmission characteristics of CPW discontinuities.

The design of our circuit can be improved for better impulse-response measurements. As shown in [73], the transmission characteristics of CPWs with narrow ground planes (10 μm to 50 μm) are better than those of standard CPW with very large ground planes ($>$ 500 μm), such as what we use. This is because the lateral extent of the odd propagating mode of a narrow-ground-plane CPW is smaller than that of a standard CPW. The odd mode of a narrow-ground-plane CPW has a fringing field far away from the metal conductors, but this quadrupole-like field is smaller than the field near the ground planes of a standard CPW, which are charged. As discussed in Sec. 3.1, the smaller a mode's lateral extent, the lower the radiative loss and dispersion. The width of the ground planes of our circuit could be reduced without any trade-off.

Another improvement would be the supression features in the measured electrical transient caused by spurious electrical pulses. These features corrupt the electrical transient's main peak, which is the feature that contains information about the impulse response of the device under test. While we can't completely eliminate spurious pulses, we can limit their influence by attenuating them or directing them away from

the probe photoconductor. For example, the height of the negative peak at 18 ps of delay can be reduced by changing the terminations of the parasitic CPWs that contact the center conductor of the main CPW from shorts to matched resistive loads. If broadband loads are not feasible, then the terminations might be horns that would launch spurious pulses into free space. We can make all the parasitic CPWs more attenuative by switching to a single-level, two-metal process: conductive Ti/Au for the main CPW, lossy bismuth [82] for the parasitic CPWs.

The experimental work in this chapter requires more verification by simulation than what we performed. It is quite difficult to do FD-TD electromagnetic simulation of our circuit because it is about 3 mm long and 1.5 mm wide and contains features as small as 3 μm. The computers we used cannot handle such a large, dense simulation, so it is difficult to tell if features in the simulated electrical transients are caused by circuit elements or the simulation boundaries. We can simulate the circuit elements one at a time and cascade the transmission characteristics of each element to simulate the whole circuit, but our photoconductive probe has a fixed position, so it is impossible to experimentally verify the simulated characteristics of the individual elements. Experiments with a movable probe, such as an electro-optic crystal or a fiber-mounted photoconductive probe [83], would be better for verifying electromagnetic simulation.

To better understand the coupling between the transient photocurrent and the propagating electromagnetic mode, we propose studying the dependence of the electrical transient on the pump pulse energy. As discussed in Sec. 2.6, at high pump pulse energy, when the transient resistance of the illuminated pump photoconductor is lower than the characteristic impedance of the CPWs the photoconductor is coupled to, the peak voltage of the generated electrical transient should saturate at a value near the bias voltage. It would be interesting to attempt to observe this saturation, to see if photoconductors and CPWs can really be treated as a network of resistors, or if Maxwell's equations and the electron transport equations must be solved simultaneously to model them more accurately.

Chapter 4

An On-chip Frequency-domain Submillimeter-wave Spectrometer

4.1 Introduction

The most prevalent form of spectroscopy involving photoconductors is time-domain spectroscopy[1]. Time-domain spectroscopy systems include a photoconductive emitter excited by a mode-locked laser, and a photoconductive sampler gated by the same laser (see Fig. 4-1a). The emitter and detector are coupled via free space or transmission lines. Free-space-coupled spectrometers are more widely used, simply because they don't require monolithic integration of the sample of interest with photoconductors. Time-domain photoconductive spectrometers are attractive because pulsed photoconductive emitters are a powerful broadband source of submillimeter waves ($\approx$ 10 nW average power [84]), photoconductive samplers are sensitive detectors with subpicosecond time resolution (a signal-to-noise ratio of 10^6 has been achieved with a 300 ms integration time [85]), and photoconductive samplers detect the electric field, which yields information about both the amplitude and phase of the transmission coefficient.

One of the major drawbacks of time-domain spectroscopy is poor frequency res-

[1]See [1] for a review of photoconductive time-domain spectroscopy.

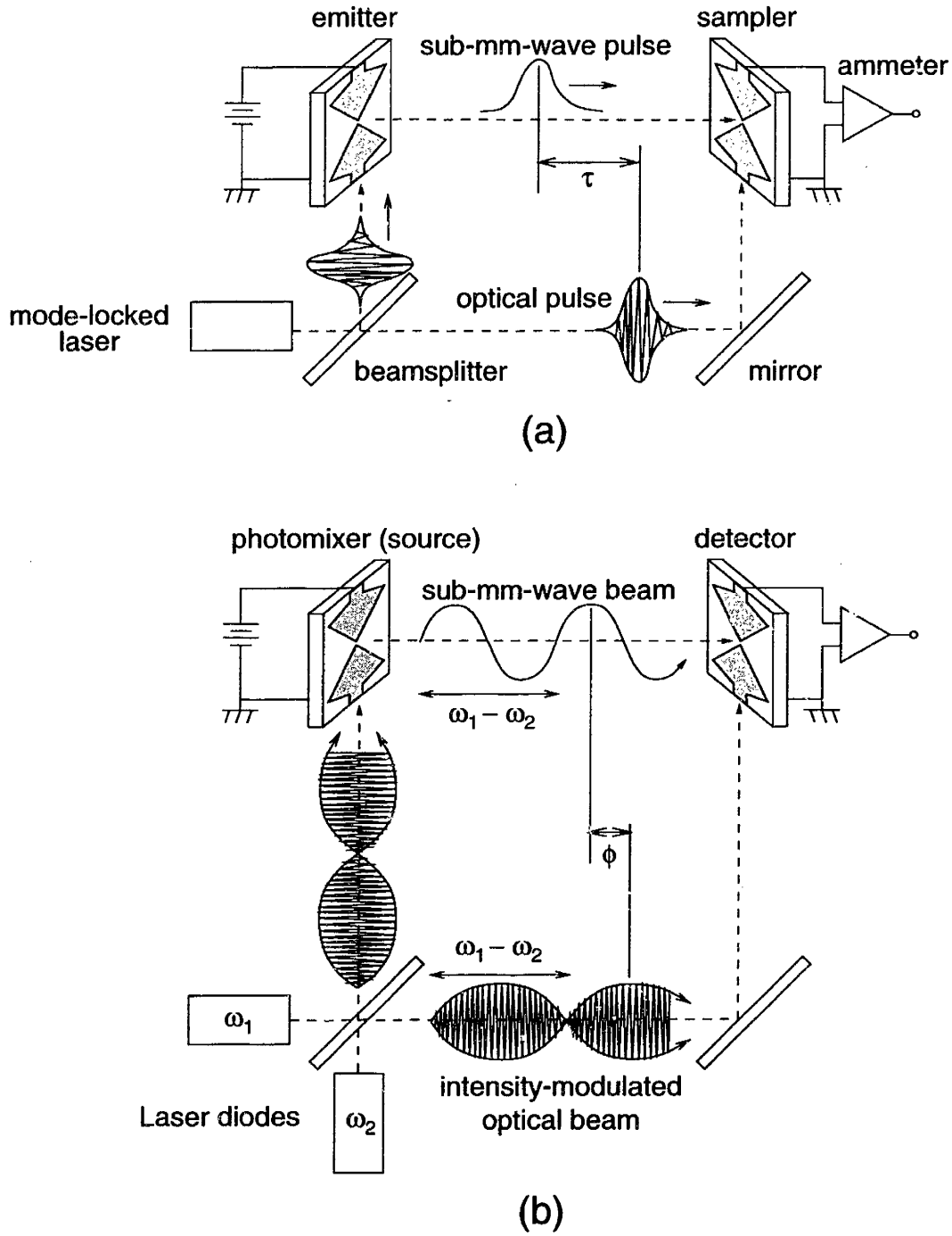

Figure 4-1: Time-domain (a) vs. frequency-domain (b) free-space-coupled photoconductive spectroscopy systems. The electric field $E(t)$ of the propagating waves is drawn. Each of the four chips shown contains an antenna-coupled photoconductor. Not shown are the optics used to collimate and focus the submillimeter waves, and the delay lines used to control the differences in path length between the two pairs of pump and probe optical beams. The path length difference controls τ, the time delay between pulses incident on the sampler in (a), and ϕ, the phase difference between the wave and intensity-modulated beam incident on the detector in (b).

olution. The frequency resolution is the inverse of the time span over which the transient electric field is measured. One fundamental limit on this time span is the period of the mode-locked laser, which usually corresponds to a frequency resolution of about 80 MHz. The time span is physically determined by the travel of the optical delay line. The travel is limited to about 1 m for reasons of compactness and stability, thus the frequency resolution is limited to about 150 MHz. In practice, the full travel of the delay line is never used, because spurious features in the measured electrical transient that are temporally separate from the main peak are windowed out of the experimental data. The typical time span used is 40 ps, which corresponds to a frequency resolution of 25 GHz. While this frequency resolution is sufficient for measuring the slowly-varying transmission spectra of materials, it may be insufficient for various applications for which submillimeter-wave spectroscopy has been proposed, especially the identification of chemical and biological substances.

Frequency-domain spectroscopy has inherently fine frequency resolution, but such spectroscopy is very difficult in the submillimeter-wave frequency range due to the lack of tunable sources of cw submillimeter-wave radiation. Recently the photomixer has been proposed as such a source. It is a voltage-biased, antenna-coupled photoconductor nearly identical to the photoconductive emitter used in time-domain spectroscopy, except that it is excited by the difference frequency of the two overlapping, tunable diode lasers that illuminate it [86]. The photomixer can generate about 0.1 μW of power at a difference frequency of 1 THz [8], and has been used successfuily as a source for molecular gas spectroscopy [87, 88]. The spectral linewidth of the photomixer's output is determined by the linewidths of the distributed-Bragg-reflector diode lasers that drive it, which are about 1 MHz when the lasers are stabilized [88]. The photomixer is tunable over an broad range (.2 to 3 THz [86]) because tuning the difference between the frequencies of two laser diodes by 1 THz entails tuning the wavelengths of those diodes by only marginal amounts.

While frequency-domain spectroscopy with a photomixer source and bolometric detector is useful for gas spectroscopy, it has the drawbacks that it is incoherent, involves cryogenics, and is not compact enough to make an on-chip spectrometer.

These drawbacks would all be removed if the detector were a photoconductor; in other words, if there were a frequency-domain analog of the time-domain spectrometer described at the beginning of this chapter. Verghese *et al.* [5] recently demonstrated the free-space-coupled version of just such a spectrometer (see Fig. 4-1b). Its source is a photomixer, and its detector is another antenna-coupled photoconductor, illuminated by a delayed portion of the two overlapping laser beams that illuminate the source. Just like the photoconductive sampler of the time-domain spectrometer, this detector is grounded at dc, and a dc current is generated within it by the coincidence of photogenerated carriers and an electromagnetic wave. This output current is at dc because the frequency of the electromagnetic wave and the modulation frequency of the photogenerated carriers are the same (since the carriers are generated by the same intensity-modulated light that excites the photomixer). The output current obviously depends on the phase difference between its optical and submillimeter-wave inputs, therefore the submillimeter wave is detected coherently. Essentially, the optical beam performs homodyne detection of the submillimeter wave at the photoconductive detector. Verghese *et al.* [5] also demonstrated a version of their spectrometer for microwave frequencies (.1 GHz to 27 GHz) coupled with coaxial lines.

In this chapter we demonstrate the monolithically integrated version of Verghese's spectrometer. Such a spectrometer is attractive for chemical and biological sensing applications because it has the frequency resolution these types of sensing require, it is compact and inexpensive, and it can be part of a microfluidic, "lab on a chip"-type circuit. It has the advantages over Verghese's free-space spectrometer that it can be used to test microelectronic devices, and does not require collimation and focusing of submillimeter waves. Not only is the spectrometer chip itself small, but the diode lasers that activate it are much smaller and cheaper than the Ti:sapphire mode-locked lasers used for time-domain spectroscopy. Because of the similarity between time-domain and frequency-domain photoconductive spectrometers, we were able to use the same devices described in the last chapter, with which we sampled picosecond-duration electrical pulses, for homodyne detection of continuous waves.

4.2 Experimental set-up and techniques

The circuit used for this experiment is the same coplanar waveguide circuit with embedded photoconductors shown in Fig. 3-1 and described in Sec. 3.2. It was connected to the same voltage biases and transimpedance amplifiers as shown in Fig. 3-1. It was illuminated as described below.

Beams from two distributed-Bragg-reflector laser diodes of slightly different wavelength (near 850 nm) were collimated with microscope objectives located near the diode apertures, forming elliptical beams approximately 2 mm wide and 4 mm tall. Two intensity-modulated optical beams were created by combining the two laser beams with a beamsplitter such that the each pair of beams output in the same direction was collinear (see Fig. 4-1b). Collinearity was achieved by simultaneously optimizing the coupling of each output laser beam to a single-mode optical fiber. Such coupling is very sensitive to a beam's position and angle.

The intensity modulation is due simply to the beating of the two laser frequencies. The intensity oscillates at the difference frequency, which we label f_d. Each laser's wavelength is temperature-tunable to a small extent that allows f_d to be tuned over a 1.5-THz range. With the room-temperature wavelengths of our lasers chosen appropriately, our difference-frequency tuning range was from dc to 3 THz. The difference frequency was measured by diverting a fraction of one of the intensity-modulated beams with a glass slide to a wavemeter, with which each laser frequency was measured individually by blocking one laser at a time. The wavemeter has 0.3 GHz resolution, which was sufficient for our work, since we never varied f_d by less than 5 GHz, between 20 GHz and 1 THz. The resolution with which we scanned our difference-frequency range is coarse enough that laser frequency instabilities due to temperature fluctuations, with a magnitude of about 50 MHz [86], was not observed. Each intensity-modulated beam traveled through an optical isolator placed immediately after the beamsplitter to reduce laser mode-hopping due to optical feedback.

The intensity-modulated beams function much as the pump and probe beams of the time-domain experiments discussed in the last chapter do. As such, the optics that

couple the intensity-modulated beams to our circuit are identical to the coupling optics discussed there. A retroreflector mounted on a motor-driven, computer-controlled translation stage controls the path length of the pump intensity-modulated beam, and a speaker-mounted retroreflector dithers the path length of the probe intensity-modulated beam. The pump and probe beams were focused onto their respective photoconductors on our circuit at approximately normal incidence with a single 10x microscope objective.

The aim of a time-domain experiment is to measure the output dc currents I_{o1} and I_{o2} as functions of the time delay τ. We control τ by controlling the path lengths of the pump and probe beams. τ is equal to $(z_{\text{probe}} - z_{\text{pump}})/c$, where c is the speed of light and z_{probe} and z_{pump} are the path lengths of the probe and pump beams, respectively (see Fig. 4-1a). z_{pump} includes the electrical length of the 2 mm of coplanar waveguide between the pump and probe photoconductors. The aim of a frequency-domain experiments is similar: to measure I_{o1} and I_{o2} at a given f_d as functions of the phase delay ϕ. We control ϕ exactly as described above, and ϕ is equal to $2\pi f_d(z_{\text{probe}} - z_{\text{pump}})/c$ (see Fig. 4-1b). The fact that we describe the path-length difference as a phase is because we expect I_{o1} and I_{o2} to vary sinusoidally with ϕ, because of the homodyne detection performed at the probe photoconductor. We describe this dependence as

$$I_{o1}(\phi), I_{o2}(\phi) = \text{Re}(I_0 e^{j\phi}) = |I_0| \cos(\phi + \delta), \tag{4.1}$$

where I_0 is a complex amplitude with phase δ. The angle δ may be non-zero because the material or device under test between the pump and probe photoconductors may induce phase shifts.

Just as we observed the electrical transients $I_{o1}(\tau)$ and $I_{o2}(\tau)$ of the time-domain experiment in real time by monitoring them on an oscilloscope triggered by the speaker drive, we tried to observe $I_{o1}(\phi)$ and $I_{o2}(\phi)$ in real-time with the same technique. With a speaker throw much greater than λ, the wavelength corresponding to f_d, we should see two in-phase sinusoids on the oscilloscope. Unfortunately, the ϕ-

dependent parts of I_{o1} and I_{o2} are too weak for the sinusoids to be observed this way. To measure the amplitude and phase of each sinusoid, we had to do separate measurements (described below) at a number of discrete ϕ determined by the motor-driven translation stage. For this reason we could not align the pump and probe beams to maximize $I_{o1}(\phi)$ and $I_{o2}(\phi)$, just as we performed alignment for the time-domain experiments while observing $I_{o1}(\tau)$ and $I_{o2}(\tau)$. Instead, we aligned the pump beam by maximizing and equalizing the currents I_1 and I_2. Next we aligned the probe beam by switching the bias network so that the probe photoconductor was biased, then maximizing and equalizing the new currents I_1 and I_2. The x-y-z translation stage holding the circuit was adjusted for coarse alignment, and beam steering was used for fine alignment.

In general, the ϕ-independent parts of I_{o1} and I_{o2} are much larger than the ϕ-dependent parts (the parts generated by the submillimeter wave excited at the pump), even though the probe photoconductor is nominally unbiased. This is because the probe photoconductor has some photovoltaic response, and because some of the pump bias appears across the probe photoconductor because of resistive coupling by the semi-insulating LTG GaAs substrate. The ϕ-independent parts of I_{o1} and I_{o2} make it very difficult to measure the ϕ-dependent parts by chopping either the pump or probe beam and measuring I_{o1} and I_{o2} with a lock-in amplifier at a set of discrete ϕ. Instead we used a technique similar to the phase modulation used with Fourier-transform spectrometers. We did not chop either beam, but instead dithered ϕ with the speaker over a range *less* than 2π (the speaker throw was less than λ), and lock-in detected the speaker-induced changes in I_{o1} and I_{o2}, essentially measuring the derivatives of $I_{o1}(\phi)$ and $I_{o2}(\phi)$. We performed this measurement at about ten discrete ϕ per wavelength of the sinusoid whose amplitude and phase we wanted to measure.

While our phase-modulation-type measurement technique gives us the best possible signal-to-noise ratio, its one drawback is that it's difficult to find the exact trajectory of the speaker at a given drive, and therefore difficult to extract the exact amplitudes of the sinusoids $I_{o1}(\phi)$ and $I_{o2}(\phi)$ from their measured derivatives.

The way around this is to measure the derivatives at different speaker-drive amplitudes, and compare them to their expected variations. The expected dependence of the derivative signals $I_{\mathrm{LIA1}}(\phi)$ and $I_{\mathrm{LIA2}}(\phi)$ measured by the lock-in amplifier on the amplitude of the speaker drive is calculated as follows. Assume that the speaker oscillates sinusoidally with a position x given by $\frac{s_0}{2}\cos(\omega t) + x_0$, where s_0 is the full speaker throw, which can be estimated by eye, and x_0 is the mean position, which corresponds to a phase delay ϕ. The current $I_{o1}(x)$ ($I_{o2}(x)$ will behave identically) is equal to $I_{o1}(\phi')$, where ϕ' is the instantaneous phase delay corresponding to x.

$$I_{o1}(x) = I_{o1}(\phi') = |I_0|\cos(\phi' + \delta) = |I_0|\cos(2 \times 2\pi(x - x_0)/\lambda + \phi + \delta), \qquad (4.2)$$

where I_0, as mentioned earlier, is the complex amplitude of the sinusoid we want to measure, δ is the phase of I_0, and the extra factor of two in the argument of sine comes from the fact that light hitting the speaker-mounted retroreflector makes a round trip over the retroreflector displacement. As a function of time,

$$I_{o1}(t) = |I_0|\cos(2\pi s_0 \cos(\omega t)/\lambda + \phi + \delta). \qquad (4.3)$$

The output of the lock-in amplifier is the time average of $I_{o1}(t) \times \cos(\omega t)$. This average is

$$I_{\mathrm{LIA1}}(\phi) = -|I_0| J_1(2\pi s_0/\lambda)\sin(\phi + \delta), \qquad (4.4)$$

where J_1 is the Bessel function of the first kind, of first order. As we would expect, $I_{\mathrm{LIA1}}(\phi)$ is a sinusoid, and is 90° out of phase with $I_{o1}(\phi)$, since $I_{\mathrm{LIA1}}(\phi)$ is essentially the derivative of $I_{o1}(\phi)$. We plot the amplitude of $I_{\mathrm{LIA1}}(\phi)$ as a function of s_0/λ in Fig. 4-2 for reference. The optimum full speaker throw is 0.29λ, at which the amplitude is a maximum of $0.58|I_0|$. Obviously the speaker drive must be tuned during a scan over a range of difference frequencies to keep the signal-to-noise ratio optimum. For each scan, we found the amplitude of the sinusoidal speaker drive that maximized the amplitude of $I_{\mathrm{LIA1}}(\phi)$ at the first frequency, and assumed we had achieved the optimum $s_0 = 0.29\lambda$. We then assumed that s_0 is proportional to the

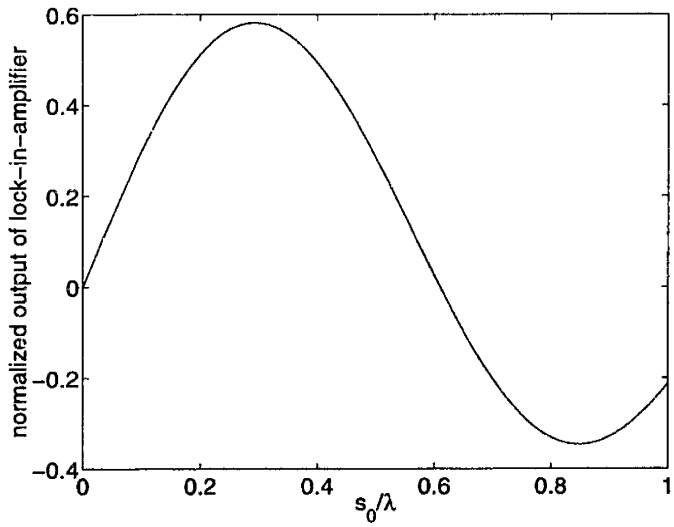

Figure 4-2: Calculated output of the lock-in amplifier, normalized by $|I_0|$, as a function of the normalized speaker throw, s_0/λ.

speaker-drive amplitude, and kept that amplitude proportional to λ during the scan. There is a limit to how hard we can drive the speaker, so at high λ we kept the speaker-drive constant and used Fig. 4-2 to derive $|I_0|$ appropriately for sub-optimum s_0.

4.3 Experimental results

4.3.1 Excitation and detection of the odd propagating mode

We first sought to verify that symmetric bias of V_1 and V_2, along with symmetric illumination of the pump and probe photoconductors by the two intensity-modulated beams, excites the odd propagating mode in our coplanar waveguide (CPW) circuit, as evidenced by symmetric detected currents $I_{\mathrm{LIA1}}(\phi)$ and $I_{\mathrm{LIA2}}(\phi)$. Fig. 4-3 shows I_{LIA1} and I_{LIA2} as functions of z, the position of the retroreflector mounted on the motor-driven translation stage, with which we control ϕ. The pump photoconductor was symmetrically biased with $V_1 = V_2 = 30$ V, and the difference frequency was 316 GHz, corresponding to $\lambda = 0.95$ mm. Note that I_{LIA1} and I_{LIA2} are sinusoidally dependent on z with a phase ϕ equal to $4\pi z/\lambda$, as expected. The sinusoidal parts

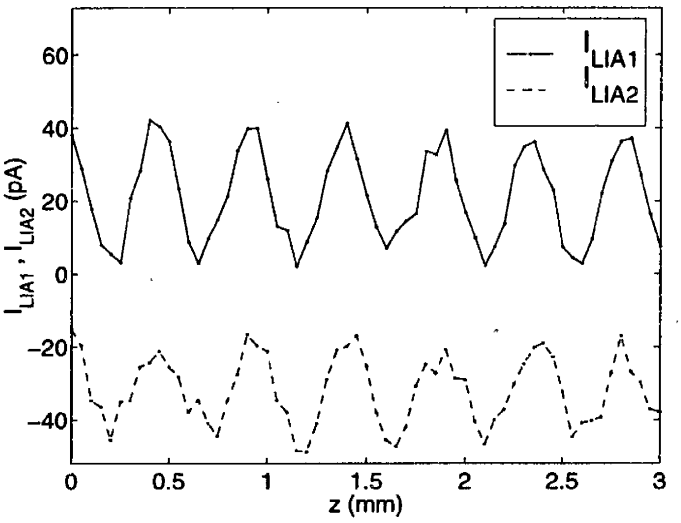

Figure 4-3: Outputs of lock-in amplifier I_{LIA1} and I_{LIA2} as functions of z, the position of the retroreflector mounted on the motor-driven translation stage. $V_1 = V_2 = 30$ V, $\lambda = 0.95$ mm.

of I_{LIA1} and I_{LIA2} are in phase and have approximately equal magnitude, indicating that a purely odd propagating mode was generated. For the rest of this chapter, we will concentrate on the dependence of I_{LIA1} on the difference frequency, and assume I_{LIA1} and I_{LIA2} are equal.

The background levels of I_{LIA1} and I_{LIA2} may be caused by coupling of the speaker-drive current to the contacts to the probe photoconductor, or may be caused by modulation of illumination of the pump photoconductor at the speaker frequency due to pump beam steering by the speaker-mounted retroreflector. While we tried to reduce the speaker-drive coupling by shielding and distancing the speaker-drive electronics from the measurement electronics, we perhaps could have reduced the pump beam steering by mounting the speaker horizontally instead of vertically, to reduce retroreflector wobble caused by gravity.

4.3.2 Transmission spectrum of the spectrometer circuit

The transmission spectrum of the spectrometer circuit is the function $I_0(f_d)$, where I_0 is defined in Eq. 4.1 and f_d is the difference frequency. We find $|I_0|$ at a given λ by measuring the amplitude of the sinusoidal variation of I_{LIA1} with z, and dividing

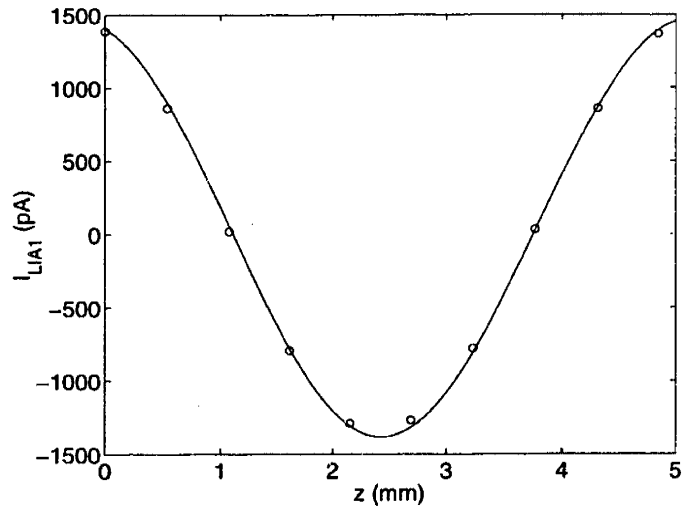

Figure 4-4: Typical data used to find $I_0(f_d)$. Data are shown as symbols, and are well fit by the sinusoid shown. The difference frequency was 27.9 GHz, in agreement with the sinusoid's 5.4 mm period.

this by $J_1(2\pi s_o/\lambda)$, as shown in Eq. 4.4. Typical data with which we performed this extraction are shown in Fig. 4-4. In general the amplitude spectrum of I_0 is flat at low f_d, rolls off at high f_d due to the finite response time of the pump and probe photoconductors, and contains peaks and valleys due to resonances of the spectrometer circuit.

As shown in Eq. 4.1, the phase δ of I_0 is the phase of $I_{o1}(\phi)$ at $\phi = 0$ (at zero path difference between the pump and probe beams). Though the effective path length of the 2 mm of CPW between the pump and probe photoconductors is frequency-dependent, as evidenced by the pulse dispersion discussed in Sec. 3.1, we will treat the path lengths as independent of f_d, and measure the frequency-dependent phase velocity of our CPW by measuring $\delta(f_d)$. Variation in $\delta(f_d)$ is caused by phase velocity dispersion, as well as reflections in the CPW circuit and phase-delay between the intensity modulated beams and the photocurrents they generate.

There is some ambiguity in extracting $\delta(f_d)$ from measurements of $I_{\mathrm{LIA1}}(z)$ made at a set of f_d. The main source of ambiguity is that z_{zpd}, the z that corresponds to $\phi = 0$, is unknown. The other source is that the sign of $I_{\mathrm{LIA1}}(z)$ is arbitrary, because it is determined by the phase of the lock-in amplifier. This makes the phases δ and $\delta + \pi$ indistinguishable. The measured data themselves have a well-defined phase, as

Fig. 4-4 shows, and are therefore not a major source of phase ambiguity. We settle the ambiguities by extracting phase spectra $\delta(f_d)$ from the measured data with assumed values for $z_{\rm zpd}$ and the sign of $I_{\rm LIA1}(z)$. We choose values that make the extracted $\delta(f_d)$ similar to the expected phase spectrum. The more frequencies at which we measure, and the greater the spread of the frequencies, the more confident we can be of our choices. Unfortunately the unknown $z_{\rm zpd}$ is a continuous variable, so there is a finite range of $z_{\rm zpd}$ that leads to acceptable $\delta(f_d)$. Thus we can find $\delta(f_d)$ with relative precision but not absolute precision.

While it does not cause ambiguity, one must remember to account for the $\pi/2$ phase difference between the measured $I_{\rm LIA1}(z)$ and the more fundamental $I_{o1}(z)$ when extracting $\delta(f_d)$ from measured data.

As noted in Sec. 4.2, poor signal-to-noise ratio is a problem with our frequency-domain measurements, so we made a few improvements to our experimental setup when measuring our circuit's transmission spectrum. One improvement was to connect the ground planes of the main CPW to ground. As Fig. 3-1 shows, these ground planes are normally left floating, to decrease the undesired current flowing through the power supplies of the pump photoconductor that doesn't flow through the photoconductor's two active regions and excite a submillimeter wave. However, grounding these ground planes shorts out a parasitic current path between the pump and probe, and reduces the noise in I_{o1} and I_{o2}.

To reduce the noise input to the lock-in amplifier, we ac coupled the trans-impedance amplifier with output I_{o1} to the lock-in amplifier with a 10 nF capacitor ($RC = 1$ s), which passed the speaker oscillation frequency (24 Hz) but rejected the dc, ϕ-independent component of I_{o1}. This was in addition to filtering performed by the lock-in amplifier, and was deemed necessary because the dc current is very large.

When we measured the transmission spectrum, we assumed that we were exciting only the odd propagating mode at the pump, and therefore did not compare I_{LIA1} with I_{LIA2} to check mode quality. We desired to combine the output currents of the two active regions of the probe photoconductor, so as to increase the signal measured by our lone lock-in amplifier. We tried to input the leads of the two active regions to

the same transimpedance amplifier, but this added a lot of noise, probably because the transimpedance amplifier was off-chip in a bias box, and connecting the two leads created a large loop. We could have connected the two leads on-chip, but this would have required rewiring the chip carrier, which we weren't able to do.

A simple solution was aim the probe beam at the photoconductor active region connected to the one transimpedance amplifier we measured, instead of illuminating the two active regions equally. Asymmetric illumination does not cause mode impurity, even though the probe photoconductor obviously interacts with on-chip submillimeter waves, because the resistance of the illuminated active regions (about 1 MΩ) is much greater than the characteristic impedance of the CPW (44 Ω). Thus an odd wave on the main CPW incident on the probe photoconductor is mainly reflected or transmitted to the parasitic CPW on the opposite side of the probe photoconductor, and the illuminated active regions are an insignificant probe of the ac voltage on the main CPW.

We performed our measurement of the transmission spectrum as follows. 63.7 mW of optical power was incident on the pump photoconductor, and 38.7 mW was incident on the probe photoconductor. At 22 discrete difference frequencies measured with the optical wavemeter, we measured one period of the sinusoid $I_{\mathrm{LIA1}}(z)$ at 10 evenly-spaced, discrete z. Each scan over z lasted about 4 minutes. The integration time of the lock-in amplifier was 3 s. Between each movement of the motor-driven retroreflector and measurement of I_{LIA1}, there was a 15 s wait. Prior to every scan, z was adjusted such that I_{LIA1} was near a maximum, then the pump and probe beams were steered to maximize I_{LIA1}. Once all the data were measured, the discrete Fourier transform of each scan was taken to find the amplitude and phase of the main harmonic. $|I_0|$ and δ were derived from these quantities as described above, taking into account the fact that each scan started at a different z.

Figure 4-5 shows the amplitude and phase of the measured transmission spectrum, in the difference frequency range of 21.3 GHz to 689 GHz. Its most prominent features are the peaks, valleys and high-frequency roll-off of the amplitude spectrum, and oscillations and non-zero average of the phase spectrum. The peaks, valleys and

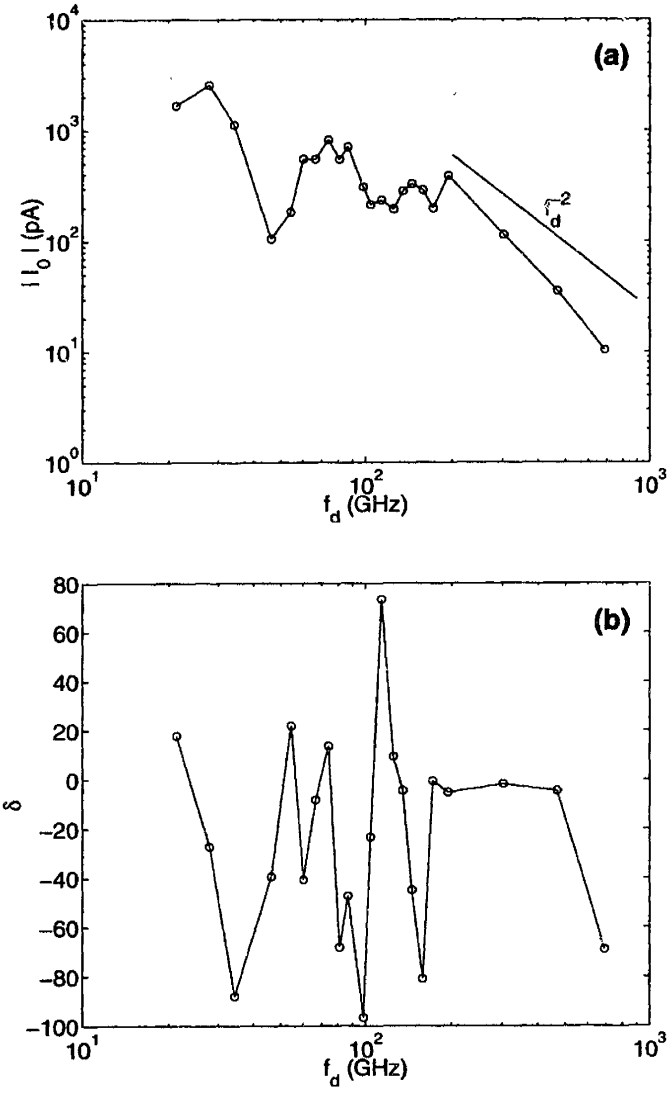

Figure 4-5: Amplitude (a) and phase (b) of the transmission spectrum. A f_d^{-2} roll-off is shown for comparison in (a). For all f_d, $V_1 = V_2 = 30$ V, $I_1 = I_2 = 53$ μA.

oscillating phase indicate that our CPW circuit has reflective terminations that cause resonance. This is undesirable for a spectrometer, but comes as no surprise, since reflections cause prominent features in the electrical transients shown in the last chapter. The finite peak-to-valley ratio that decreases with increasing frequency indicates that our CPWs are lossy, and that the loss increases with frequency. This is in agreement with previous measurements of the attenuation coefficient of CPWs, which increases with frequency due to the skin effect and radiative loss [73]. The amplitude at high frequency is nearly proportional to f_d^{-2}, which is the expected roll-off caused by the finite response time of the pump and probe photoconductors. We don't expect to observe an additional roll-off due to capacitance, because our photoconductors are planar and not interdigitated. The finite negative average phase is probably the consequence of the pump and probe photoconductors having different response times. If the pump photoconductor's response time were τ_{pump} and that of the probe were τ_{probe}, with $\tau_{\text{pump}} > \tau_{\text{probe}}$, then in the frequency range $\frac{1}{2\pi\tau_{\text{pump}}} < f_d < \frac{1}{2\pi\tau_{\text{probe}}}$ the pump photocurrent would lag the intensity modulation of the pump beam, but the probe photoconductance would be in phase with the intensity modulation of the probe beam, and we would observe a negative δ over the entire frequency range. The high τ_{pump} at our 30 V bias could be caused by the high-field effects discussed in Chapter 2.

We developed the following model for the transmission spectrum $I_0(f_d)$. It is based on the submillimeter-wave circuit diagram shown in Fig. 4-6, which in turn is based on the physical layout of the circuit, shown in Fig. 3-1. The 2-mm-long main CPW is represented by a transmission line with $Z_0 = 44\ \Omega$. The 1-mm-long parasitic CPWs that couple well to the main CPW and cause the large reflection seen in the time-domain experiments are represented by transmission lines with $Z_0 = 55\ \Omega$. The two active regions of the pump photoconductor are represented by in-phase current sources, each with a sinusoidal component oscillating at $\omega = 2\pi f_d$ and a dc component. The dc offset exists because the bias on the pump photoconductor is always positive. We assume that the ac and dc components have the same amplitude at $\omega = 0$, which is equivalent to assuming that the two laser diode beams

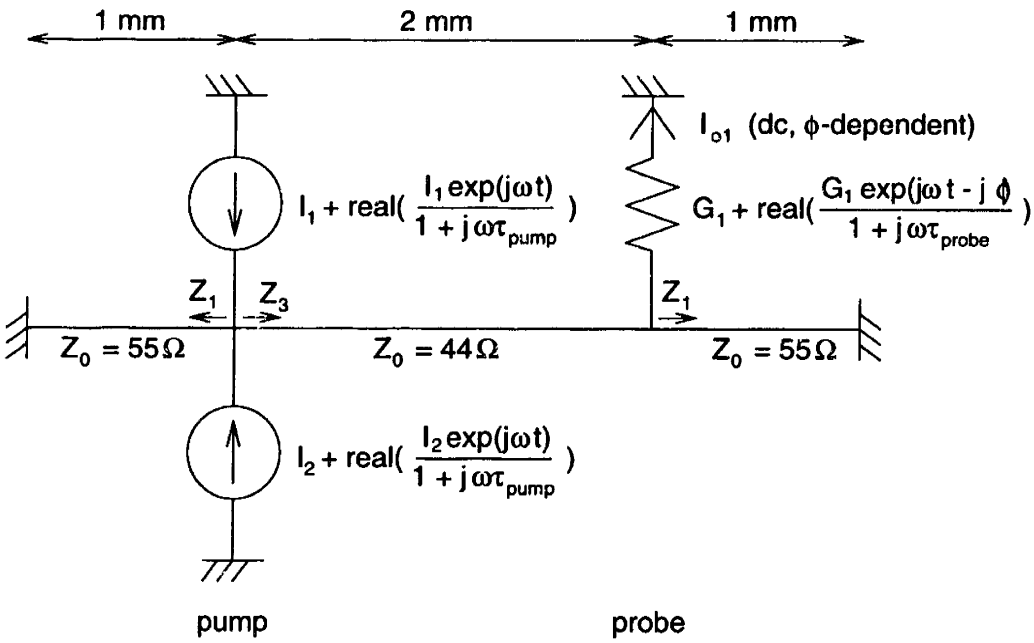

Figure 4-6: Circuit diagram of spectrometer. I_1, I_2 and G_1 are real numbers, and $\omega = 2\pi f_d$.

were perfectly overlapped, and that full intensity modulation of the pump and probe beams was achieved. The ac component has a frequency-dependent amplitude and phase because of the finite response time of the pump photoconductor. I_1 and I_2 are equal because the pump photoconductor was always evenly illuminated. The probe photoconductor is represented by a resistive tap of the CPWs with a time-dependent conductance proportional to the time-dependent current sources, but lagging them by the phase delay ϕ. There is only one resistor at the probe because of our single-sided illumination of the probe photoconductor. I_{o1} is the portion of interest of the current flowing through the probe photoconductor: the dc, ϕ-dependent portion. Z_1 and Z_3 are the input impedances at the points shown in the diagram.

We use standard microwave circuit analysis to find I_{o1} as a function of I_1, G_1, ϕ and f_d. We neglect the dc components of the current sources and the probe conductance, because these cause only ϕ-independent output current. We assume the CPWs have a propagation constant $\gamma = \alpha(f_d) + j\beta(f_d)$, where $\alpha(f_d)$ is the attenuation constant to be fit to the data, and $\beta(f_d)$ is the phase constant, which is equal to $2\pi f_d/v_p$, where v_p is the phase velocity of a coplanar transmission line on a semi-infinite GaAs

substrate. We neglect dispersion and consider v_p to be the frequency-independent value $0.37c$, or $1.1\text{x}10^8$ m/s [10]. First we find the input impedances Z_1 and Z_3.

$$Z_1 = 55 \tanh(\gamma \times .001) \ \Omega, \tag{4.5}$$

and

$$Z_3 = 44 \frac{Z_1 + 44 \tanh(\gamma \times .002)}{44 + Z_1 \tanh(\gamma \times .002)} \ \Omega. \tag{4.6}$$

Let V_{pump} be the complex amplitude of the ac voltage at the probe photoconductor. Then

$$V_{\text{pump}} = 2I_1(Z_1 \parallel Z_3)/(1 + j\omega\tau_{\text{pump}}). \tag{4.7}$$

V_{pump} is the sum of forward- and backward-moving waves on the main CPW, which we state as

$$V_{\text{pump}} = V_f \exp(\gamma \times .002) + V_r \exp(-\gamma \times .002) = V_f(\exp(\gamma \times .002) + \Gamma \exp(-\gamma \times .002)), \tag{4.8}$$

where V_f and V_r are the complex amplitudes of the forward and backward waves at the probe photoconductor, and Γ is the voltage reflection coefficient corresponding to the load Z_1 on the main CPW, and equals $(Z_1 - 44)/(Z_1 + 44)$. Let V_{probe} be the complex amplitude of the ac voltage at the probe photoconductor. Then

$$V_{\text{probe}} = V_f(1 + \Gamma) = V_{\text{pump}}(1 + \Gamma)/(\exp(\gamma \times .002) + \Gamma \exp(-\gamma \times .002)). \tag{4.9}$$

I_{o1} is the average over time of the product of the real parts of $V_{\text{probe}} \exp(j\omega t)$ and $G_1 \exp(j\omega t - j\phi)/(1 + j\omega\tau_{\text{probe}})$. This is equal to

$$I_{o1} = \frac{1}{2}|V_{\text{probe}}| \frac{G_1}{\sqrt{1 + \omega^2\tau_{\text{probe}}^2}} \cos(\angle(V_{\text{probe}}) + \phi - \angle(\frac{1}{1 + j\omega\tau_{\text{probe}}})). \tag{4.10}$$

The amplitude of the transmission spectrum I_0 is the amplitude of the above expres-

sion:

$$|I_0| = \frac{1}{2}|V_{\text{probe}}|\frac{G_1}{\sqrt{1+\omega^2\tau_{\text{probe}}^2}}. \tag{4.11}$$

The phase of the transmission spectrum, δ, is the argument of the cosine term in Eq. 4.10 at $\phi = 0$, plus a phase shift proportional to frequency to negate the 2 mm of pump-to-probe propagation delay contained in the complex amplitude V_{probe}:

$$\delta = \angle(V_{\text{probe}}) - \angle(\frac{1}{1+j\omega\tau_{\text{probe}}}) + \beta(.002). \tag{4.12}$$

The phase spectrum $\delta(f_d)$ is the sum of a term due to the circuit resonance that oscillates about zero, and a slowly-varying term δ_{pc} due to the different photoconductor response times, which is

$$\delta_{\text{pc}} = \angle\frac{1}{1+j\omega\tau_{\text{pump}}} - \angle\frac{1}{1+j\omega\tau_{\text{probe}}} = \angle\frac{1+j\omega\tau_{\text{probe}}}{1+j\omega\tau_{\text{pump}}}. \tag{4.13}$$

The parameters in the above model are I_1, G_1, τ_{pump}, τ_{probe} and $\alpha(f_d)$. I_1 and G_1 are easy to measure, because these are, respectively, simply the dc current in each active region of the pump photoconductor, and the dc zero-bias conductance of the single active region used of the probe photoconductor. We measured I_1 to be 53 μA at a 30 V bias. We measured G_1 by switching the power supplies to the probe photoconductor, and measuring the I-V curve of the single active region under illumination, at biases less than 3 V. G_1 was measured to be 1.26 $\mu\mho$. We measured τ_{probe} to be 1.2 ps with a mode-locked Ti:sapphire laser and the autocorrelation technique discussed in Sec. 2.6. To do the autocorrelation experiment, we monitored the dc photocurrent in the single active region of the probe photoconductor, at a bias of 1 V. We did not measure the voltage-dependence of the response time of the pump photoconductor, therefore τ_{pump} is an unknown fitting parameter. $\alpha(f_d)$ is also unknown, and we model it as

$$\alpha(f_d) = \begin{cases} \alpha_{\text{dc}}, & f_d < f_{\text{skin}} \\ \alpha_{\text{dc}}(\frac{f_d}{f_{\text{skin}}})^{.5}, & f_d > f_{\text{skin}} \end{cases}, \tag{4.14}$$

where α_{dc} is the attenuation coefficient at low frequencies, and f_{skin} is the frequency

at which the skin effect becomes appreciable. We neglect radiative losses, which are appreciable for CPWs with dimensions similar to ours only for frequencies greater than 400 GHz [73]. We treat α_{dc} and f_{skin} as fitting parameters.

A reasonably good fit of our model to the data is shown in Fig. 4-7. Note that for $f_d > 200$ GHz, to maximize the signal-to-noise ratio, we only measured I_0 at f_d such that the amplitude of I_0 was enhanced by resonance. Thus these data should be near the peaks of the model amplitude spectrum. The fit was achieved with the following values for the fitting parameters: $\tau_{pump} = 5.3$ ps, $\alpha_{dc} = .2$ mm^{-1} and $f_{skin} = 100$ GHz. The value of τ_{pump} is greater than the low-bias response time, τ_{probe}, by a factor of 4.5. This is reasonable, because Fig. 2-34 shows that the electron capture time in the photoconductor discussed in Chapter 1 is 4 to 5 times greater than its low-bias value at a bias of 18 V, which is the equivalent bias to the 30 V bias applied to the spectrometer circuit's pump photoconductor, because of the difference in gap length. As discussed in Chapter 1, it is the electron capture time that determines an LTG GaAs photoconductor's response time.

The value of α_{dc} is found to be reasonable by the following argument. For a moderately lossy transmission line, the attenuation coefficient α is $R/2Z_0$, where R is the resistance per unit length of the transmission line. The value of α_{dc} corresponds to $R = 17.6\ \Omega$/mm, which in turn corresponds to a conductivity of 2.3x10^7 Ω^{-1}m^{-1} for the gold of the 10-μm-wide, 250-nm-thick center conductor of our main CPW. This conductivity is a reasonable value.

The value of f_{skin} is reasonable as well because the skin depth at 100 GHz in gold with the above conductivity is 330 nm, which is almost the same as our gold thickness. Alexandrou *et al.* [73] measured the attenuation due to the skin effect in a CPW in the frequency range 100 GHz to 400 GHz, and found it to be very similar to what we measured.

Our data clearly show and our model predicts peaks in the amplitude spectrum at odd multiples of a fundamental frequency, and valleys at the even multiples. It is simple to show which standing waves these resonances correspond to. The ac voltages of two standing waves, one at the fundamental frequency and the other at

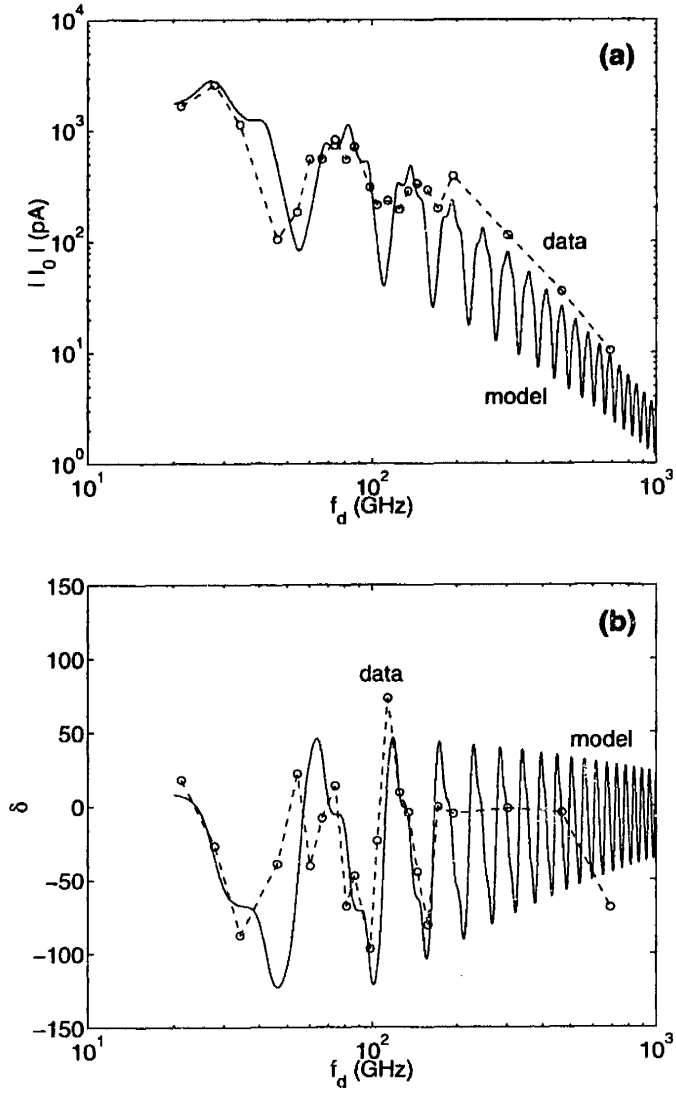

Figure 4-7: Fit of our model to the data of Fig. 4-5, with fitting parameters $\tau_{\text{pump}} = 5.3$ ps, $\alpha_{\text{dc}} = .2$ mm^{-1} and $f_{\text{skin}} = 100$ GHz.

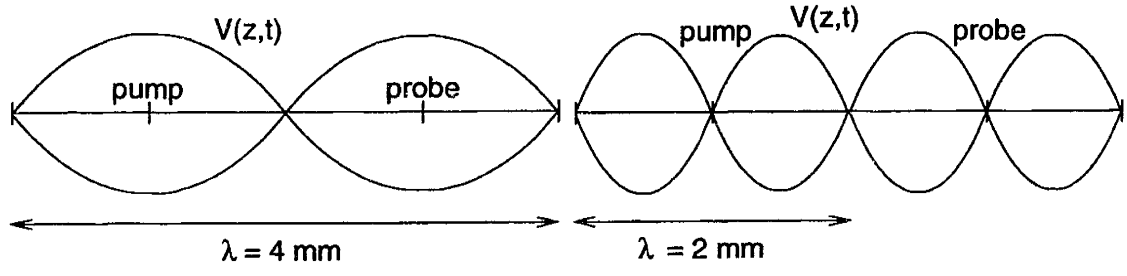

Figure 4-8: Standing waves in the spectrometer circuit. The first causes a peak in the amplitude of the transmission spectrum, the second causes a valley.

twice the fundamental frequency, are shown in Fig. 4-8. In each case, nodes are at the short terminations. In the first case, voltage maxima are at the pump and probe photoconductors, and in the second case, nodes are at the photoconductors. The output current is proportional to the amplitude of the ac voltage at the probe, therefore the output current peaks when there is a voltage maximum at the probe, at odd multiples of the fundamental frequency, and is minimum when there is a node at the probe, at even multiples of the fundamental. The fundamental frequency corresponds to a wavelength equal to the short-to-short distance of 4 mm. This frequency is $v_p/.004 = 27.5$ GHz. Resonant behavior, with enhanced and diminished output amplitude at the predicted set of frequencies, is evident in our data.

4.3.3 Dependence of the transmission spectrum's phase on pump voltage bias

To verify that the average value of δ is negative over most of our frequency range because the pump photoconductor's response time is large at high bias, we measured δ as a function of the pump photoconductor's bias (V_1 and V_2) at a fixed f_d of 85 GHz. This frequency is between the pole frequencies corresponding to τ_{probe} and τ_{pump} at $V_1 = 30$ V, therefore δ at $f_d = 85$ GHz should be strongly bias-dependent. The data were taken on a different day from the day the transmission spectrum data were taken, when we were unsure of z_{zpd}, so we could only measure relative changes in δ. The data are plotted in Fig. 4-9. The reference phase was chosen to match the model described below at the lowest voltage bias.

The bias-dependent part of δ is δ_{pc}, which is written explicitly in Eq. 4.13. Its bias-dependence comes from the bias-dependence of τ_{pump}. We adapt the models of Chapter 1 to derive $\tau_{\text{pump}}(V_1)$. In Sec. 2.5 we derive a model for the electric field-dependence of the electron capture time τ_e, based on electron heating and barrier-lowering of Coulomb-attractive electron capture sites. The model $\tau_e(E)$ is plotted as model (c) of Fig. 2-31. This model is of the form $\tau_e(E) = \tau_e(E = 0) \times f(E)$, therefore $\tau_{\text{pump}}(V_1)$ is simply $\tau_{\text{pump}}(V_1 = 0) \times f(E = V_1/l)$, where l is the gap length of the

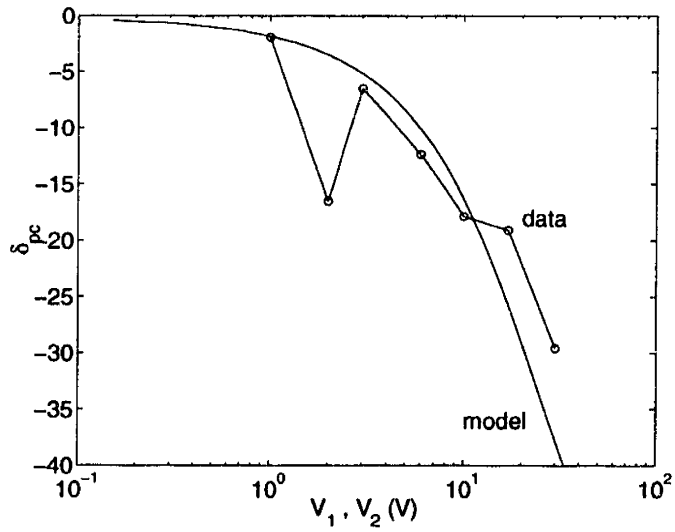

Figure 4-9: Portion of the transmission spectrum phase due to photoconductor response times as a function of the pump photoconductor bias ($V_1 = V_2$).

pump photoconductor of the spectrometer circuit, and $\tau_{\text{pump}}(V_1 = 0) = \tau_{\text{probe}} = 1.2$ ps. We plug the above $\tau_{\text{pump}}(V_1)$ into Eq. 4.13 to derive $\delta_{\text{pc}}(V_1)$, which is the model plotted in Fig. 4-9. The agreement between the model and our data is moderately good. The uncertainty in δ_{pc} is large at low V_1 due to low signal-to-noise ratio. Note that the LTG GaAs material of the spectrometer circuit is from a different source (FZ Jülich) than the source (MIT Lincoln Lab) of the LTG GaAs modeled in Chapter 2, thus we have proven the general applicability of the models of Chapter 1.

4.4 Discussion

4.4.1 Possible improvements

The measurements presented in this chapter are remarkable for spectral measurements of an integrated circuit because of the breadth of the frequency range considered (21.3 GHz to 689 GHz), and the frequency resolution (< 100 MHz actual resolution, 5.7 GHz minimum step between measurement frequencies). Both amplitude and phase information was obtained. However, Fig. 4-7 shows many discrepancies between our model and the measured data, which we believe are due to noise. The signal-to-noise

ratio must be reduced for photoconductive frequency-domain spectroscopy to be a viable alternative to time-domain spectroscopy.

One obvious way to do this is to increase the signal by increasing the responsivity of the pump and probe photoconductors. Photoconductors with interdigitated fingers have a greater effective width than the photoconductors we used, and have less metal surface area that reflects less incident light. These benefits would increase I_{o1} by one to two orders of magnitude. It is especially important to reduce the surface area of the metal wire between the two active regions of the pump photoconductor (see Fig. 3-1), because this is at the position of maximum pump beam intensity. Note that the pump and probe photoconductors should be optimized differently: the pump photoconductor must generate a large current, and the probe photoconductor must have a large conductance. Velocity saturation of photogenerated carriers is an issue with the pump photoconductor, but not with the probe photoconductor, because its ac voltage bias is small. Thus in general the probe photoconductor should have a smaller gap length than the pump photoconductor.

The data shown in Fig. 4-4 indicate that the noise in each individual measurement of I_{LIA1} is not enough to explain the discrepancies between our model and the data of Fig. 4-7. We can extract with precision the amplitude and phase of I_0 at a given frequency from data such as that shown in Fig. 4-4, which are measured within 4 minutes, but when we assemble the I_0 spectrum from measurements taken over a few hours, then the noise emerges. Obviously we are limited by the stability of our experimental set-up. We once measured I_0 at 82 GHz seven times, with seven separate scans over z within 35 minutes, without aligning the pump and probe beams before all but the first scan, and found that the measured amplitude of I_0 decreased steadily, and was 50% of its original value by the last scan. The phase was stable, except for a abrupt change of 50° between the sixth and seventh scan. We believe that the instability lies in the alignment of the pump and probe beams to the photoconductors, and is not caused by mode-hopping of the lasers, because the frequency variability of the lasers is not enough to cause the noise we observe.

One way to avoid the instability is to speed up the experiment, much of which is

performed manually. For example the lasers were tuned manually, and the speaker drive was adjusted manually. Also, the extra signal provided by more responsive photoconductors may make it possible to reduce the integration time of the lock-in amplifier, or avoid the phase-modulation-type technique altogether, and instead use a large-amplitude speaker drive to observe the sinusoidal $I_{o1}(z)$ without scanning through z with the motor-driven translation stage. As noted in Sec. 4.2, this measurement technique allows accurate alignment, because the sinusoid of interest can be viewed in real time. Repeated real-time alignment would counteract instability. The experimental setup could be stabilized by coupling the pump and probe beams to their respective photoconductors with optical fibers epoxied to the spectrometer circuit [78].

To better measure devices or chemical substances placed between the pump and probe photoconductors, we would like the transmission spectrum of our device-less circuit to be free of oscillations due to resonance. To eliminate resonance, we must use matched loads instead of shorts to terminate the parasitic CPWs, and make the characteristic impedances of the main CPW and the parasitic CPWs the same. We can also decrease the lengths of the main CPW and the parasitic CPWs, which would decrease resistive loss and beneficially increase the fundamental resonance frequency if the terminations of the parasitic CPWs were not perfectly matched loads.

4.4.2 Time-domain vs. frequency-domain spectroscopy

One very prominent difference between the time-domain data presented in chapter 3 and the frequency-domain data presented in this chapter, measured using the same circuit, is the magnitude of the output current I_{o1}. In chapter 3, the maximum I_{o1} measured is about 300 nA (see Fig. 4-5), whereas in this chapter the maximum I_{o1} is only about 3 nA (see Fig. 3-3). It is essentially this difference that makes the signal-to-noise ratio of the time-domain data so much better than that of the frequency-domain data. It is important to understand where this difference comes from, and whether or not time-domain spectroscopy has an advantage over frequency-domain spectroscopy in all cases.

Consider two sets of pump and probe beams with the same average power, one set from a mode-locked laser, the other set from two beating diode lasers. Assume the beams are incident on the same circuit, with the same pump photoconductor voltage bias, and that the beams are phased to generate maximum output current. Assume also that the optical intensities are low enough that the photocurrent of the pump photoconductor never saturates due to the finite voltage bias (see Sec. 2.6), and that the difference frequency of the laser diodes is low enough that the photoconductors can respond to it fully. It is simple to show that the mode-locked laser generates more output current by a factor of $\frac{1}{f\tau}$, where f is the repetition frequency of the mode-locked laser, and τ is the photoconductor response time. This is because we are essentially performing a correlation experiment, and the dc output current is proportional to the time integral of the square of the conductance waveform generated at each of the two photoconductors. One gets more output by squeezing that waveform in time, since the time-average conductance is a constant. The factor $\frac{1}{f\tau}$ is about 10^4 for typical values of f ($\approx$ 100 MHz) and τ ($\approx$ 1 ps), which gives quite an advantage to the time-domain output.

The weak assumption in the above argument is that the pump photocurrent never saturates. The peak photoconductance generated by the mode-locked laser is the same factor $\frac{1}{f\tau}$ times greater than the peak photoconductance generated by the laser diodes, therefore there is a large range of optical input power for which I_{o1} of the time-domain spectrometer is limited by saturation, but I_{o1} of the frequency-domain spectrometer is not. Photoconductors with interdigitated fingers can be used to boost the I_{o1} of frequency-domain circuits at high optical input power, while they would not improve the I_{o1} of time-domain circuits. Similarly, current efforts to increase the amount of optical input power photoconductors can withstand [8] will improve frequency-domain spectrometers more than time-domain spectrometers.

Appendix A

Electromagnetic Simulation

We found the finite-difference time-domain (FD-TD) electromagnetic simulator LC [80] to be an extremely useful design tool for laying out coplanar waveguide (CPW) circuits with embedded photoconductors. It convinced us of the importance of designing circuits with evenly symmetric discontinuities to avoid mode mixing, which lead to the mode-preserving circuits discussed in Chapter 3. We can't use it to directly compare the measurements of Chapters 3 and 4 with simulation, because the circuits we designed are too large and finely structured (4.5 mm^2 chip with 3 μm features and 0.3-μm-thick metal) to simulate accurately in their entirety. However, it is worthwhile to discuss and provide examples of the use of LC, so that others may take advantage of this useful and free software that can be run easily at M. I. T.

A.1 Simulation of pulse propagation on a CPW

FD-TD simulation is an inherently simple technique [1]. Maxwell's curl equations give the time derivatives of the electric and magnetic fields in terms of spatial derivatives of their complementary fields, and are naturally stated as difference equations for a discretized three-dimensional space with discrete time steps. To integrate the fields forward in time, the electric field is used to propagate forward the magnetic field, then the roles are reversed in the next time step to propagate forward the electric field.

[1] See [89] for a list of references about FD-TD simulation

Various types of materials can be included in the simulation simply by attributing the appropriate values of conductivity, permittivity and permeability to each spatial node.

LC performs its simulation within a regular three-dimensional mesh of points, with a default spacing of 1 mm, and a default time step of 1.668 ps. It allows the user to define three different types of blocks of space within the mesh: materials, sources and probes. The material blocks define the physical properties of the volume enclosed by the block. Source blocks have user-defined electric or magnetic field waveforms on their surfaces, which radiate into the rest of the mesh. Probe blocks are particular regions of the mesh that the user wants to extract information from. This information may be the electric and magnetic field data of the simulation itself, or derived quantities such as the total charge within a probe block, which is derived from the electric field with Gauss's law. LC offers many different types of boundary conditions as well. We usually chose absorbing boundary conditions to minimize the reflections of electromagnetic pulses hitting the boundaries. We found the boundary condition called perfectly matched layers [90] to be the most effective, although it requires the most RAM and computing time.

To verify that LC can accurately simulate pulse propagation on CPW circuits, we simulated a pulse propagating on a straight section of CPW on a GaAs substrate. A top view of the simulation mesh is shown in Fig. A-1, and a list of the simulation blocks is in Table A.1. Note that some of the blocks overlap. Since each mesh point can only be of one material type, each material block supersedes the ones listed above it. Some of the probe blocks also overlap, but this simply allows different quantities to be extracted from the same field data. The mesh is basically a 1:1000 replica of the main CPW of the circuit discussed in Chapter 3.

The current source excites a gaussian pulse of current in the center conductor of the CPW. The transient current $i_0(t)$ reaches a maximum of 1 A 0.956 ns after the start of the simulation, and has a full width at half maximum of 0.527 ns. Our simulation lasted 3000 times steps, which is about 5 ns. While LC has a few different types of waveforms it can generate itself, we supplied LC with an input file with the

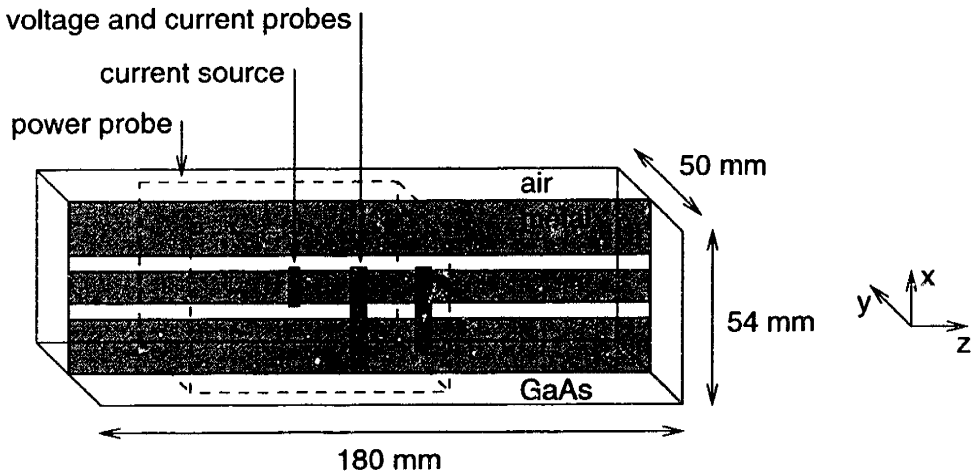

Figure A-1: Top view of the simulated CPW.

Table A.1: Blocks of the pulse propagation simulation, with the coordinates of block limits given in mm.

	x_-	x_+	y_-	y_+	z_-	z_+	waveform symbol
materials							
air	-27	27	-25	25	-80	100	
GaAs ($\epsilon_r = 13.1$)	-27	27	-25	0	-80	100	
metal ($\sigma = 3.27\text{x}10^7$ $\mho$/m):							
center conductor	-5	5	0	0	-80	100	
$+x$ ground plane	10	27	0	0	-80	100	
$-x$ ground plane	-27	-10	0	0	-80	100	
sources							
current source	-6	6	-1	1	-11	-9	i_0
probes							
center current probe 1	-6	-6	-1	1	9	11	i_1
center current probe 2	-6	-6	-1	1	29	31	i_2
side current probe 1	9	21	-1	1	9	11	i_{s1}
side current probe 2	9	21	-1	1	29	31	i_{s2}
voltage probe 1	4	11	-1	1	9	11	v_1
voltage probe 2	4	11	-1	1	29	31	v_2
front power probe	-25	25	-23	23	30	30	p_f
side power probe	25	25	-23	23	-50	30	p_s
top power probe	-25	25	23	23	-50	30	p_t
bottom power probe	-25	25	-23	-23	-50	30	p_b

current waveform because it seems to have trouble padding a self-defined gaussian pulse with zero current following the main peak.

We used three different types of probes to characterize the pulse propagation. Current probes give the line integral of the magnetic field around the probe block. We defined the orientation of our four current probes to give the current in the z direction. Note that two current probes define loops that wrap around the center conductor, and the other two wrap around the portion of the ground planes that carry the most transient current. The voltage probes give the electric field integral in a given direction, which we defined to be the x direction. We positioned two voltage probes to give the transient voltage between the center conductor and one ground plane. The power probes are planes which give the surface integral of the Poynting vector. We placed the power probes around the current source to compare the power radiated and guided away from it.

The simulated waveforms of all the probed quantities are shown in Fig. A-2. There are many signs that the simulation is accurate and physical. For example, the pulse's group velocity, as derived from the temporal difference between the peaks in $i_0(t)$ and $i_2(t)$, is 1.04x10^8 m/s, which is close to expected value of 1.1x10^8 m/s [10]. The ratio of the voltage peaks to the current peaks is 34.5 Ω, which is close to the expected characteristic impedance of 44 Ω [49]. We don't expect the derived characteristic impedance to be very accurate, because the mesh spacing of 1 mm is not much smaller then the 5 mm distance between each ground plane and the center conductor. The current pulse $i_2(t)$ is slightly dispersed, with a faster trailing edge than leading edge. This agrees with theory, which predicts that the effective dielectric constant of a CPW is an increasing function of frequency [72], and agrees with previous experiments as well [73]. The guided power p_f is about 20 times greater than p_b, the power radiated into the GaAs substrate, and much greater still than the power radiated into air and to the side. This is as expected, because the pulse width of about 55 mm is greater than the 20 mm distance between ground planes, thus the ground planes effectively shield the substrate an air from radiation. That more power is radiated into the GaAs substrate than into air is also as expected, since GaAs presents a lower impedance to

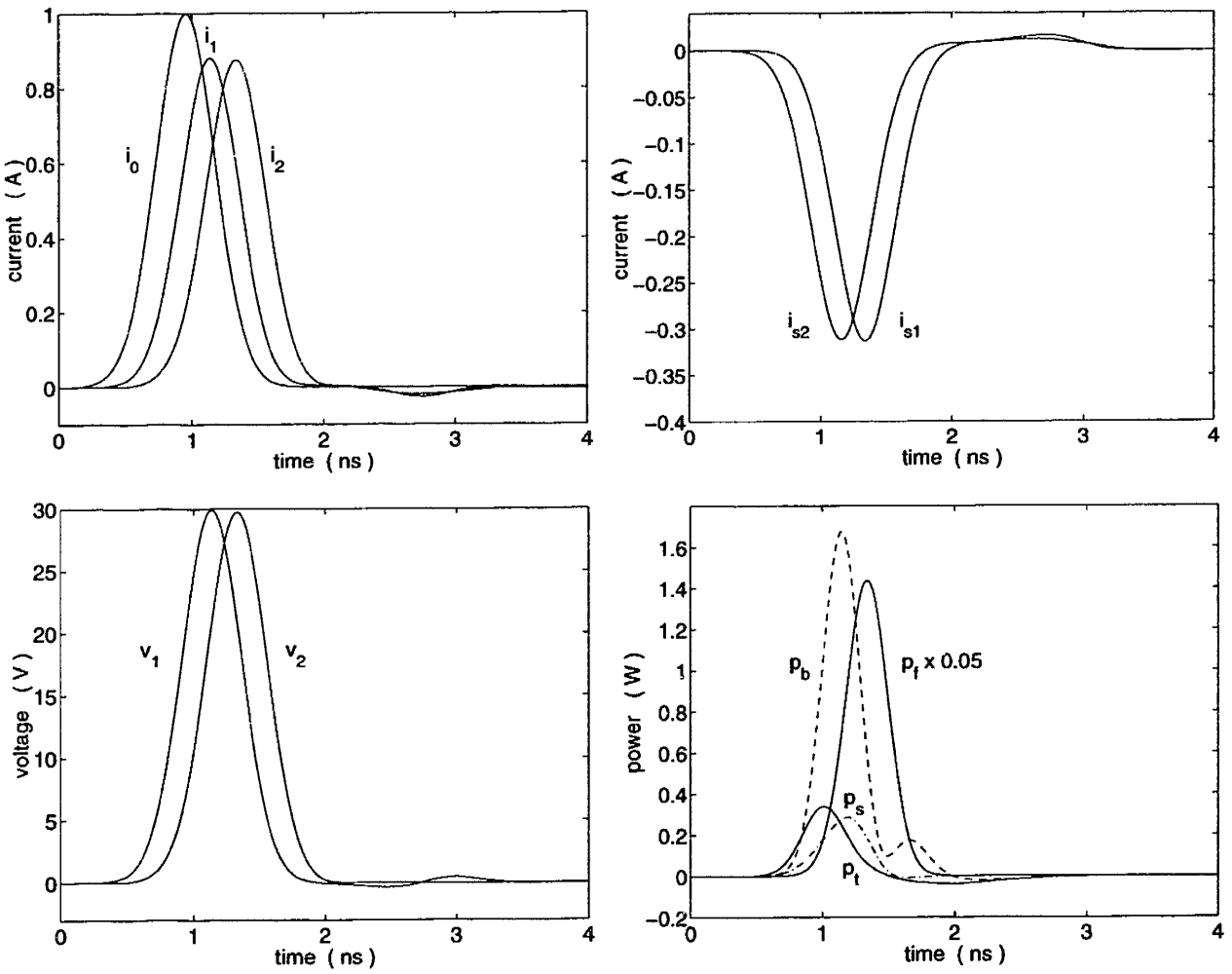

Figure A-2: Simulated waveforms of all the probed quantities.

the radiating current than air does [44]. Also as expected, the currents i_{s1} and i_{s2} in the ground plane are very similar to the currents i_1 and i_2 in the center conductor, but are about half the magnitude and have the opposite sign.

There are a few non-physical results that must be noted. The boundaries at $z = -80$ mm and $z = 100$ mm both produce reflections that are evident in the current and voltage waveforms near a time of 3 ns. Fortunately, these features are of low amplitude, and have substantial temporal separation from the main peaks. The difference in amplitude between the excitation current i_0 and the propagating currents i_1 and i_2 is also non-physical. The amplitude of i_2 is slightly less than that of i_1, due to both resistive and radiative attenuation, but both are much less than the amplitude of i_0. The power probes show that radiation into the substrate does not account for the difference. Perhaps the difference arises because an isolated current source is intrinsically non-physical.

Since the absolute magnitude of the waveforms calculated by LC are slightly dubious, the conclusion we draw from the above investigation is that LC is very good for comparing the relative transmission properties of different discontinuities in a transmission line circuit. To make the main features of waveforms distinguishable from those features due to reflections at simulation boundaries, we need simply position our probes far from the boundaries.

A.2 Pulse propagation through a discontinuity

One structure we would like to know the transmission properties of is the double photoconductor described in Chapter 3. The data presented in the chapter suggest that this structure transmits a large portion of an electromagnetic pulse incident from the main CPW of the experimental circuit. To verify this, we created the simulation mesh shown in Fig. A-3, which is basically a 1:1000 replica of a section of the experimental circuit with a double photoconductor. A list of the simulation blocks is in Table A.2. We created another simulation for comparison with the same size and probes as the one shown in Fig. A-3, but with a straight CPW and no discontinuity.

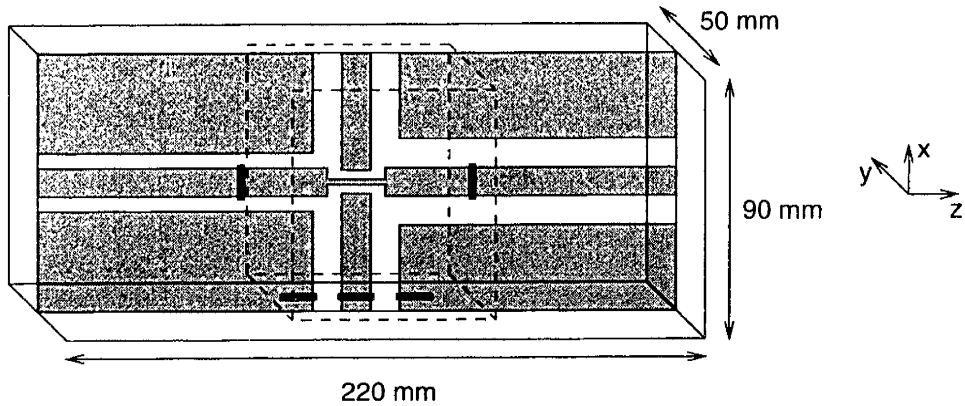

Figure A-3: Top view of the simulated CPW with a double photoconductor. The colors and symbols for materials, sources and probes are the same as in Fig. A-1.

Table A.2: Blocks of the simulation with a discontinuity, with the coordinates of block limits given in mm.

	x_-	x_+	y_-	y_+	z_-	z_+	waveform symbol
materials							
air	-45	45	-25	25	-80	140	
GaAs	-45	45	-25	0	-80	140	
metal:							
$-z$ center conductor	-5	5	0	0	-80	20	
mid-z center conductor	-1	1	0	0	19	41	
$+z$ center conductor	-5	5	0	0	40	140	
$+x$ center conductor	4	45	0	0	25	35	
$-x$ center conductor	-45	-4	0	0	25	35	
$+x, +z$ ground plane	15	45	0	0	45	140	
$-x, +z$ ground plane	-45	-15	0	0	45	140	
$-x, -z$ ground plane	-45	-10	0	0	-80	15	
$+x, -z$ ground plane	10	45	0	0	-80	15	
sources							
current source	-6	6	-1	1	-11	-9	i_0
probes							
center current probe	-6	-6	-1	1	69	71	i_1
stub center current probe	39	41	-1	1	24	36	i_{sc}
stub near side current probe	39	41	-1	1	4	16	i_{sn}
stub far side current probe	39	41	-1	1	44	56	i_{sf}
front power probe	-40	40	-23	23	70	70	p_f
side power probe	40	40	-23	23	0	70	p_s
top power probe	-40	40	23	23	0	70	p_t
bottom power probe	-40	40	-23	-23	0	70	p_b

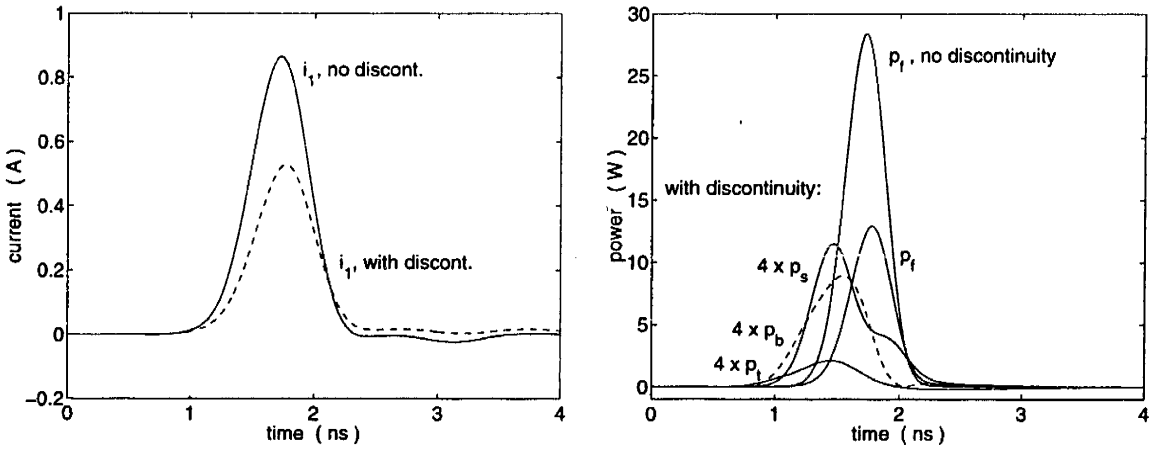

Figure A-4: Comparison of current and power waveforms for simulations with and without a double-photoconductor discontinuity. p_f is the power in the probe plane at extreme $+z$, p_s is the power in the plane at extreme $+x$, p_b is the power in the plane at extreme $-y$, and p_t is the power in the plane at extreme $+y$ (see Fig. A-3 and Table A.2).

In Fig. A-4 we compare the transmitted current i_1 and the radiated and guided power of the two simulations. Note that i_1 for the simulation with no discontinuity is mainly a delayed version of i_1 and i_2 of the simulation discussed in the previous section, and shown in Fig. A-2. This is to be expected, because of the greater distance between source and probe for the later simulations. Note also that the discontinuity causes only a 39% reduction in the transmitted current. We see that more power is transmitted through the double photoconductor than diverted to the parasitic CPWs in the x direction, which are used to bias the double photoconductor.

With the simulator we can see in detail how the pulse on the main CPW couples to the CPWs orthogonal to it. Figure A-5 (a) shows the currents i_{sn}, i_{sc} andi_{sf} in the CPW orthogonal to the main CPW in the z direction. The waveforms show that two pulses of opposite sign are launched onto the parasitic CPW, with a small time delay between them. These pulses in i_{sn} and i_{sf} are induced by the currents in the ground planes of the main CPW, as shown in Fig. A-5 (b). i_{sc} is bipolar becuase it is composed of separate pulses of opposite sign induced by the currents in the nearby ground planes. The odd propagating mode of the main CPW (see Fig. 2-19) does not couple to the odd propagating mode of the parasitic CPW, but rather to the

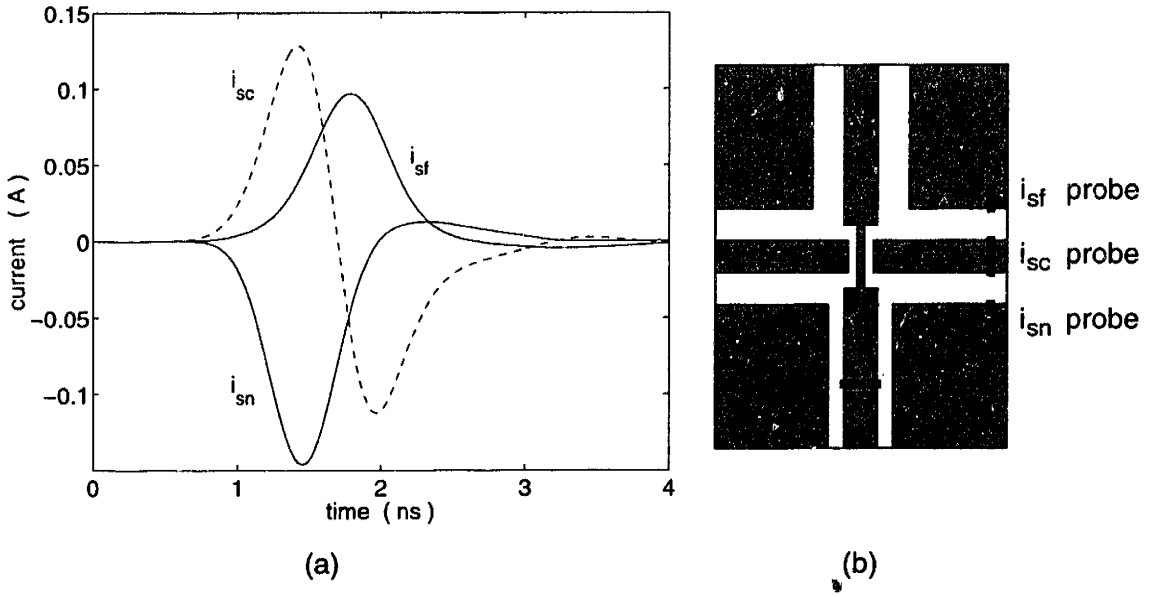

Figure A-5: (a): Currents in the CPW used to bias the double photoconductor. (b): Circuit diagram showing the currents induced by the source pulse, which explains why i_{sn} and i_{sf} are of opposite sign.

slotline-like modes localized on either side of the parasitic CPW. This must be kept in mind when considering what impedance the parasitic CPWs present to the main CPW.

The simulation reveals that the double-photoconductor structure is fairly transmissive, and gives some insight into how it interferes with pulse propagation. To learn even more from simulation, we could vary the simulated discontinuity to maximize the transmitted power, so as to avoid diverting power to the parasitic CPWs or reflecting it back to the pump photoconductor. As a first step in this direction, we created a simulated circuit identical to the one in Fig. A-3, except that its CPW in the z direction at high z has a lower characteristic impedance Z_0 than the same CPW of the original simulation. The dimensions of the original simulation's high z CPW are 10 mm-10 mm-10 mm, while those of the new simulation are 5 mm-10 mm-5 mm, the same dimensions as those of the low-z CPW of both simulations. In Fig. A-6 we compare the transmitted power and current waveforms of the two simulations. The original simulation, with the high-z CPW with the higher Z_0, has less transmitted current but more transmitted power. Apparently increasing the load seen by a pulse

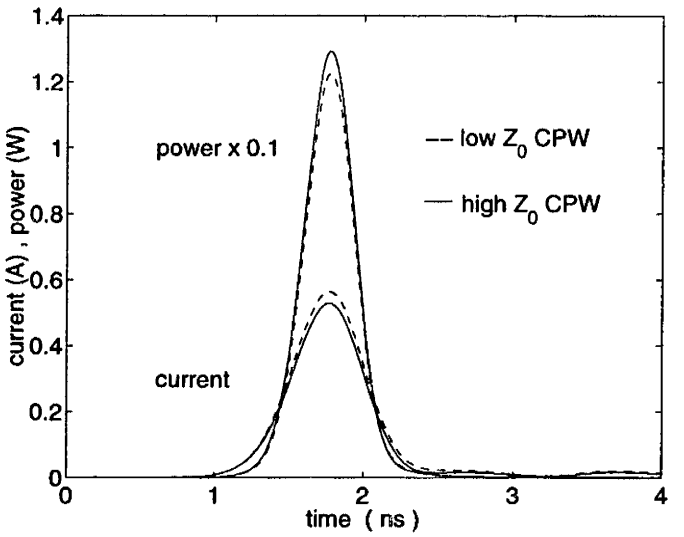

Figure A-6: Comparison of transmitted current i_1 and transmitted power p_f of simulations with CPWs of different characteristic impedance at high z.

incident on the discontinuity makes the load a better match to the CPW that the pulse is incident from (the main CPW at low z).

As stated in Sec. 3.4, the best way to experimentally verify FD-TD simulations of discontinuities is to use a mobile electric field probe to compare the electric field waveforms in different regions of a circuit, much as we use multiple probes in our simulation. While we did not perform such experiments, most of LC's calculations are physically reasonable, and give us confidence that LC is a useful tool for the design of CPW circuits. To future users of LC at M. I. T., we must add that LC only runs on SGI computers, the fastest of which (as of May 1999) are the O2 machines in the Athena cluster in room 4-035.

Appendix B

Experimental Equipment and Tips

In this appendix we discuss how to use the equipment on the laser table in room 26-468, which consists of an argon laser that pumps a Ti:sapphire laser whose mode-locked beam is used for pump-and-probe experiments. We also describe how to epoxy an optical fiber to an chip (see [78]).

B.1 Turning on the lasers

The argon laser consumes so much power that it requires a large cooling system. The Ti:sapphire laser requires a smaller cooler. Turning the lasers on mostly involves turning these systems on and making sure that they work. The argon laser cooling system consists of a closed water loop that cools both the argon laser and its power supply under the laser table, a heat exchanger, and an extension of the chilled water loop of building 26. The flow of the house chilled water is increased with a booster pump. The Ti:sapphire laser's chiller controls the temperature of the sapphire crystal with a closed water loop. The chiller is under the laser table near the booster pump. The lasers are turned on as follows.

1. Turn on both valves of the house chilled water loop, on the supply and return (the long vertical pipes on the wall behind the laser). Allow some water to flow through the booster pump for half a minute. Verify that there is flow by looking for a slight

movement of the flow meter, the glass pipe with a spring inside.

2. Turn on the Neslab heat exchanger. The pressure indicator should read about 62 lb/in^2. The "flow" indicator on the argon laser status display should turn off (the laser is always powered). Check the water reservoir to make sure the level is at most an inch from the top. Check every once in a while for leaks under the laser table.

3. Plug in the booster pump to turn it on. The spring on the flow meter should extend to its maximum. The pressure indicated on the gauge on the pump should read about 100 lb/in^2. The temperature of the house chilled water supply will drop quickly, and that of the house chilled water return will drop more slowly. After these temperatures stabilize, you are ready to turn on the argon laser. Do step 4 before turning it on. Keep in mind that the argon laser will make the return temperature about 5 to 10° F hotter than the supply temperature, and that the return temperature is an estimate of the laser temperature. Make sure that the laser will operate within its specified temperature range. The temperature of the argon laser is not regulated, and water should not be allowed to condense on the laser tube, so do not cool the argon laser for too long before turning the argon laser on.

4. Before turning on the argon laser: turn on the Ti:sapphire laser's chiller. The argon laser beam is focused on the sapphire crystal inside the Ti:sapphire laser whenever the argon laser is on, so be sure the crystal temperature is regulated before heating it with the argon laser. Also, check that Ti:sapphire laser beam is blocked (usually just beyond the circular attenuator) for safety.

5. Turn on the argon laser by turning the key clockwise. There is a delay before the power supply turns on, then the power ramps up slowly. The laser should have already been set to "beamlok" (active beam steering), to display the power, to constant-current mode, and to a current that corresponds to a power of about 3.2 W. The power will reach a maximum, then slowly drop over the next 20 minutes to about 3.0 W.

6. Let the laser warm up for about half an hour.

7. Switch the laser from constant-current mode to constant-power mode. The power level should already have been set to 3 W, to match the current level. Turn the power level up to 7 W, which is the typical power level for mode-locking the Ti-sapphire laser. The Ti:sapphire laser beam should be visible, since the Ti:sapphire laser's threshold pump power is 3 to 4 W. The lasers are now ready to use.

B.2 Mode-locking the Ti:sapphire laser

To mode-lock the Ti:sapphire laser, simply press the square black button in the "status" section of the 3955 module above the laser table. This turns on the acousto-optic modulator (AOM) inside the laser cavity. The "pulsing" light on the 3955 should turn on. However, the light merely indicates that the laser beam intensity has a modulation at the AOM's frequency, and is no guarantee that the laser is truly mode-locked.

There are three ways to see if the Ti:sapphire laser is mode-locked. The easiest way is to look at the beam spot on a white card. Look at the spot of a beam of moderate intensity, such as the spot on the body of the argon laser from the beam reflected off of the circular attenuator. If the spot is speckled, then the laser beam is highly coherent, has a very narrow spectrum and is not mode-locked. If it is uniform and unspeckled, then the laser is mode-locked.

The next easiest way to check for mode-lock is to look at the "monitor" output of the 3955 module on an oscilloscope. Use the "sync" output as the trigger. If the "monitor" output is a clean, sharp sinusoid at the AOM frequency (82 MHz), then the laser is probably mode-locked. If it is not, then the laser is definitely not mode-locked. This is probably the best way to monitor the Ti:sapphire laser in real time, while tweaking the micrometers on top of the laser that control its center frequency and bandwidth.

The most accurate way to check the condition of the Ti:sapphire laser is to measure its spectrum. To do this, divert some of the Ti:sapphire beam to the spectrometer

with a motorized grating in the middle of the laser table. Make sure a digital voltage meter (DVM) is hooked up properly to the photodiode at the spectrometer's output. Use the Labview software to initialize the spectrometer and the DVM, and to measure the spectrum. If the laser is mode-locked, the spectrum will be broad and smooth, and if it's not, the spectrum will be similar to an impulse. A typical mode-locked spectrum has an amplitude of 3 mV, a center wavelength of 770 nm, and a spectral width of 10 nm.

The Ti:sapphire laser usually mode-locks easily and repeatably from day to day. If it doesn't mode-lock, turn off the AOM, turn the argon laser power down to the Ti:sapphire laser's threshold, and use the optical power meter to minimize the threshold pump power, as described in the Ti:sapphire laser's manual. Then turn the argon laser power back up to 7 W and try to mode-lock the Ti:sapphire laser again. If it still does not work, try to make it mode-lock at a center wavelength of about 760 nm. The shortest pulse widths are achieved with a center wavelength of about 780 nm, which is at the high extreme of the Ti:sapphire laser's working range. At 760 nm, the pulse width is longer, but the threshold pump power is lower and the laser seems to mode-lock more easily.

After mode-lock is achieved, the Ti:sapphire laser can be adjusted to decrease the pulse width. Usually this can be accomplished by raising the wavelength with the appropriate micrometer, and monitoring the oscilloscope to make sure the laser stays mode-locked. If it falls out of mode-lock, turn the micrometer the other way and the laser should re-lock. If neither minimizing the pump threshold power nor reducing the Ti:sapphire wavelength achieves mode-lock, consult the Ti:sapphire laser manual. The mode-lock should be stable enough to turn off the AOM and maintain mode-lock.

B.3 Shutdown

Block the Ti:sapphire laser beam. Turn off the AOM if it's on. Turn the argon laser power down to 3 W and switch the argon laser from constant-power to constant-current mode. The power usually drops to about 2.8 W, but doesn't need to be

adjusted. Turn off the argon laser with the key. Wait until the house chilled water supply and return temperatures are approximately equal, then unplug the booster pump, turn off the Neslab heat exchanger, and close the two house chilled water valves.

B.4 Other information

The power supplies of the op-amps of the transimpedance amplifiers inside the bias box are set at ± 12 V. The power supplies of the audio amplifier that drives the speaker are set at ± 11 V. A typical speaker drive is a sinusoid of 20 Hz frequency and 4.4 V peak-to-peak amplitude (the HP116A pulse/function generator's hi and lo levels are set to ± 1.1 V). Use the shorting switches on the bias box to protect the device under test from ESD.

Steps to epoxy an optical fiber to a LTG GaAs chip: ask Simon Verghese and Alex MacIntosh of Lincoln Lab for advice. Mount the chip facing upwards to counteract the pull of gravity on the epoxy. Make sure the "black light" in the lab (the UV source) can be placed near the chip to cure the epoxy. Remove the fiber's acrylate coating and cleave it if necessary. Align the dry fiber. Translate the fiber away from the chip to allow room to apply epoxy. Use fresh epoxy. Put a bead of epoxy on a wand made of optical fiber identical to the fiber to be epoxied. While viewing through a microscope, wet the *face* of the fiber with the bead on the wand, making sure to make a small, symmetric bead. Translate the fiber back to the chip and make contact, wetting the chip surface. Re-align the fiber as little possible, to avoid making the blob of epoxy on the chip non-symmetric. Cure overnight with the "black light".

Bibliography

[1] M. C. Nuss and J. Orenstein, "Terahertz Time-Domain Spectroscopy", in Millimeter and Submillimeter Spectroscopy of Solids, ed. by G. Grüner, Springer (1998).

[2] M. Matloubian, C. Pobanz, D. Docter, M. Case, M. Micovic, C. Nguyen, M. Yu, M. Lui, "Submillimeter wave InP-based HEMTs with fmax over 600 GHz", in Technical Digest of Ultrafast Electronics and Optoelectronics, paper UThC1, Optical Society of America (1999).

[3] N. Gopalsami and A. C. Raptis, "Remote detection of chemicals by millimeter-wave spectroscopy", Proc. SPIE **3465**, 254 (1998).

[4] Q. Hu, S. Verghese, R. A. Wyss, T. Schäpers, J. del Alamo, S.Feng, K. Yakubo, M. J. Rooks, M. R. Melloch and A. Förster, "High-frequency (f 1 THz) studies of quantum-effect devices", Semicond. Sci. and Tech. **11**, 1888 (1996).

[5] S. Verghese, K. A. McIntosh, S. Calawa, W. F. Dinatale, E. K. Duerr, K. A. Molvar, "Generation and detection of coherent terahertz waves using two photomixers", Appl. Phys. Lett. **73**, 3824 (1998).

[6] S. Y. Chou, Y. Liu, W. Khalil, T. Y. Hsiang and S. Alexandrou, "Ultrafast nanoscale metal-semiconductor-metal photodetectors on bulk and low-temperature-grown GaAs", Appl. Phys. Lett. **61**, 819 (1992).

[7] E. R. Brown, K. A. McIntosh, K. B. Nichols and C. L. Dennis, "Photomixing up to 3.8 THz in low-temperature-grown GaAs", Appl. Phys. Lett. **66**, 285 (1995).

[8] S. Verghese, K. A. McIntosh and E. R. Brown, "Optical and terahertz power limits in low-temperature-grown GaAs photomixers", Appl. Phys. Lett. **71**, 2743 (1997).

[9] M. Y. Frankel, J. F. Whitaker, G. A. Mourou, F. W. Smith and A. R. Calawa, "High-voltage picosecond photoconductor switch based on low-temperature-grown GaAs", IEEE Trans. Electron Devices **37**, 2493 (1990).

[10] J. Allam, N. de B. Baynes, J. R. A. Cleaver, K. Ogawa, T. Mishima and I. Ohbu, "Monolithically-integrated optoelectronic circuit for ultrafast sampling of a dual-gate field-effect transistor", Opt. and Quantum Elec. **28**, 875 (1996).

[11] E. R. Brown, K. A. McIntosh, F. W. Smith, K. B. Nichols, M. J Manfra, C. L. Dennis and J. P. Mattia, "Milliwatt output levels and superquadratic bias dependence in a low-temperature-grown GaAs photomixer", Appl. Phys. Lett. **64**, 3311 (1994).

[12] S. Matsuura, G. A. Blake, R. A. Wyss, J. C. Pearson, C. Kadow, A. W. Jackson and A. C. Gossard, "Traveling-wave photomixers based on noncollinear optical/terahertz phase-matching", Proceedings of the Tenth International Symposium on Space Terahertz Technology (1999).

[13] J. P. Ibbetson and I. K. Mishra, "Space-charge-limited currents in nonstoichiometric GaAs", Appl. Phys. Lett. **68**, 3781 (1996).

[14] S. Gupta, "Carrier Dynaimics in III-V Materials and Hetero-structures Studied by Ultrafast Laser Techniques", PhD Thesis, The University of Michigan, Department of Electrical Engineering, 1992.

[15] S. Gupta, M. Y. Frankel, J. A. Valdmanis, J. F. Whitaker, G. A. Mourou, F. W. Smith and A. R. Calawa, "Subpicosecond carrier lifetime in GaAs grown by molecular beam epitaxy at low temperatures", Appl. Phys. Lett. **59**, 3276 (1991).

[16] F. Smith, "The Device Applications and Characterization of Nonstoichiometric GaAs Grown by Molecular Beam Epitaxy", PhD Thesis, Massachusetts Institute of Technology, Department of Electrical Engineering and Computer Science, 1990.

[17] E. S. Harmon, M. R. Melloch, J. M. Woodall, D. D. Nolte, N. Otsuka and C. L. Chang, "Carrier lifetime versus anneal in low temperature growth GaAs", Appl. Phys. Lett. **63**, 2248 (1993).

[18] D. C. Look, D. C. Walters, M. O. Manasreh, J. R. Sizelove, C. E. Stutz and K. R. Evans, "Anomalous Hall-effect results in low-temperature molecular-beam-epitaxial GaAs: hopping in a dense *EL2*-like band", Phys. Rev. B, **42**, 3578 (1990).

[19] P. Kordoš, M. Marso, A. Förster, J. Darmo, J. Betko and G. Nimtz, "Space-charge-controlled conduction in low-temperature-grown molecular-beam epitaxial GaAs", Appl. Phys. Lett. **71**, 1118 (1997).

[20] X. Liu, A. Prasad, W. M. Chen, A. Kurpiewski, A. Stoschek, Z. Lilienthal-Weber and E. R. Weber, "Mechanism responsible for the semi-insulating properties of low-temperature-grown GaAs", Appl. Phys. Lett. **65**, 3002 (1994).

[21] D. C. Look, D. C. Walters, G. D. Robinson, J. R. Sizelove, M. G. Mier and C. E. Stutz, "Annealing dynamics of molecular-beam epitaxial GaAs grown at 200 °C" J. Appl. Phys. **74**, 306, 1993.

[22] M. Stellmacher, J. Schnell, D. Adam, J. Nagle, "Photoconductivity investigation of the electron dynamics in GaAs grown at low temperature", Appl. Phys. Lett. **74**, 1239 (1999).

[23] A. J. Lochtefeld, M. R. Melloch, J. C. P. Chang and E. S. Harmon, "The role of point defects and arsenic precipitates in carrier trapping and recombination in low-temperature grown GaAs", Appl. Phys. Lett. **69**, 1465 (1996).

[24] C. Y. Sung, H. H. Wang, T. B. Norris, J. F. Whitaker, "Ultrafast electron and hole trapping times and defect band saturation dynamics in low-temperature-

grown GaAs", in Conference on Lasers and Electro-Optics, Vol. 9, p. 454, Optical Society of America (1996).

[25] A. C. Warren, J. M. Woodall, J. L. Freeouf, D. Grischkowsky, D. T. McInturff, M. R. Melloch and N. Otsuka, "Arsenic precipitates and the semi-insulating properties of GaAs buffer layers grown by low-temperature molecular beam epitaxy", Appl. Phys. Lett. **57**, 1331 (1990).

[26] M. R. Melloch, J. M. Woodall, E. S. Harmon, N. Otsuka, F. H. Pollak, R. M. Feenstra and M. A. Lutz, Annu. Rev. Mater. Sci. **25**, 547 (1995).

[27] K. A. McIntosh, K. B. Nichols, S. Verghese and E. R. Brown, "Investigation of ultrashort photocarrier relaxation times in low-temperature-grown GaAs", Appl. Phys. Lett. **70**, 354 (1997).

[28] X.-Q. Zhou, H. M. van Driel, W. W. Rühle, Z. Gogolak, and K. Ploog, "Femptosecond carrier kinetics in low-temperature-grown GaAs", Appl. Phys. Lett. **61** 3020 (1992).

[29] H. Yamamoto, Z-Q. Fang and D. C. Look, "Nonalloyed ohmic contacts on low-temperature molecular beam epitaxial GaAs: influence of deep donor band", Appl. Phys. Lett. **57**, 1537 (1990).

[30] S. P. Wilson and A. B. Walker, "One- and two-dimensional models of the transient response of metal-semiconductor-metal photodetectors including diffraction", Semicond. Sci. Technol. **12**, 1265 (1997).

[31] M. A. Lampert and P. Mark, "Curent Injection in Solids", Academic Press (1970).

[32] S. E. Ralph and D. Grischkowsky, "Trap-enhanced electric fields in semi-insulators: the role of electrical and carrier injection", Appl. Phys. Lett. **59** 1972 (1991).

[33] S. Shiobara, K. Sasaki and H. Hasegawa, "Surface electrical breakdown characteristics of molecular beam epitaxial layers grown at low temperatures", Solid State Electronics **38**, 1685 (1995).

[34] P. J. Corvini and J. E. Bowers, "Model for trap filling and avalanche breakdown in semi-insulating Fe:InP", J. Appl. Phys. **82**, 259 (1997).

[35] J. K. Luo, H. Thomas, D. V. Morgan and D. Westwood, "Transport properties of GaAs layers grown by molecular beam epitaxy at low temperature and the effects of annealing", J. Appl. Phys. **79**, 3622 (1996).

[36] S. Sze, "Physics of Semiconductor Devices", John Wiley and Sons (1981).

[37] J. K. Luo, H. Thomas, D. V. Morgan and D. Westwood, "Thermal annealing effect on low temperature molecular beam epitaxy grown GaAs: arsenic precipitation and the change of resistivity", Appl. Phys. Lett. **64**, 3614 (1994).

[38] J. P. Ibbetson, J. S. Speck, N. X. Nguyen, A. C. Gossard and U. K. Mishra, "The role of microstructure in the electrical properties of GaAs grown at low temperature", J. Electron. Mater. **22**, 1421 (1993).

[39] P. Arifin, E. Goldys and T. L. Tansley, "Monte Carlo simulation of electron drift velocity in low-temperature-grown gallium arsenide in a Schottky-barrier model", Phys. Rev. B **52** 5708 (1995).

[40] W. T. Masselink and T. F. Kuech, "Velocity-field characteristics of electrons in doped GaAs", J. Elec. Mat. **18** 579 (1989).

[41] H. M. van Driel, X.-Q. Zhou, W. W. Rühle, J. Kuhl and K. Ploog, "Photoluminescence from hot carriers in low-temperature-grown gallium arsenide", Appl. Phys. Lett. **60** 2246 (1992).

[42] G. S. Hobson, "The Gunn Effect", p. 48, Oxford University Press (1974).

[43] C. Ludwig and J. Kuhl, "Studies of the temporal and spectral shape of terahertz pulses generated from photoconducting switches", Appl. Phys. Lett. **69** 1194 (1996).

[44] P. R. Smith, D. H. Auston and M. C. Nuss, "Subpicosecond Photoconducting dipole antennas", IEEE J. Quantum Electron. **24** (1988).

[45] J. Son, W. Sha, J. Kim, T. B. Norris, J. F. Whitaker and G. A. Mourou, "Transient velocity overshoot dynamics in GaAs for electric fields $\leq$ 200 kV/cm", Appl. Phys. Lett. **63** 923 (1993).

[46] D. J. Griffiths, "Introduction to Electrodyanmics", Prentice Hall (1989).

[47] U. D. Keil, J. M. Hvam, S. Tautz, S. U. Dankowski, P. Kiessel, G. H. Döhler, "Femptosecond differential transmission measuremnts on low temperature GaAs metal-semiconductor-metal structures", Appl. Phys. Lett. **70**, 72 (1997).

[48] J. S. Blakemore, "Semiconducting and other major proerties of gallium arsenide", J. Appl. Phys. **53**, R123 (1982).

[49] B. Wadell, "Transmission Line Design Handbook", Artech House (1991).

[50] E. R. Brown, submitted to Appl. Phys. Lett.

[51] Atlas device simulation software with Luminous, an add-on for optoelectronic simulation. Owned by M. I. T. Lincoln Laboratory.
http://www.silvaco.com/products/atlas/atlas.html

[52] L.-W. Yin, J. P. Ibbetson, M. M. Hashemi, A. C. Gossard, U. K. Mishra, Y. Hwang, T. Zhang and R. M. Kolbas, "Investigation of the electronic properties of *in situ* annealed low-temperature gallium arsenide grown by molecular beam epitaxy", Appl. Phys. Lett. **60**, 2005 (1992).

[53] D. C. Look, "Electrical Characterization of GaAs Materials and Devices", p. 132, John Wiley and Sons (1989).

[54] M/A-COM III-V Materials Data Sheets
http://www.macom-gaaswafers.com/data.html

[55] The 1994 catalog of Newport Corporation, p. 2.100.

[56] T. H. Ning, "High-field capture of electrons by Coulomb-attractive centers in silicon dioxide", J. Appl. Phys. **47** 3203 (1976).

[57] G. A. Dussel and K. W. Böer, "Field-enhanced ionization", Phys. Status Solidi **39** 375 (1970).

[58] D. Auston, "Picosecond optoelectronic switching and gating in silicon", Appl. Phys. Lett. **26** 101 (1975).

[59] Y. Chen, S. Williamson, T. Brock, F. Smith and A. Calawa, "375-Ghz-bandwidth photoconductive detector", Appl. Phys. Lett. **59** 1984 (1991).

[60] S. Verghese, N. Zamdmer, Q. Hu, E. Brown and A. Förster, "An optical correlator using a low-temeprature-grown GaAs photoconductor", Appl. Phys. Lett. **69** 842 (1996).

[61] J. Valdmanis, "1 THz-bandwidth prober for high-speed devices and integrated circuits", Electron. Lett. **23** 1308 (1987).

[62] R. Jacobsen, K. Birkelund, T. Holst, P. Uhd Jepsen and S. Keiding, "Interpretation of photocurrent correlation measurements used for ultrafast photoconductive switch characterization", J. Appl. Phys. **79**, 2649 (1996).

[63] T. S. Sosnowski, T. B. Norris, H. H. Wang, P. Grenier, J. F. Whitaker and C. Y. Sung, "High-carrier-density electron dynamics in low-temperature-grown GaAs", Appl. Phys. Lett. **70** 3245 (1997).

[64] E. K. Duerr, K. A. MacIntosh, S. Verghese, "Design of a Distributed Terahertz Photomixer", Proceedings of the Tenth International Symposium on Space Terahertz Technology (1999).

[65] J. P. Kreskovsky and H. L. Grubin, "Numerical studies of annealed non-stoichiometric low temperature grown GaAs", J. Appl. Phys. **81**, 7326 (1997).

[66] C. Moglestue, J, Rozenzweig, J. Kuhl, M. Klingenstein, Lambsdorff, A. Axmann, J. Schneider and A. Hülsmann, "Picosecond pulse rrsponse characteristics of GaAs metal-semiconductor-metal photodetectors", J. Appl. Phys. **70**, 2435 (1991).

[67] M. Y. Frankel, "500-GHz characterization of an optoelectronic S-parameter test structure", IEEE Microwave Guided Wave Lett. **4** 118 (1994).

[68] A. Zeng, M. K. Jackson, M. Van Hove and W. de Raedt, "Electrooptic characterization of modulation-doped field-effect transistors with monolithically-integrated test fixtures", Opt. and Quantum Elec. **28**, 867 (1996).

[69] J. A. Sheridan, B. A. Nechay, D. M. Bloom, P. M. Solomon and Y. C. Pao, "Direct measurement of transit time effects in MODFETs", in IEDM Technical Digest, p. 579, Institute of Electrical and Electronics Engineers (1994).

[70] K. Ogawa, J. Allam, N. de B. Baynes, J. R. A. Cleaver, T. MNishima, I. Ohbu, "Ulrafst characterization of in-plane-gate field-effect transistors: parasitics in laterally gated transistors", Opt. and Quantum Elec. **28**, 907 (1996).

[71] M. Y. Frankel, J. F. Whitaker and G. A. Mourou, "Optoelectronic transient characterization of ultrafast devices", IEEE J. Quantum Electron. **28** 2313 (1992).

[72] M. Y. Frankel, S. Gupta, J. A. Valdmanis and G. A. Mourou, "Terahertz attenuation and dispersion characteristics of coplanar transmission lines", IEEE Trans. Microwave Theory and Tech. **39**, 910 (1991).

[73] S. Alexandrou, C.-C. Wang, M. Currie, R. Sobolewski and T. Y. Hsiang, "Loss and dispersion at subterahertz frequencies in copalnar waveguides with varying ground-plane widths", Proc. SPIE **2149**, 108 (1994).

[74] C. Shu, X. Wu, E. S. Yang, X.-C. Zhang and D. H. Auston, "Propagation characteristics of piocosecond electrical pulses on a periodically loaded coplanar waveguide", IEEE Trans. Microwave Theory and Tech. **39**, 930 (1991).

[75] N. G. Paulter, D. N. Sinha, A. J. Gibbs and W. R. Eisenstadt, "Optoelectronic measurements of picosecond electrical pulse propagation in coplanar waveguide transmission lines", IEEE Trans. Microwave Theory and Tech. **37**, 1612 (1989).

[76] R. W. McGowan, D. Grischkowsky and J. A. Misewich, "Demonstrated low radiative loss of a quadrupole ultrashort electrical pulse propagated on a three strip coplanar transmission line", Appl. Phys. Lett. **71**, 2842 (1997).

[77] H.-J. Cheng, J. F. Whitaker, T. M. Weller and L. P. B. Katehi, "Terahertz-bandwidth characteristics of coplanar transmission lines on low permittivity substrates"IEEE Trans. Microwave Theory and Tech. **42**, 2399 (1994).

[78] S. Verghese, N. Zamdmer, Q. Hu and A. Förster, "Cryogenic picosecond sampling using fiber-coupled photoconductive switches", Appl. Phys. Lett. **70**, 2644 (1997).

[79] D. R. Dykaar, R. Sobolewski, J. M. Chwalek, T. Y. Hsiang and G. A. Mourou, "Electro-optic sampler for characterization of devices in a cryogenic environment", Advances in Cryogenic Eng. **33**, 1097 (1988).

[80] LC home page, http://lc.cray.com/ (Silicon Graphics, 1999).

[81] N. Zamdmer, Q. Hu, S. Verghese and A. Förster, "Mode-discriminating photoconductor and coplanar waveguide circuit for picosecond sampling", Appl. Phys. Lett. **74**, 1039 (1999).

[82] S. Verghese, private communication.

[83] J. F. Whitaker, G. David and M. Crites, "Integrated-circuit diagnostics using micromachined photoconductive sampling probes", in Technical Digest of Ultrafast Electronics and Optoelectronics, paper UWB1, Optical Society of America (1999).

[84] M. van Exter and D. R. Grischkowsky, "Characterization of an optoelectronic terahertz beam system", IEEE Trans. Microwave Theory and Tech. **38**, 1684 (1990).

[85] I. Brener, D. Dykaar, A. Frommer, L. N. Pfeiffer, J. Lopata, J. Wynn, K. West and M. C. Nuss, "Terahertz emission from electric field singularities in biased semiconductors", Optics Letters **21**, 1924 (1996).

[86] K. A. McIntosh, E. R. Brown, K. B. Nichols, O. B. McMahon and W. F. Dinatale and T. M. Lyszczarz, "Terahertz photomixing with diode lasers in low-temperature-grown GaAs", Appl. Phys. Lett. **67**, 3844 (1995).

[87] A. S. Pine, R. D. Suenram, E. R. Brown and K. A. McIntosh, "A terahertz photomixing spectrometer: application to SO_2 self broadening", J. Mol. Spectrosc. **175**, 37 (1996).

[88] P. Chen, G. A. Blake, M. C. Gaidis, E. R. Brown, K. A. McIntosh, S. Y. Chou, M. I. Nathan and F. Williamson, "Spectroscopic applications and frequency locking of THz photomixing with distributed-Bragg-reflector diode lasers in low-temperature-grown GaAs", Appl. Phys. Lett. **71**, 1601 (1997).

[89] An introduction to LC, http://lc.cray.com/doc/intro.html (Silicon Graphics, 1999).

[90] J. P. Berenger, "A perfectly matched layer for the absorption of electromagnetic waves", J. Comput. Phys. **114**, 185 (1994).

THESIS PROCESSING SLIP

FIXED FIELD: ill. _____ name _____

index _____ biblio _____

▶ COPIES: (Archives) Aero Dewey (Eng) Hum
Lindgren Music Rotch Science

TITLE VARIES: ▶ ☐ _____

NAME VARIES: ▶ ☒ Noah Daniel

IMPRINT: (COPYRIGHT) _____

▶ COLLATION: 168 P

▶ ADD: DEGREE: _____ ▶ DEPT.: _____

SUPERVISORS: _____

NOTES:

cat'r: date:

page: 502

▶ DEPT: E. E.

▶ YEAR: 1999 ▶ DEGREE: Ph. D.

▶ NAME: ZANDNER, Noah